A DISSERTATION FOR THE DEGREE OF DOCTOR OF PHILOSOPHY

Development and application of nanoporous carbon materials by catalytic activation of residual solids obtained from biorefinery processes

바이오리파이너리 공정 부산물의 촉매 활성화 공정을 이용한 나노 세공 탄소 소재 개발 및 활용

Advisor Professor: Hye Jung Youn

By Hyewon Hwang

PROGRAM IN ENVIRONMENTAL MATERIALS SCIENCE
DEPARTMENT OF FOREST SCIENCES
GRADUATE SCHOOL
SEOUL NATIONAL UNIVERSITY

FEBRUARY, 2018

Development and application of nanoporous carbon materials by catalytic activation of residual solids obtained from biorefinery processes

바이오리파이너리 공정 부산물의 촉매 활성화 공정을 이용한 나노 세공 탄소 소재 개발 및 활용

지도교수 윤 혜 정

이 논문을 농학박사 학위논문으로 제출함
2017년 11월

서울대학교 대학원
산림과학부 환경재료과학전공
황 혜 원

황혜원의 농학박사 학위논문을 인준함
2018년 1 월

위 원 장	최 인 규	(인)
부위원장	윤 혜 정	(인)
위 원	최 준 원	(인)
위 원	이 학 래	(인)
위 원	이 재 원	(인)

Abstract

Development and application of nanoporous carbon materials by catalytic activation of residual solids obtained from biorefinery processes

Hyewon Hwang
Program in Environmental Materials Science
Department of Forest Sciences
The Graduate School
Seoul National University

Solid co-products from biofuel technologies have great potential as a promising precursor to replace bituminous coal, conventional raw material for preparing nanoporous activated carbon. There are positive double effects of securing alternative resources that are environmental friendly and economically sustainable as well as valorization of co-products with enhancing the efficiency of the biorefinery process. However, the conversion mechanism has not fully understood due to the complexity of various influence factors, and very little has known about utilization of carbon material from co-products. This research focuses on effects of various reaction parameters on properties of activated carbon product, followed by evaluating performance as a versatile carbon material in further industrial application.

First, fast pyrolysis char, obtained from two biomasses at 500°C with a residence time of 1.3 s, was used as a precursor of nanoporous carbon material under different KOH loadings. In order to investigate a potential application as a biosorbent, phenol removal test according to contact time and initial adsorbate concentration was also conducted. After the catalytic activation, a super-active carbon with a large pore volume (1.58 cm^3/g) and high specific surface area

(2711 m^2/g) was successfully prepared. In addition, Langmuir adsorption capacity of the produced activated carbon for phenol was 625 mg/g, which superior to that of AC (500 mg/g), and correlation study revealed that mesopore volume has a positive correlation with adsorption capacity.

Second, preparation and modification of activated carbon derived from different precursor chars (fast pyrolysis char and hydrochar) under different atmospheric conditions (N_2 and zero air) and by post-acidification (HNO_3) were performed. Additionally, an evaluation of their potentials for application as an adsorbent for heavy metal and a carbon electrode was carried out. The specific surface area of the precursor chars was less than 23 m^2/g, but it increased to 1515-1879 m^2/g for N_2-activated carbon and 842-1022 m^2/g for air-activated carbon. Changes in aromatic macromolecular structure for each carbon product were observed and conditions of zero air rendered the char more reactive than under conditions of pure N_2. A plausible reaction mechanism for this observation was suggested to be the formation of a key intermediate in the presence of excess air. Furthermore, the performance when used in applications for various fields depended on the carbon properties such as specific surface area, functional group, hydrophilicity, and mesopore ratio. Compared to post-modified carbon, the air-activated carbon exhibited high versatility to function as both a Pb^{2+} adsorbent (~41.1 mg/g) and energy storage material (~185.9 F/g).

Lastly, the effects of various parameters, such as feedstock, temperature, reaction time, and catalyst loadings on chemical and structural properties of activated carbon derived from lignin were investigated. The assessment of adsorption capacity for removal of heavy metals (Pb^{2+} and Cd^{2+}) and organic compounds (phenol, bisphenol-A, and 2,4-dichlorophenoxyacetic acid), and electrochemical properties was also performed. Catalytic reaction occurred from the external surface under mild conditions of less than 750°C and within 1 h, then it transferred to the internal region under more severe reaction conditions with volatile release of de-alkylated aromatics, leading to structure and surface collapse. The maximum BET surface area of 2782 m^2/g was obtained under 750°C, 2 h and catalyst ratio of 4. Lignin-derived activated

carbon was more efficient for removal of organic pollutants rather than heavy metals due to interaction of π-π bonding. Furthermore, the activated carbon has a potential to be used as a supercapacitor electrode with a specific capacitance up to 214.0 F/g.

Keywords: Fast pyrolysis, Hydrothermal liquefaction, Lignin, Activated carbon, Aromatic hydrocarbon, Surface modification, Biosorbent, Carbon electrode

Contents

Chapter 2

Manufacturing a super-active carbon using fast pyrolysis char from biomass and correlation study on structural features and phenol adsorption ····· 47

Chapter 3

Facile surface modification of nanoporous carbon prepared from a co-product of biofuel technologies for efficient biosorbents and carbon electrodes ····· 91

Chapter 4

Lignin-derived hierarchically porous carbon under various reaction parameters for high-performance adsorbent and supercapacitor ····· 133

List of Tables

List of Figures

List of Abbreviations

LCCs	Lignin-carbohydrate complexes
EDLCs	Electronic double layer capacitors
YP	Yellow poplar
JP	Japanese red pine
Rf	Response factors
AH	Aromatic hydrocarbon
PAH	Poly aromatic hydrocarbon
PSD	Pore size distribution
PC	Pyrolysis char
HC	Hydrochar
CV	Cyclic voltammetry
OA	Oxygenated aromatics
BTX	Benzene, toluene, and xylene
AL	Asian lignin
IL	Inbicon lignin
BPA	Bisphenol-A
2,4-D	2,4-Dichlorophenoxyacetic acid
CAC	Commercial activated carbon
PCA	Principal component analysis

Chapter 1

Introduction

1. Background

1.1. Lignocellulosic biomass as a renewable carbon source

Lignocellulosic biomass is organic matter derived from wood, agricultural, and herbaceous biomass, mainly composed of cellulose, hemicellulose, and lignin. Lignocellulosic biomass has great advantages as an inedible resource with no competition with food as well as low cost, abundant and reliable supply availability comparing to conventional fossil fuel. It is also a renewable and environment-friendly energy source, which can contribute to the reduction of carbon dioxide emissions. It could be expected to save up to 38 million tonnes of carbon emission to the atmosphere by carbon sequestration effect from the use of biomass instead of fossil fuel (Canadell & Schulze, 2014). For now, however, more than 60% of the total global demand for traditional biomass use is for cooking and heating in the residential and commercial building sectors which have very low conversion efficiency (10-20%) (IRENA, 2014). Because biomass applications have been changing over time, a prospect for biomass as an energy source is auspicious that it could account for 60% of total final renewable energy use in various industrial sectors by 2030.

Therefore, a lot of attentions have been paid to the study on development of alternative fuel and chemical materials from biomass for substitution of fossil fuel. The proper techniques for clean and green sustainable energy source will contribute to the improvement of fields of materials, environment, and energy science in future (Figure 1-1).

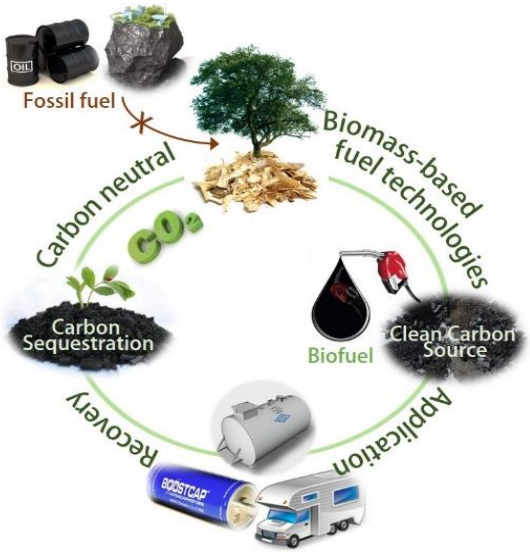

Figure 1-1. Carbon sequestration cycle based on biomass utilization for biorefinery process.

1.2. Biomass conversion processes to liquid biofuel

Figure 1-2 shows the biomass conversion processes to biofuel and it has a potential for use as electricity, heat, fuel, and chemical materials. Among those, pyrolysis, hydrothermal liquefaction, and hydrolysis followed by saccharification techniques generates liquid biofuel such as bio-crude oil and bioethanol. Both liquid fuels, bio-crude oil and bioethanol, are products to replace petroleum oil in terms of power generation and transportation fields. There are several differences between them that bio-crude oil is usually derived from thermochemical conversion process of whole biomass and consists of oxygenated hydrocarbon compounds while bioethanol is obtained from biochemical conversion process of only carbohydrate portion in biomass and the product is ethanol literally.

For crude oil production, typically the processes are conducted under oxygen limit condition and high temperature enough to decompose the structure of biomass component. As for the presence of solvent, the techniques can be mainly divided by two types of dry-based pyrolysis and wet-based pyrolysis.

Fast pyrolysis is one of the most promising processes based on dry-based method to yield liquid oil in large quantities up to 70 wt.%. In this process, biomass is rapidly heated at around 500°C with short vapor residence times (typically less than 2 s) in the absence of oxygen and any solvent (Bridgwater et al., 1999). During the fast pyrolysis, the polymeric constituents of biomass are thermally degraded into numerous small molecules and are converted to volatile vapors that condense to form liquid bio-crude oil. The heavy mass from recondensation of fragments or incompletely decomposed portion is separated and recovered as a solid product, pyrolysis char.

Hydrothermal liquefaction is the other bio-crude oil production process based on wet-based pyrolysis. Water is used as a solvent and the process condition is

generally set at the temperature of sub- or super-critical condition of water, 280-370°C, at between 10-25 MPa with longer reaction times more than 30 min compared to fast pyrolysis (Toor et al., 2011). The degradation mechanism is significantly different from that of fast pyrolysis by hydrolysis of biomass constituents under sub- or super-critical water condition. The liquid product from this process is yielded less, but has high level of higher heating values and low water content, which represents a better quality as a liquid fuel. Hydrochar, water fraction, and gas were also obtained in this process.

On the other hand, the processing of lignocellulosic biomass to bioethanol consists of four major operation steps: pretreatment, hydrolysis, fermentation, and product separation/purification. Above all, biomass is need to be treated with physical, chemical, thermal, or biological method to enhance accessibility of enzymes for further steps by breaking down of the rigid structure attributed to crystallinity of cellulose and complexity of lignin. Then it is converted to small fragments such as sugars and ethanol through the following procedures. The final product is ethanol derived from carbohydrates of biomass while lignin was removed and recovered as a byproduct to improve an efficiency of biorefinery process.

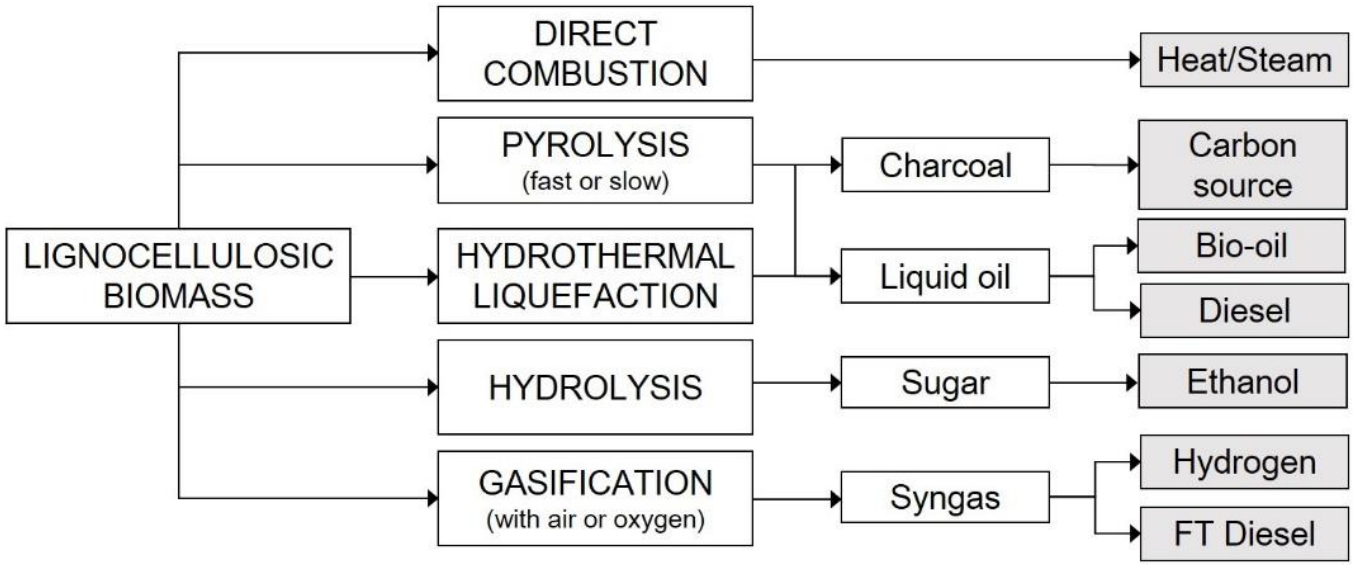

Figure 1-2. Overview of conversion techniques for the production of biofuels from biomass.

1.3. Pyrolysis char and hydrochar

Solid product recovered from fast pyrolysis and hydrothermal liquefaction is called pyrolysis char and hydrochar, respectively. Both chars significantly differ from each other in terms of their physical and chemical properties due to different process conditions that dry or wet pyrolysis (Figure 1-3). The chemical reaction mechanism of each process is so complicated that it has been still partially understood (Libra et al., 2011). Thus, more specific investigation of structural and physicochemical properties according to feedstock and process conditions is required for better understanding of conversion mechanism. It would also enhance their availability to be fit for the targeting purpose economically by predicting qualities of char products from the control of process conditions.

Moreover, both char products have great advantages such as porous, easy handling, energy and carbon rich material. Although the char product has been commonly used only for combustion with a low value, it can be utilized for soil amelioration, nutrient conservation via intelligent waste stream management and the increase of carbon stock. Furthermore, it has also potential to be used in environmental, catalytic, electronic and agricultural applications by post thermochemical treatments.

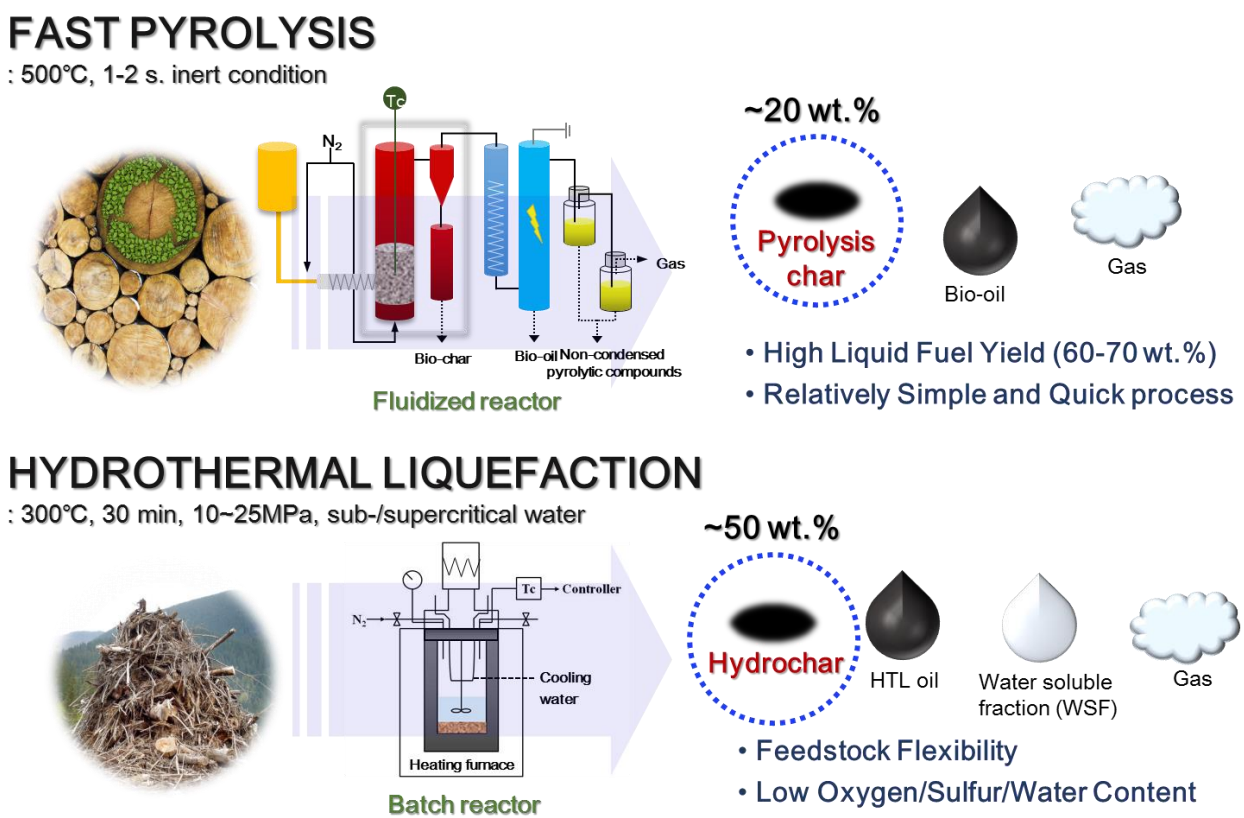

Figure 1-3. Thermochemical processes for the production of pyrolysis char and hydrochar.

1.4. Residual lignins and its potential use

As described above, lignin is one of the main components in biomass bio-synthesized from three monomeric phenols of *p*-coumaryl alcohol (H unit), coniferyl alcohol (G unit), and sinapyl alcohol (S unit). The plausible structure of lignin is shown in Figure 1-4. The structural building blocks of lignin are linked by carbon-carbon and ether bonds but its exact polymer structure was not thoroughly figured out due to its complexity with a high degree of condensation. Besides, the structure of lignin inevitably depends on the isolated techniques including an extraction method from the original biomass and technical processes such as pulping or refinery by using chemical or physical treatment.

Among those techniques, large quantities of lignin are generated from pretreatment process which is essential for the production of bioethanol from lignocellulosics due to its recalcitrance. During the process, crystallinity of cellulose and rigid and compact structure of lignin are decomposed and then carbohydrates are further treated for conversion to a goal product while lignin is obtained as a byproduct. Most of lignin byproducts have mainly being utilized for combustion as a boiler fuel. However, the quantity of lignin from biorefinery process in bioethanol production is estimated to reach 225 Mtons to meet the goal to replace 30% of fossil fuels by biofuels by 2030 (Kumar et al., 2009). Therefore, the valorization of residual lignin as functional added polymers and biomaterials is the utmost important areas of research to increase the usage of byproduct and achieve sustainable economy in future.

Numerous studies have been performed to investigate the potential applications of lignin considering its carbon-condensed structure containing aromatics which makes it possible to replace fossil fuels as an alternative resource for carbon materials and aromatic compounds (Kai et al., 2016; Xu et al., 2014). The future use of lignin will depend on the possibilities of either

degrading it into aromatic hydrocarbons or to take advantage of lignin as a multi-functional macromolecule.

Among many research fields, the most prominent lignin utilization so far seems to be its depolymerization into lower-molecular weight compounds. However, as mentioned above, a significant amount of residues would still remain after depolymerization techniques because rigid and complex three-dimensional aromatic structures of lignin would result in difficulties of easy degradation by simple catalyst or process. For utilization of lignin in pyrolysis oil production, a large portion of solid char also produced from the process whereas the oil is highly oxygenated and unstable during storage requiring further upgrading (Amen-Chen et al., 2001).

Thus, conversion of whole lignin solids to macromolecule composites with improved physicochemical properties is one of the solution strategies for valorization of residual lignin. Specifically, carbonaceous material with high specific surface area and reactivity can be generated from lignin mass by post-activation treatment.

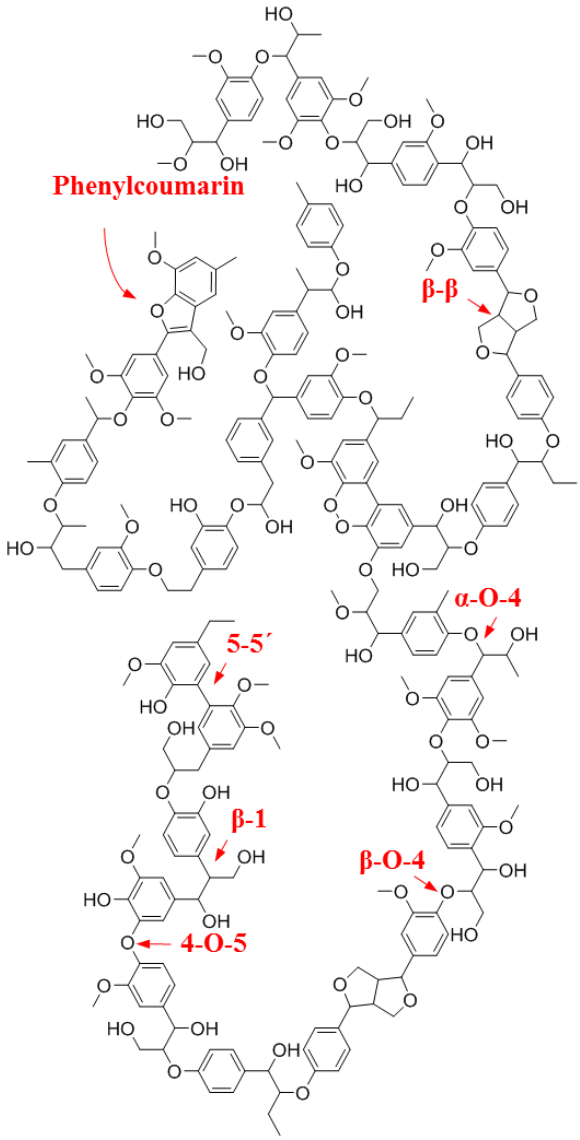

Figure 1-4. Schematic representation of lignin structure.

1.5. Activated carbon and need for alternative precursor sources

Activated carbon is a form of carbon with small pores that increase the surface area available for adsorption or chemical reactions. The major commercial and industrial fields are water treatments followed by air purification, food and beverage, pharmaceutical and medical, automotive, and other sectors like catalyst support and energy storage material (Figure 1-5) (Grand View Research, 2016; Transparency Market Research, 2013). The world activated carbon market size exceeded $ 3 billion in 2015 and it is anticipated to gradually rise at Compound Annual Growth Rate (CAGR) of 11.9 % till 2019 with growing concerns related to drinking contaminated water (Figure 1-6) (Grand View Research, 2016). The largest activated carbon production company in the world, Calgon carbon corporation, has annual sales of $ 500 million by generating more than 100 kinds of products mainly from bituminous coal, a fossil fuel.

However, the supply of raw material is getting unreliable because coal is being depleted and causing environmental problems. Indeed, harmful substance released from the coal mining and refinery industry should be controlled according to regulatory norms and guidelines as suggested by Environmental Protection Agency (EPA) in USA. Some of activated carbon are produced from nut shell or wood biomass, but still a high price of the product makes for researchers have made efforts in low-cost as well as sustainable alternatives.

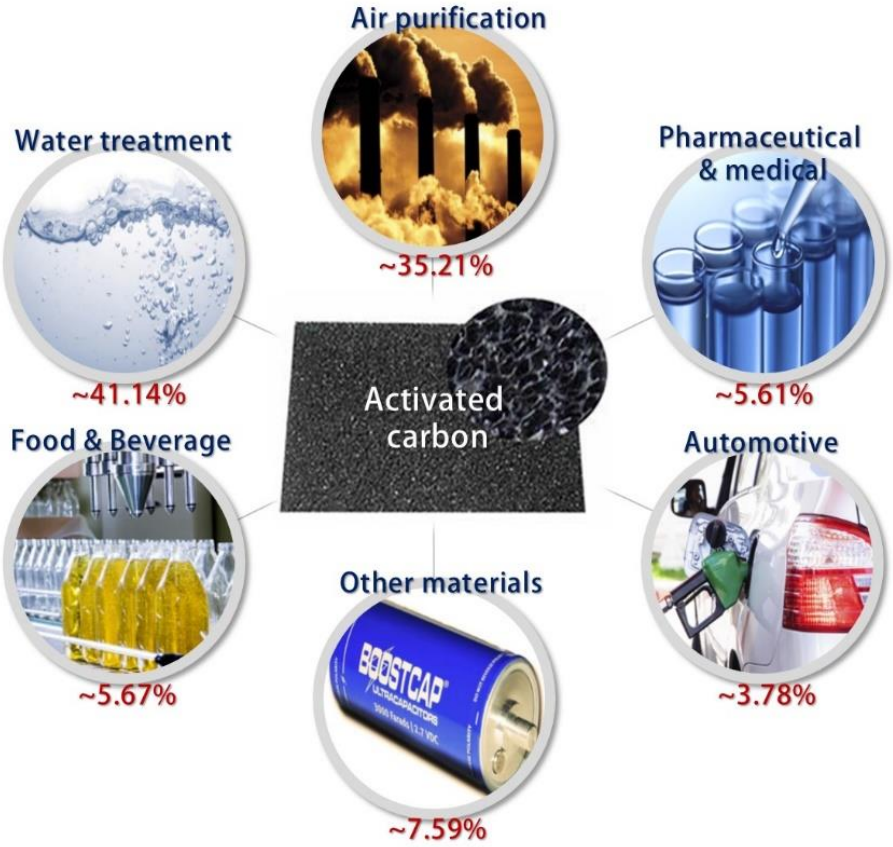

Figure 1-5. Global activated carbon market in various application fields (Transparency Market Research, 2013).

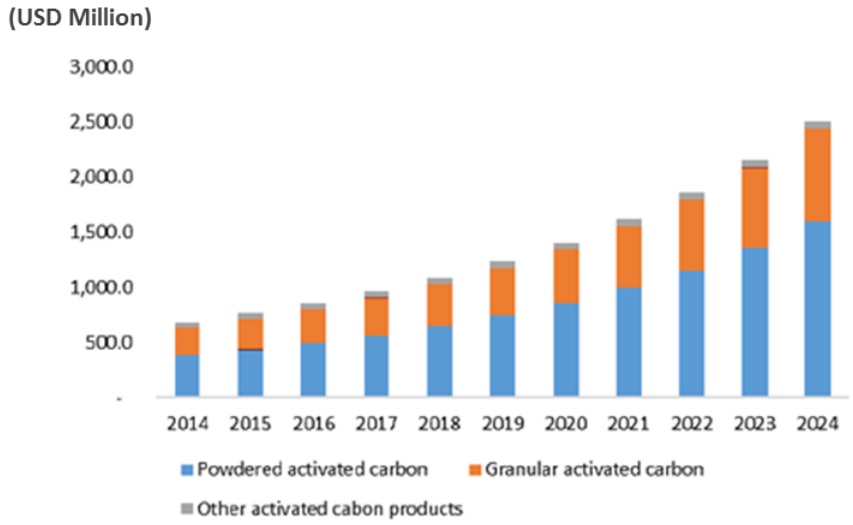

Figure 1-6. U.S. activated carbon market revenue by product, 2014-2024 (Grand View Research, 2016).

On the other hand, according to Korea Customs Service, activated carbon industry in Korea run $ 94 million trade deficit in 2016. It could be mainly attributed to a deficiency of raw material as well as fundamental technologies in the country, resulting in high dependence on overseas products. Therefore, both seeking for a suitable source and development of proper techniques are necessary to self-reliance of the country in activated carbon industry.

Residual solids mentioned above including char products (pyrolysis char and hydrochar) and lignin from biorefinery process could be a clean carbon solution as a precursor of activated carbon with great advantages of sustainable, renewable, and inexpensive source. In other words, a reliable supply of raw materials for activated carbon could be accomplished with increasing values of residual solids from biofuel technologies. It could be also achieved that development of own techniques adequate for the country's circumstances corresponding to raw material supply to produce activated carbon.

2. Objectives

Solid co-products such as char and lignin from biofuel technologies have great potential as a promising precursor to replace bituminous coal, conventional raw material for preparing activated carbon. Although activation is a well-known process, the conversion mechanism has not fully understood due to the complexity of various influence factors, and very little has known about utilization of activated carbon from co-products. Valorization of co-products into high quality carbon material and its application in advanced industrial fields provides positive double effects of supplying alternative resources that are environmental friendly and economically sustainable as well as enhancing the efficiency of the total biorefinery process.

In this study, the effects of various reaction parameters (raw material, temperature, reaction time, and catalyst loading) on chemical and structural characteristics of nanoporous activated carbon obtained fast pyrolysis char, hydrochar, and lignin were investigated. In order to better comprehensive understanding of catalytic mechanism of each precursor, volatiles released during the process was identified and quantitated by thermogravimetric analysis and analytical pyrolysis. Raman spectroscopy was used for investigation of changes in carbon aromatic structure of activated carbon. The other properties such as surface functionalities, morphological and porous features were also analyzed by FT-IR, XPS, SEM, and BET anlaysis. From this result, surface and structure development behavior such as bond cleavage, carbon lattice explosion, pore creation was observed according to process conditions. Additionally, simultaneous surface development by controlling atmospheric condition was attempted, and its feasibility as a facile modification was assessed and compared to conventional post-acidification.

Furthermore, the performance of the produced activated carbon in practical

use was evaluated in comparison with commercial activated carbon. It was utilized as not only an adsorbent for removal of Pb^{2+}, Cd^{2+}, phenol, bisphenol, and 2,4-dichlorophenoxyacetic acid in aqueous standard solution, but also a carbon electrode for supercapacitor. Electric properties were analyzed by cyclic voltammetry and electrochemical impedance spectroscopy using three-electrode system. Based on these results, the correlation between properties of activated carbon and application performance was discussed.

Therefore, the objectives of this study were:

(1) To investigate structural development mechanism of solid co-products during catalytic activation process

(2) To investigate the effects of various parameters e.g. raw material, temperature, reaction time, and catalyst loading on carbon network structure and surface functionalities of produced carbon material

(3) To evaluate a potential of the carbon product for practical use as a biosorbent and electrode

(4) To investigate the correlation between properties of carbon product and its performance on application fields

3. Literature review

3.1. Residual solids from biofuel production

3.1.1. Solid product from fast pyrolysis of biomass

As demand for an alternative energy resource increased, numerous studies have been investigated to produce sustainable and renewable clean fuel with high efficiency and quality, associated with yield and properties of products, respectively.

Fast pyrolysis is one of the most suitable processes to produce liquid fuel from biomass with high yield up to 70 wt.% (Bridgwater et al., 1999; Czernik & Bridgwater, 2004). Many researches revealed that the yield and properties of products highly depend on various influence factors e.g. feedstock type, moisture content, particle size, temperature, and residence time, etc. Kim et al. performed fast pyrolysis of yellow poplar to examine the effects of temperature and residence time on production of pyrolytic products (Kim et al., 2011). The yield and properties of liquid oil from fast pyrolysis of 5 different feedstocks including wheat straw, switch grass, miscanthus, willow short rotation coppice, and beech wood were also characterized and compared in other group (Greenhalf et al., 2013). Moreover, our previous studies were conducted to understand the effects of particle size, moisture content, and inorganic elements of biomass on the properties of liquid product (Hwang et al., 2013; Hwang et al., 2015; Hwang et al., 2012).

In those studies, the process has mainly concentrated on optimization of liquid fuel production and its characterization. Among all the pyrolytic products (gas, liquid, and solids), physicochemical properties were usually analyzed only for liquid product. Although liquid oil is a main target product of fast pyrolysis,

solid char also produced as typically 15-20 wt% from feedstock.

The formation and structure of char from biomass are complex and not fully understood yet. Demirbas suggested reaction mechanisms (1-1)-(1-3) for char formation during biomass pyrolysis (Demirbas, 2004).

$$\text{1st step : Biomass} \rightarrow \text{Water} + \text{Unreacted residue} \quad (1\text{-}1)$$

$$2^{nd}\text{ step : Unreacted residue} \rightarrow (\text{Volatile + Gases})_1 + (\text{Char})_1 \quad (1\text{-}2)$$

$$3^{rd}\text{ step : } (\text{Char})_1 \rightarrow (\text{Volatile + Gases})_2 + (\text{Char})_2 \quad (1\text{-}3)$$

According to the mechanisms, dehydration occurred and primary char formed with volatile and gases together followed by the formation of carbon-rich residual solids by chemical rearrangement reaction.

Meanwhile, Kim et al. investigated physicochemical properties of pyrolysis char from pitch pine under different temperature conditions (Kim et al., 2012). The high temperature condition led to the high degree of carbonization for char while oxygen and hydrogen were removed. Besides, highly ordered aromatic structure was formed at the temperature above 400°C. Additionally, the physical-chemical transitions of two plant biomass (wood and grass) were studied as charring temperature increased from 100 to 700°C (Keiluweit et al., 2010). The results indicated that four distinct categories of char formed as follows; the crystalline part, incipient aromatic polycondensates, poorly ordered graphene stacks, and turbostratic chars. The dynamic molecular structure of char was visually described in Figure 1-7.

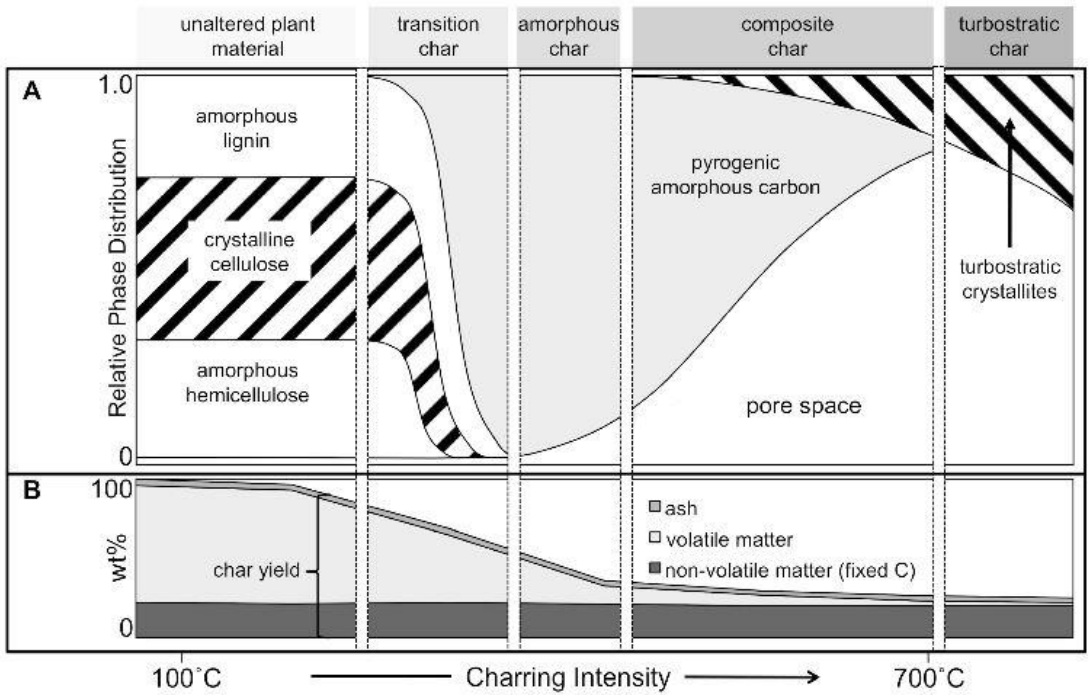

Figure 1-7. Dynamic molecular structure of plant biomass-derived char across a charring gradient and schematic representation of the four proposed char categories and their individual phases.

(A) Physical and chemical characteristics of organic phases.

(B) Char composition as inferred from gravimetric analysis (Keiluweit et al., 2010).

Based on the characteristics of porous, easy handling, energy and carbon-rich material, pyrolysis char has potential as soil amendment, adsorbent, catalyst support, and precursor for activated char (Azargohar & Dalai, 2006; Beesley et al., 2011; Mani et al., 2013; Mohan et al., 2014). Li et al. suggested that high cation exchange capacity correlated with O/C ratio of char would improve soil properties and carbon sequestration (Lee et al., 2010). For activated carbon, fast pyrolysis char provided from Dynamotive Coporation (Vancouver, BC, Canada) was subjected to be activated by chemical activation and BET surface area of the produced carbon material was larger than 1500 m^2/g due to formation of small graphite-like structure (Azargohar & Dalai, 2006). Therefore, pyrolysis char can be utilized in many application fields with extraordinary effects even though most of applications are still in their early stages. The potential and practical utilization fields are summarized in Table 1-1.

Table 1-1. Potential for biochar applications in various fields (Qian et al., 2015).

Application	Purpose	Advantage	Disadvantage
Soil amendment	Carbon sequestration, soil quality improvement	Low cost, sustainable resource, retain nutrient, reduce fertilizer consumption and GHG emission	Possible PAHs contaminant
Adsorbent	Adsorption of contaminants	Low cost, abundant and sustainable resource, and oxygenated groups on biochar surface facilitate adsorption	Uncertain effectiveness
Catalyst	Syngas cleaning, biodiesel production	Easy to recycle supported metal, co-catalyst, low cost	Relative low efficiency
Activated carbon	Precursor for making activated carbon	Low cost, abundant and sustainable resource	Properties vary with different precursors

3.1.2. Solid product from hydrothermal liquefaction of biomass

Hydrothermal treatment of biomass have been gained attention as a method to obtain chemicals along with liquid and gas fuel (Bobleter, 1994; Kambo & Dutta, 2015). But the recent researches are more focused on solid product, hydrochar, that have several value-added applications.

To extend the understanding of conversion of biomass during hydrothermal process, Kruse and Dinjus suggested the main reaction pathways of the ionic reaction mechanism as shown in Figure 1-8 (Kruse & Dinjus, 2007). The mechanism includes protonation, deprotonation by OH^- ion, hydration, keto–enol-tautomerization, acetalization and aldol condensation. The self-dissociation of water is the basis of many suggested mechanisms for hydrolysis and elimination, which would be different from pyrolysis process.

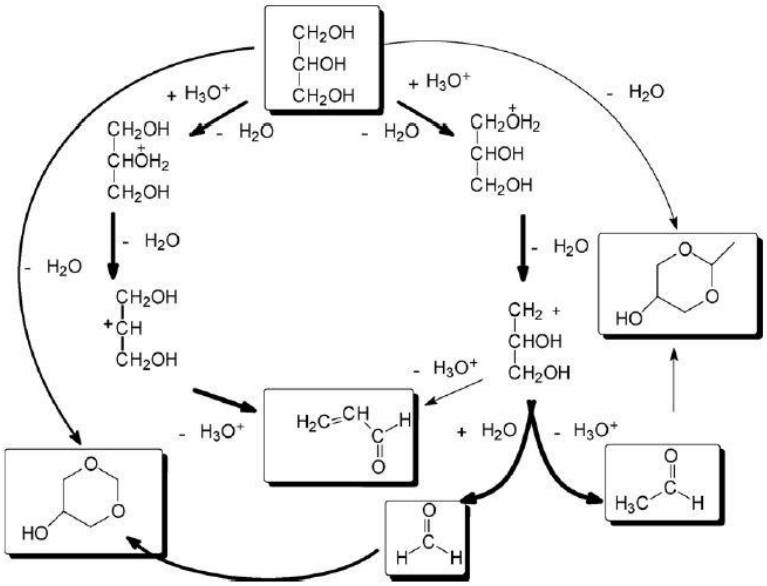

Figure 1-8. Main reaction pathways of the ionic reaction mechanism (Kruse & Dinjus, 2007).

For char formation during hydrothermal process, a simplified representation of the mechanism is shown in Figure 1-9. (Dinjus et al., 2011; Karayıldırım et al., 2008). Biomass could be converted to char product via both reaction path A and B. Specifically, carbohydrates preferably reacts according to path A while lignin does to path B. Additionally, the reaction is represented rather simply and it must be assumed that both reaction paths may influence each other or mix.

In order to investigate the characteristics of hydrochar, different types of biomass (cellulose, cauliflower, grass, straw, beechwood, lignin) were hydrothermal treated under various temperature conditions in ranges of 180-250°C for 4 or 17 h (Kruse & Dinjus, 2007). As reaction temperature and time increased, carbonization and perforated structure were observed. In particular, lignin can hardly be decomposed hydrolytically and remained as noticeable structure of initial state while carbohydrates can be converted to spherical particles.

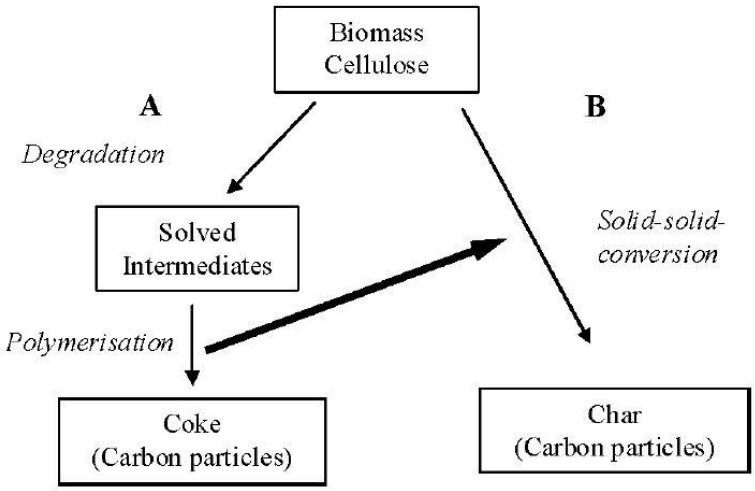

Figure 1-9. Simplified representation of the chemical processes during hydrothermal carbonization (Dinjus et al., 2011; Karayıldırım et al., 2008).

Because hydrochar is usually compared with pyrolysis char, comparative studies of them have been performed. Kambo and Dutta investigated differences between hydrochar and pyrolysis char in terms of production, physico-chemical properties and applications (Kambo & Dutta, 2015). In the review paper, hydrochar typically has lower carbon content, less aromatic matrix, and lower BET surface area compared to pyrolysis char due to different reaction medium and pathways. In addition, hydrochar has more oxygen-rich functional groups on its surface, the application for adsorption using it would be more suitable than pyrolysis char.

On the other hand, Zhu et al. prepared a novel porous carbon from hydrochar via activation process (300-700°C) to investigate its characteristics and adsorption behavior for tetracycline (Zhu et al., 2014). A high surface area (>270 m^2/g) was observed from the product produced at 500-700°C and linear relationships were obtained between Freundlich adsorptive capacity (K_F) and elemental atomic ratios, surface area and pore volume. The high adsorption capacity of activated carbon product can be attributed to its low polarity and high aromaticity, surface area and pore volume.

3.1.3. Lignin as a byproduct from pretreatment process

Lignin structure depends on the isolation procedures, pretreatment methods. Among those, hydrothermal pretreatment is used as a physical technique, which has advantages that no additional chemicals are necessary. After the pretreatment, high Mw with a broad molar mass of lignin was observed, attributed to cleavage of ether linkages in the lignin accompanied by agglomeration into smaller particles and separation from cellulose resulting in a more heterogeneous lignin structure (Kaparaju & Felby, 2010). In addition, ^{13}C-NMR was used for the estimation of structural changes of lignin, indicating that extensive depolymerization of lignin occurred by homolytic cleavage of the aryl-ether bonds (β-O-4 linkages) (Wen et al., 2013).

On the other hand, sodium hydroxide (NaOH) is used for alkaline pretreatment, resulting in a highest level of delignification and cellulose conversion (He et al., 2008; Silverstein et al., 2007). The ester bond of lignin-carbohydrate complexes (LCCs) was destroyed through the hydrolysis reaction, and a large molecular weight and three-dimensional structure of lignin was converted to a small fragment after NaOH pretreatment (He et al., 2008).

In addition, acid pretreatment using H_2SO_4 or HCl leads to depolymerization of lignin by cleavage of ether linkages (Samuel et al., 2010). At the same time, aromatic ring condensation occurrs follwed by new formation of C-C bonds. The condensed lignin matrix makes it difficult to use for valueable applications.

In order to utilize residual lignin from biorefinery process rather than a fuel for combustion, several applications were implemented in a lap-scale such as phenolic resins, dispersants, and automotive brake pads (Lora & Glasser, 2002). One of possible application using whole lignin macromolecules is as a precursor for activated carbon production. Indeed, lignin has a high carbon content and its molecular structure is similar to coal, thus it would be an ideal precursor.

3.2. Activation process using chemical reagent

3.2.1. Activated carbon production from biomass resource

Activated carbon is commonly derived from coal (anthracite, bituminous, sub- bituminous and lignite), nut shells, wood, and peat. In order to generate porous network in carbon source, physical and chemical process is often used (MARSH, 2006). Chemical activation is generally performed at 400-900°C with activating chemical agents such as KOH, H_3PO_4, $ZnCl_2$, etc.. Comparing to physical activation, chemical activation has superior advantages of lower reaction temperature, higher yields, less activation time, and higher specific surface area (SSA) and micropore volume.

In particular, KOH activation is outstanding to produce activated carbon with high SSA and micropore volume. Otowa et al. proposed the reaction mechanism of KOH activation below 700°C as shown in (1-4)-(1-7) (Otowa et al., 1993). KOH dehydrates to transform into K_2O at 400°C (1-4) and then carbon is consumed by the reaction between carbon and H_2O with the emission of H_2 (1-5). Finally, K_2CO_3 is formed at about 400°C from the reaction of K_2O and CO_2 produced in the reaction (1-6).

$$2KOH \rightarrow K_2O + H_2O \quad (1\text{-}4)$$

$$C + H_2O \rightarrow CO + H_2 \quad (1\text{-}5)$$

$$CO + H_2O \rightarrow CO_2 + H_2 \quad (1\text{-}6)$$

$$CO_2 + K_2O \rightarrow K_2CO_3 \quad (1\text{-}7)$$

The other studies also suggested the reaction mechanism during KOH activation above 700°C (Lozano-Castello et al., 2007; Raymundo-Pinero et al., 2005). According to the mechanisms (1-8)-(1-11), K_2CO_3 would be decomposed to K_2O and CO_2 at temperature higher than 700°C, completely

disappeared at 800°C. The produced CO_2, K_2O and K_2CO_3 then can be reduced to be converted into metallic K at higher temperature over 700°C. This metallic K compound results in expansion of intercalation structure of carbon lattice as shown in Figure 1-10 (Romanos et al., 2011). After the activation, K-related compounds then are removed and high microporous structure can be created.

$$K_2CO_3 \rightarrow K_2O + CO_2 \quad (1\text{-}8)$$

$$CO_2 + C \rightarrow 2CO \quad (1\text{-}9)$$

$$K_2CO_3 + 2C \rightarrow 2K + 3CO \quad (1\text{-}10)$$

$$C + K_2O \rightarrow 2K + CO \quad (1\text{-}11)$$

Thus, KOH activation has been applied to prepare fossil-based carbon sources for high SSA and micropore volume (Otowa et al., 1993). However, fossil-based carbon sources are non-renewable, thus development of renewable and eco-friendly source is required for the production of activated carbon.

In this regard, many studies have been carried out to prepare high SSA-activated carbon from renewable biomass using KOH. Activated carbon was prepared from wheat straw at 700°C using KOH:char ratio of 3.5:1 (Li et al., 2010). The activated carbon had SSA of up to 2316 m^2/g and pore volume of up to 1.50 cm^3/g with uniform pores below 4 nm. Wood sawdust-based activated carbon was also produced from hydrothermal treatment, followed by KOH activation and it had high SSA (2968 m^2/g) and pore volume (1.35cm^3/g) mainly below 3 nm (Wei et al., 2011). Furthermore, Khezami et al. investigated the characterization of activated carbon from cellulose, lignin, and xylan, and it was revealed that the porosity of the product recreated within cell walls and middle lamellae regardless of the initial porous structure (Khezami et al., 2005).

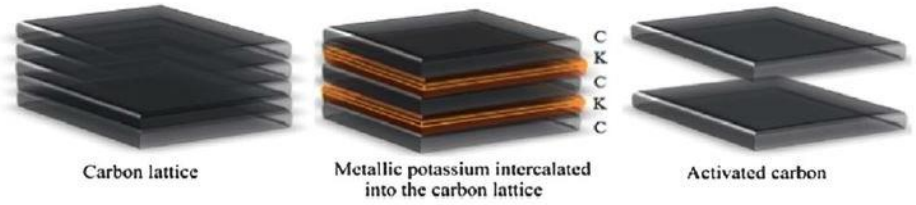

Figure 1-10. Activation mechanism by the penetration of metallic K into the carbon lattices (Romanos et al., 2011).

3.2.2. Influence factors on activation process

The activation process and mechanism of biomass carbon source are dependent on various parameters e.g. temperature, amount of catalyst, time, and feedstock type. Those parameters significantly influence on the reactivity of carbon source, produced pore structure and surface chemistry, leading to further affects the performance of activated carbon in application fields.

Wei et al. performed KOH activation of starch, cellulose, and wood under different temperature conditions of 700°C and 800°C, and the high temperature showed the largest volume of small mesopores in the range of 2–3 nm (Wei et al., 2011). In addition, SSA of activated carbon from wood largely increased while that from cellulose decreased as temperature increased to 800°C.

Gao et al. studied the effect of catalyst loading (0.5-4), temperature (650-850°C), and reaction time (0.5-2.5 h) on properties of activated carbon and adsorption behaviors using lignin (Gao et al., 2013). For development of high SSA, activation at 750°C for 1 h with catalyst loading of 3:1 was the optimum condition in the study. Meanwhile, micropore surface area and volume increased from 1h to 2.5 h, indicating that an increase of total SSA might be not always corresponded with an increase of micropore. They suggested the activation mechanisms according to temperatures as shown in Figure 1-11.

Romanos et al. investigated the textural properties of activated carbon from corncob biomass and revealed that the pore size distribution is differed each other according to the reaction temperature and catalyst loadings (Figure 1-12) (Romanos et al., 2011). The porosity increased as KOH ratio and temperature increased, suggesting that penetration of metallic potassium into the carbon matrix increased and then lattice would be further expanded, followed by increase in porosity. Thus, pore characteristic could be controlled by the process parameters to use in proper application fields for the material.

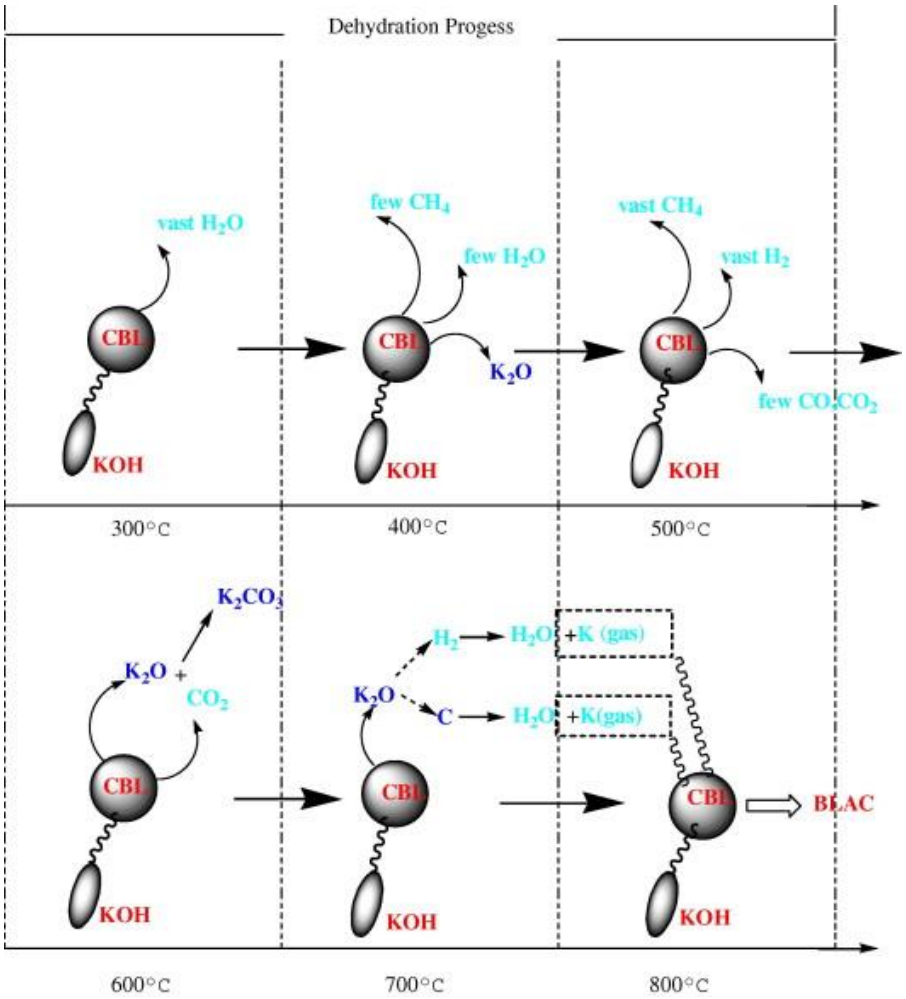

Figure 1-11. The activation mechanisms of KOH on carbonized black liquor lignin under different temperatures (Gao et al., 2013).

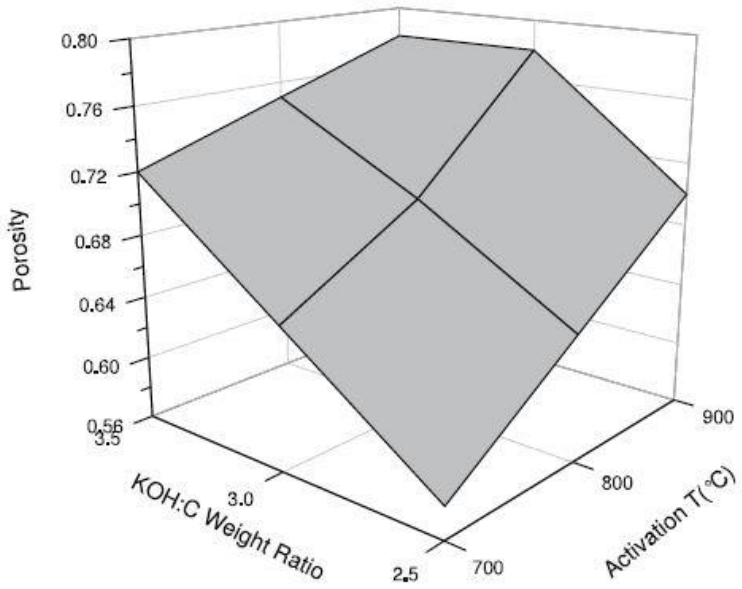

Figure 1-12. Porosity dependence on the KOH:C weight ratio and the activation temperature (Romanos et al., 2011).

3.2.3. Modification of surface functionalities of activated carbon

Furthermore, approach to modify the surface functionalities of activated carbon to enhance the chemical reactivity with other substances has been performed. To investigate surface characteristics after modification, thermal or chemical post-treatment was carried out and surface properties were determined by using various experimental techniques (Figueiredo et al., 1999). Oxygen-containing gas was used for gas phase oxidation of activated carbon product during the operating process and HNO_3 was used for liquid phase oxidation treatment after the process. There are differences in carbon products that the main increase in hydroxyl and carbonyl groups for gas-oxidized product and carboxylic acids for liquid-oxidized product, respectively.

Pyrolysis char derived from Bamboo was treated by chemical methods ($KMnO_4$, HNO_3 and NaOH) and heat method (Li et al., 2014). The surface features and adsorption capacity for furfural were investigated for each modified carbon products. The result showed that hydrophilicity increased by chemical modification whereas it decreased by heat treatment. The largest amount of acidic functional groups was introduced by HNO_3 treatment rather than other treatment. For furfural adsorption capacity, it was related to the basic surface group content, which can be attributed to the enhancement of dispersion interactions, thus the highest capacity was obtained for heat-treated samples with a total removal efficiency at a furfural concentration of 10 g/L.

Additionally, the effect of surface oxidation on removal efficiency of metallic contaminant in aqueous solution (Pb^{2+}, Cu^{2+}, Cd^{2+}, and Ni^{2+}) was investigated by using hydrochar from peanut hull (Xue et al., 2012). Surface oxidation using H_2O_2 enhanced the oxygen containing functional groups, particularly carboxyl groups, and the modified hydrochar showed higher heavy metal adsorption capacity about 20 times more than untreated hydrochar, which was comparable

to that of commercial activated carbon.

Chen and Wu also prepared activated carbon with nitic acid or hydrochloric acid treatment to change surface groups, and investigated metal adsorptive properties (Chen & Wu, 2004). As a result, copper uptake by nitric acid-treated carbon product significantly increased due to an increase in surface functional groups such as phenols, ethers, and lactones.

3.2.4. Characterization of carbon products

In general, char, carbon material is not well-defined chemical substance, resulting in difficulties in identification of the precise structure even though using all the techniques currently available. The fact that there is no standard model of char from biomass also leads to large variations of properties. To determination of char structure before and after certain conversion process, various analytical methods have been tried to solid products.

SEM (Scaning Electron Microscope) analysis has been widely used to examine the morphological features of solid surface (Azargohar et al., 2014; Zhu et al., 2014). The changes in surface such as collapsed, slit, and new pore structure can be visually observed with different magnifications. For characterization of functional groups and bonding structure on surface, Fourier-transform infrared spectroscopy (FT-IR), Boehm titration, and X-ray photoelectron spectroscopy (XPS) analysis have been conducted (Boehm, 1994; Boehm, 2002). From FT-IR analysis, functional groups on the surface of solid carbon material can be determined by representative peaks on the spectra. The peak for aromatic ring stretching (around $1600cm^{-1}$) is usually found for activated carbon (Zhao et al., 2016). Meanwhile, Boehm suggested the titration methods for quantifying and qualifying acidic/basic functional groups on surface of carbon samples. Several surface oxide groups (shown in Figure 1-13 (Montes-Moran et al., 2004)) including carboxylic, lactonic, phenolic, and basic groups can be identified using different titration reagents such as NaOH, Na_2CO_3, $NaHCO_3$, and HCl. XPS analysis is conducted for analysis of functional structure based on binding energy. The photoelectron spectrum can be deconvoluted to several main signals e.g. aliphatic/aromatic carbon groups, hydroxyl group, carbonyl group, and carboxylic/ester/lactone group and then surface chemical structure can be quantified (Wagner et al.).

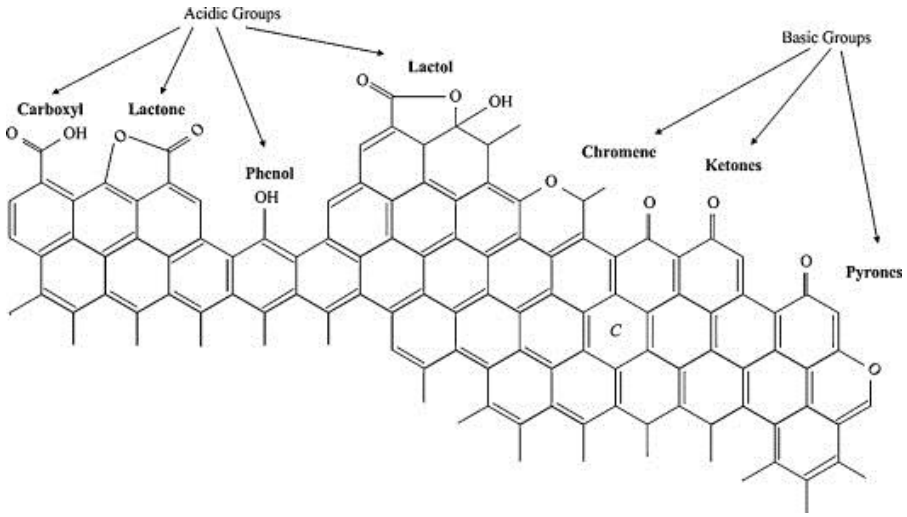

Figure 1-13. Acidic and basic surface functionalities on a carbon basal plane (Montes-Moran et al., 2004).

In addition, Brunauer–Emmett–Teller (BET) and Barrett-Joyner-Halenda (BJH) analysis are well-known methods for characterization of textural properties of solid char (Barrett et al., 1951; Brunauer et al., 1938). Specific surface area is commonly examined by BET method using N_2 adsorption at 77 K which is a critical temperature for nitrogen to be condensed onto the surface. Pore volume and size can be analyzed by BJH method and pore size distribution can be also obtained from desorption isotherm of porous substances. For structural characterization, X-ray diffraction (XRD) analysis is used and amorphous or graphitic crystalline structure can be measured from its patterns. Girgis et al. thoroughly analyzed activated carbon from steam and acid treatment by XRD analysis and revealed that interlayer spacing, microcrystallite lateral dimensions, and turbostratic graphene layer exist therein (Girgis et al., 2007). Furthermore, Raman spectroscopy, one of the most powerful tools for characterizing carbon materials, has been recently used to investigate wide variety of structural features of solid carbon materials. The classification of order or disorder structure and Sp^2 cluster size can be determined by deconvolution of Raman spectra using Gaussian bands. Especially, the I_d/I_g ratio is often used in amorphous carbons as a parameter indicating the relative content of sp^2 or sp^3 bonding structure (Shimodaira & Masui, 2002).

3.3. Practical use of biomass-derived activated carbon

3.3.1. Biosorbent for water remediation

Adsorption applications have been divided into mainly two categories of organics (dyes, phenolics, polyaromatics, etc.) and inorganics (cations and anions). Among those, phenolics and heavy metals are the representative ones of contaminants that can pose serious problems such as protein degeneration, tissue erosion, paralysis of the central nervous system, and damage to brain functions when entering the drinking water system even at low concentration (Knop & Pilato, 2013; Naseem & Tahir, 2001). Thus, it is considered necessary to remove those harmful substances from industrial effluents before discharging into the water stream.

Activated carbon has exhibited a great potential to adsorb water contaminants due to its porous structure and wide availability of the product by surface modification. Adsorption by activated carbon is one of the promising methods that frequently used to remediate water among other methods including aerobic and anaerobic biodegradation, oxidation by ozone, and uptake by ion exchange resins, etc.. It is attractive for its simplicity of process, flexibility in design and operation, high-quality treated effluent, and insensitivity to toxic substances, but activated carbon is still costly to make. In this regard, many studies have been tried to use sustainable source, biomass to produce activated carbon and apply for water remediation.

Removal ability of activated carbon from rattan sawdust was evaluated for phenol adsorption in a batch process under the different solution concentrations (25-200 mg/L) and pH (3-10) (Hameed & Rahman, 2008). The phenol adsorption capacity increased as the initial solution concentration increased while it did not affected by the initial pH in the range of 3-8. The maximum

adsorption capacity was estimated as 149.25 mg/g determined by Langmuir model. Liu et al. proposed chemical interactions between phenol and char surface as shown in Figure 1-14 (Liu et al., 2011). The adsorption mechanism contains Lewis acid-base complexation, hydrogen bonding, and π-π stacking interactions.

For heavy metal adsorption behavior study, Gao et al. carried out Ni^{2+} adsorption test for activated carbon derived from black liquor lignin under different parameters (initial solution concentration, contact time, and solution pH) (Gao et al., 2013). As a result, the adsorption thermodynamics can be well represented by Langmuir isotherms and Q_m, Langmuir constant, was estimated as 14.02525 mg/g. The adsorption gradually approached equilibrium at 30 min and then remains constant for further contact times. It was also revealed that the initial concentration affected the time to reach equilibrium state and adsorption capacity increased by increasing pH due to driving force and electrostatic attraction, respectively.

In addition, the adsorption test for Pb^{2+} by activated carbon from Poaceae was conducted under different parameters (pH, contact time, and solution concentration) (Lalhruaitluanga et al., 2010). The optimum adsorption condition was determined for pH 5.0, contact time 120 min, and the maximum adsorption capacity was estimated as 53.76 mg/g. The several functional groups of –OH, C=O, and carbonyls were mainly related to lead adsorption by carbon samples. Consequently, activated carbon from biomass source can be efficiently used as a biosorbent material for water remediation technologies.

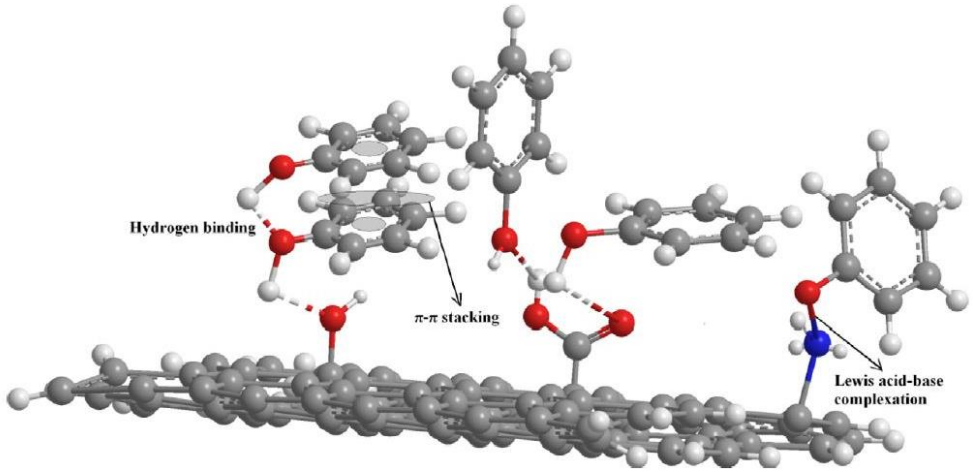

Figure 1-14. Chemical interactions between phenol and the functional groups on the surface of char (Liu et al., 2011).

3.3.2. Electric energy storage material

Supercapacitors (also known as electronic double layer capacitors (EDLCs)) are gaining increasing attention for energy storage applications in recent years due to their fast charging rates, high energy and power densities, and good cycle life. Typical uses of supercapacitor are for memory back-up systems, industrial power and energy management, and a temporary energy storage device for elevators and regenerative braking in electric and hybrid cars. The charge accumulates at the electrode/electrolyte interface as presented in Figure 1-15 (Pandolfo & Hollenkamp, 2006) and the capacitance of a device is largely dependent on the characteristics of the electrode material.

Because of adjustable microstructure and large SSA, activated carbon has been intensively investigated to prepare a carbon electrode. Wheat straw and lignocellulosic biomass-based activated carbon, from the literatures as mentioned in 2.2.1., showed the specific capacitance as 251 F/g and 236 F/g, respectively, higher than that of commercial electrode (~100 F/g) (Li et al., 2010; Wei et al., 2011). Figure 1-16 provides the comparing result of specific capacitance of biomass-based activated carbon and commercial activated carbon. Marta et al. studied supercapacitive behavior of activated carbon from glucose by direct pyrolysis and hydrothermal treatment (Sevilla et al., 2014). The result indicates that hydrothermally carbonized glucose exhibits a superior rate capability and a higher specific capacitance (240 F/g) in accordance to higher SSA and it can be a suitable material for high-power supercapacitors. Furthermore, it has excellent robustness even for a large cell voltage of 1.2 V in 1 M H_2SO_4. Jiang et al. studied about nanostructured carbon material from KOH activation of ginkgo shells and its application on electrochemical supercapacitors. The produced activated carbon had SSA of 1775 m^2/g and specific capacitance of 178 F/g at a potential scan rate of 500 mV/s, which is

superior to that of commercial activated carbon (< 50 F/g). It also showed high performance on cycle stability with 92.6 % capacity retention for 5000 cycles.

Moreover, lignin is also preferred as a precursor for the production of activated carbon and electrode. Suitable functional groups, if it does not already exist, can be easily modified onto the surface of the lignin char macromolecules to enhance the pseudo-capacitance, increase the amount of energy stored in the super-capacitor, improve the wettability and enhance the cycle stability of the electrode (Kai et al., 2016). Saha et al. produced porous carbon from lignin, and the produced material used as supercapacitor electrode materials, exhibited gravimetric specific capacitances of 91.7 F/g suggesting a potential use in specific electrochemical applications of lignin (Saha et al., 2014).

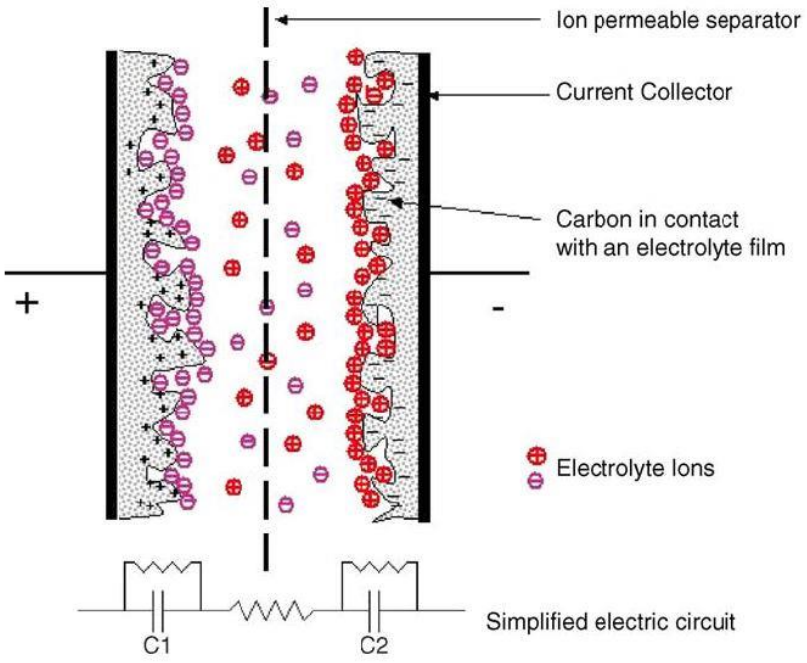

Figure 1-15. Representation of an electrochemical double layer capacitor (in its charged state) (Pandolfo & Hollenkamp, 2006).

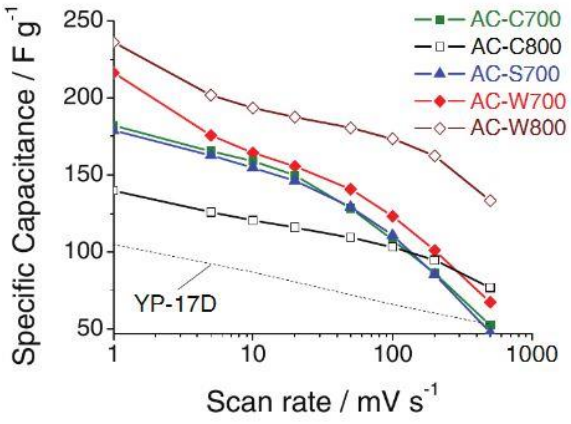

Figure 1-16. Specific capacitance of carbon samples at different CV scan rates in comparison with that of commercially available YP-17D activated carbon (AC-C700: activated carbon from cellulose at 700°C; AC-C800: activated carbon from cellulose at 800°C; AC-S700: activated carbon from starch at 700°C; AC-W700: activated carbon from wood at 700°C; AC-W800: activated carbon from wood at 800°C; YP-17D: commercial activated carbon commonly used in supercapacitor) (Wei et al., 2011).

Chapter 2

Manufacturing a super-active carbon using fast pyrolysis char from biomass and correlation study on structural features and phenol adsorption

A paper published in RSC advances
7(67) (2017) 42192-42202

1. Introduction

Fast pyrolysis is one of the most promising thermal conversion processes to produce liquid alternative fuel from dry biomass sources in high yield (~70 wt%) (Bridgewater, 2004). Although the process has been optimized for liquid oil production, it is also accompanied by a valuable co-product, char, a solid-state material mainly composed of carbon (Hwang et al., 2013; Hwang et al., 2015).

Because of the low specific surface area of fast pyrolysis char, very little is known about studies on its application and it has commonly been used for combustion for energy production. However, it has great potential to be utilized as a precursor of porous carbonaceous material due to high carbon content (Azargohar et al., 2014; Kim et al., 2012). The fast pyrolysis char can be converted to high-active carbon through post thermochemical treatment such as activation using chemical agents which provides better availability. Improved quality carbon material is mainly used as a bio-adsorbent (Dąbrowski et al., 2005; Lima et al., 2010), and can be used in the field of catalyst support (Kastner et al., 2012) and electrode material (Wang & Kaskel, 2012).

The world activated carbon market exceeded $3 billion in 2015 and is anticipated to gradually rise at a CAGR of 11.9% by 2019 (Research, 2016). In addition, as concerns related to environmental problems grow, there is an increasing demand for renewable resources to replace coal, specifically bituminous coal, the main raw material of activated carbon. Therefore, if pyrolysis char could be used as a precursor of activated carbon, it would be expected to have a positive effect on the environment as well as provide an economic benefit.

However, there have been few studies conducted on the production of activated carbon using fast pyrolysis char, and in particular, studies on the application as biosorbent have been limited. Instead, A great deal of research

has focused on activation processes using coal (Gong et al., 2009) or biomass such as wood (González-García et al., 2013), nut shells (Schröder et al., 2007), and wastes (Romanos et al., 2011), requiring an additional carbonization step for long times.

Although activation is a well-known process for the commonly used precursors mentioned above, the mechanism has not been fully elucidated due to the complexity of its various parameters. Indeed, most research has mainly represented chemical and structural characteristics of the produced activated carbon and did not deal with the mechanism of structure formation. For the catalytic activation process, a few studies (Lozano-Castello et al., 2007; Otowa et al., 1993; Raymundo-Pinero et al., 2005) have suggested chemical reactions with KOH, widely used activating agent due to its high efficiency in the production of activated carbon with large pore volumes and specific surface areas, mostly focused on the interactions between KOH and carbon solids and changes in the state of the catalyst, not carbon material itself. Thus, study on the degradation procedure of raw material as catalytic activation proceeds is still lacking.

In this study, it was hypothesized that the observation of weight loss tendency and kinds of released volatile compounds during thermal conversion process could provide key information to understand the cleavage process of structural bonding. In addition, KOH activation could result in production of highly-porous activated carbon from fast pyrolysis char. Last but not least, evaluating pollutant removal efficiency by use of the produced carbon material could be strongly associated with its potential to replace commercial one.

In this context, utilization of fast pyrolysis char, co-product from biofuel technology, to a precursor for activated carbon by KOH activation was carried out in this study. Before a practical activation, modification of the char structure was investigated by determining changes in weight loss point of structural degradation and volatile compounds released during the catalytic conversion of

pyrolysis char with KOH. For chemical activation, overall experiments were designed by varying biomass type (softwood and hardwood) and catalyst loading, which are significant factors in the process. Finally, all the samples were subjected to pollutant adsorption test. Phenol, a versatile precursor for plastics, drugs, and herbicide industries, was selected in this study because it is the representative one of priority pollutants determined by the U.S. EPA and it can cause serious problems such as protein degeneration, tissue erosion, paralysis of the central nervous system, and damage to brain functions at low concentrations when entering drinking water systems (Knop & Pilato, 2013; Naseem & Tahir, 2001). Because adsorption capacity is significantly affected by properties of activated carbon, a correlation study was also intensely carried out to determine the most important factor. Furthermore, adsorption capacity as well as chemical, structural, morphological, and textural properties of each carbon product were compared with commercial activated carbon. The present work will help to enhance both value of fast pyrolysis char and efficiency of water remediation by conversion of co-product into a high-performance biosorbent, which is an approach to total biorefinery.

2. Materials and methods

2.1. Feedstock analysis and pyrolysis char preparation

Two kinds of wood, yellow poplar (YP) and Japanese red pine (JP), were kindly provided by the Korea Forest Research Institute (Seoul, Republic of Korea) and were used as the biomass feedstock in this study. Samples were ground and sieved through 0.5 mm mesh, followed by drying in an oven overnight before use. The moisture content of each sample was measured to be less than 2 wt%. Biomass samples were analyzed by elemental analysis (C, H, and N) using a US/CHNS-932 (LECO, USA) and the ratio of oxygen was calculated by difference. Compositional analysis for holocellulose, lignin, and ash content was conducted according to Wise's method (Wise, 1946), TAPPI method (T222 om-88), and National Renewable Energy Laboratory (NREL) standard procedures, respectively. In order to determine the inorganic content of biomass, inductively coupled plasma-emission spectroscopy (ICP-ES) analysis was performed using an ICPS-1000IV instrument (Shimadzu, Japan). Before the analysis, 0.5 g of samples were digested with an addition of 10 mL of acid mixture (HNO_3 : HCl : H_2O_2 (8:1:1, v/v)) by microwave (Mutiwave 3000, Anton Paar). The heating and pressure program were set as follows. Temperature is ramped to 550°C by 5°C/min and held for 5 min, then ramped to 1200°C with the same heating rate, and held 10 min at final temperature. The reaction pressure was maintained at 55 bar with a 0.3 bar/s during the process. After the reaction, liquefied sample was diluted to 50 mL and analyzed. Table 2-1 shows data for the fundamental analysis of the feedstocks.

The char, a carbonaceous precursor for activated carbon, was obtained from fast pyrolysis of the two biomass samples under conditions of 500°C and 1.3 s. The schematic of an experimental apparatus, fluidized bed reactor, for fast

pyrolysis have been provided in previous studies (Hwang et al., 2013; Hwang et al., 2015) and the detailed experimental procedure is as follow. Each biomass was prepared dry and injected into the heated reactor by a screw-type feeder at a rate of about 150 g/h under 10 L/min of N_2 flow rate. Biomass then was rapidly decomposed, some were recovered as liquid oil via an ethanol cooler and an electrostatic precipitator, and some were collected as solid char by a cyclone connected to the reactor. After the experiment, enough gas was allowed to flow for 30 min to react the residual volatiles, and then the temperature of the reactor was lowered. Finally, the collected solid char was weighed and stored in a sealed vial. The char yield was 8.4 wt% for YP and 12.9 wt% for JP based on the wet basis of biomass samples. The produced char from YP and JP was labeled YPC and JPC, respectively.

Table 2-1. Characterization of biomass feedstock.

	Elemental analysis (wt%)*		Compositional analysis (wt%)		ICP-ES analysis (ppm by biomass)			
Yellow poplar	C	45.8						
	H	5.8	Holocellulose	74.0	K	630.4	P	101.2
	O	48.2	Lignin	30.0	Mg	170.4	Si	19.8
	N	0.2	Ash	0.45	Ca	908.6	Fe	35.1
Japanese red pine	C	50.7						
	H	6.1	Holocellulose	73.6	K	721.0	P	286.5
	O	43.2	Lignin	31.4	Mg	199.0	Si	96.9
	N	0.0	Ash	1.0	Ca	1481.7	Fe	96.5

* Oxygen ratio was calculated by difference.

2.2. Thermal degradation analysis of fast pyrolysis char during catalytic conversion

As for analytical approach, thermogravimetric (TG) and differential thermogravimetric (DTG) analyses and pyrolysis-gas chromatography-mass spectrometry (Py-GC-MS) were conducted. The samples for both experiments were prepared as a mixture of ground char and KOH catalyst (Sigma Aldrich), with catalyst ratios of 0, 2:1, and 4:1 (catalyst:char, w:w).

For TG-DTG analysis, approximately 10 mg of each mixture sample was placed in a crucible in the instrument chamber (TGA/DSC 3+(LF-1100) (Mettler-Toledo AG, Switzerland)) and heated at 10°C /min in the temperature range of 40°C to 700°C under a nitrogen atmosphere.

Analytical pyrolysis to identify released volatile compounds from fast pyrolysis char samples during catalytic pyrolysis was conducted using Py-GC-MS equipped with a coil-type CDS Pyroprobe 5000 (CDS Analytical Inc., Oxford, PA, USA) and GC–MS/FID (Agilent Technologies 7890A/Agilent Technologies 5975A, USA) with a DB-5 capillary column (30 m × 0.25 mm ID × 0.25 μm film thickness). The prepared mixture sample including 3 mg of char was introduced into a quartz tube, which was then sealed by glass wool at both ends. For quantitative analysis, 1 μL of internal standard (IS; 1.3 mg of fluoranthene/mL of methanol) was also added to each sample. Finally, the sample was pyrolyzed to 700°C at a heating rate of 10°C/ms and was maintained for 20 s. Subsequently, the released volatile products were on-line transferred to a GC–MS/FID, and the program was set as follows. The GC injector and detector temperatures were set at 250°C and 300°C, respectively. The oven temperature program began with a 50°C hold for 5 min, and the temperature was increased at a heating rate of 3°C/min to 280°C and maintained for 10 min. The separated compounds were transferred into the ionization source of a

quadrupole MS, and ionization was conducted in electron impact mode at 70 eV. The volatile compounds were identified based on NIST MS Search 2.0 (NIST/EPA/NIH Mass Spectral Library; NIST 02), and quantitative analysis was achieved with consideration of response factors (Rf) of each compound, as suggested in a previous study (Kim et al., 2015). The amount of volatiles released from char with different catalyst ratios was calculated with the following equation.

$$\text{Amount of volatiles } (\mu g/\text{g char}) = \text{Rf} \times \frac{A_{volatiles}}{A_{I.S}} \times \frac{Q_{I.S}\ (\mu g)}{Q_{char}\ (g)} \qquad (2\text{-}1)$$

where Rf is the response factor, $A_{volatiles}$ and $A_{I.S}$ are the peak areas of the volatile compounds and internal standard, respectively, and $Q_{I.S}$ and Q_{char} are the amounts of internal standard and char sample.

2.3. Manufacturing of nanoporous carbon from fast pyrolysis char by catalytic activation

Chemical activation of fast pyrolysis char was performed to produce nanoporous activated carbon using batch-type reactor placed at the Institute of Catalysis Research and Technology (IKFT) of Karlsruhe Institute of Technology (KIT). For each experiment, a mixture of pyrolysis char (1.5 g) and KOH (0, 3, or 6 g for ratio conditions of 0, 2:1, or 4:1, respectively, w:w) was prepared and purged with nitrogen (250 ml/min) for 10 min to retain the inert condition of the reactor before activation. The reactor was then introduced into a furnace that had previously reached the reaction temperature of 700°C, and this temperature was maintained for 2 h with a constant flow of nitrogen gas. After activation, the reactor was removed and allowed to cool to room temperature. The mixture was washed with 250 ml of HCl solution (1 M), followed by 2 L of D.I. water to remove the KOH catalyst and residual HCl, respectively. No precipitation was observed in any experiment after adding a droplet of $AgNO_3$ (0.1 M) to the filtrate, which confirmed that HCl had been thoroughly removed. The product was dried in an oven overnight, and the yield was calculated. All experiments were carried out in triplicate, and the produced activated carbon was referred to as YP0, YP2, YP4, JP0, JP2, and JP4 according to the type of precursor and ratio of catalyst.

2.4. Characterization of activated carbon

Elemental analysis for carbon product was carried out by the same method as referred in Section 2.1. The surface morphologies of the samples were observed by field-emission scanning electron microscopy (FESEM), using a SIGMA (Carl Zeiss, UK) at various magnifications. For surface structure analysis, XRD and Raman spectroscopy were carried out using D8 ADVANCE with DAVINCI (BRUKER, Germany) at the National Instrumentation Center for Environmental Management (NICEM) and T64000 (HORIBA Scientific, Japan) at the National Center for Inter-university Research Facilities (NCIRF) at Seoul National University, respectively. XPS measurements were conducted to determine surface chemistry of the samples using AXIS-HSi (KRATOS, UK). Binding energies for high-resolution scanning of C1s spectra were fitted at 284.5 eV for the lowest binding energy peak (C1s(1)), and peak deconvolution was accomplished using casaXPS software. Zeta potential was measured using Zetasizer-nano series (Malvern, UK). The suspension sample was prepared by adding fine char powder to 0.05 N NaCl solution, and adjusting the pH from 3 to 11 with HCl and NaOH solution. The mixture was agitated for better wettability and dispersion over 24 h, and sonicated before the measurement. The texture features were characterized by BET method for specific surface area from N_2 adsorption, the BJH method for pore size and average diameter using adsorption branch, and the t-plot method for micropore structure using an ASAP 2010 (Micrometrics, Canada) with a N_2 adsorption-desorption isotherm at 77 K.

2.5. Phenol adsorption experiment

Phenol (Sigma Aldrich) adsorption tests for fast pyrolysis char and produced activated carbon were performed at 28°C under two different parameters; contact times and concentrations of phenol solution. For the adsorption, 0.05 g of char sample was added to 100 ml of phenol solution was added. The each flask was sealed by parafilm and then shaken at 150 rpm. The effect of contact times on adsorption capability was determined under different time intervals (0.5, 1, 2, 3, 5, 7, and 20 h) using 200 mg/L of phenol solution. The effect of initial adsorbate concentrations was investigated using various phenol solutions (25, 50, 100, 150, and 200 mg/L) with fixed contact times for 20 h to reach equilibrium state of the solution. After the adsorption, absorbance of the filtrate was measured using UV-vis spectrophotometer (EVOLUTION 201, USA) at the wavelength of 270 nm and phenol concentration was calibrated from the absorbance data. The amount of adsorbed phenol at the equilibrium q_e (mg/g) was calculated as follows:

$$q_e = \frac{(C_0 - C_e)V}{W} \quad (2\text{-}2)$$

C_0 (mg/L) and C_e (mg/L) are the initial and equilibrium concentration of phenol solution, respectively, W (g) is the input weight of carbon sample, and V (L) is the volume of phenol solution.

Overall scheme of this study, including three main parts of analytical and practical approach, was provided in Figure 2-1. Furthermore, commercial activated carbon (AC; purchased from Sigma-Aldrich) was characterized and applied to phenol adsorption by the same methods as above in order to compare with the resultant activated carbon samples in this study. All experiments were carried out in duplicate, and the average values are presented.

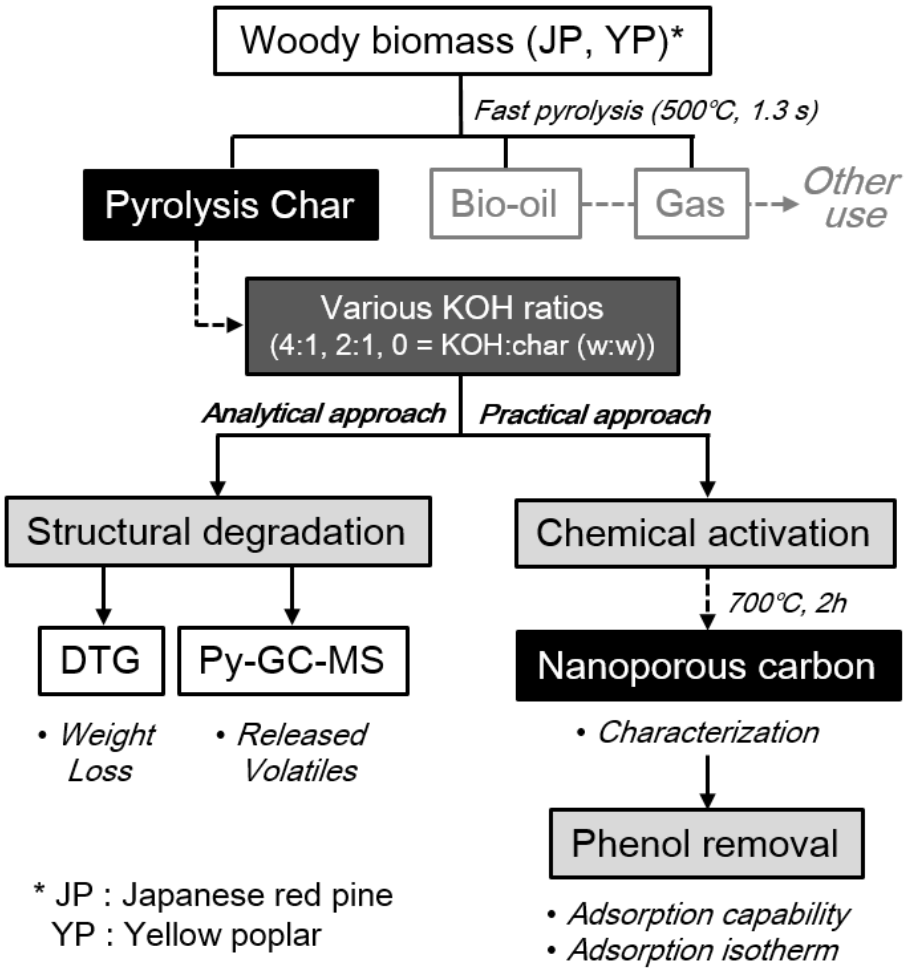

Figure 2-1. Overall scheme of analytical and practical approach to utilize co-product solid from fast pyrolysis to nanoporous material under different catalyst loadings and feedstock types.

3. Results and Discussion

3.1. Thermal degradation behavior of char during catalytic conversion by DTG and Py-GC-MS

Before conducting a practical activation process to produce activated carbon, a study of thermal degradation behavior of fast pyrolysis char in the presence of catalyst was investigated. Changes in sample weight as temperature increased and volatile compounds released from char during catalytic thermal decomposition were analyzed by DTG and Py-GC-MS analysis, respectively.

Figure 2-2 shows the DTG curves of pyrolysis char samples with or without KOH catalyst under a nitrogen atmosphere. The curves for pyrolysis char in the absence of KOH (JPC and YPC) appeared almost linear due to gradual decomposition over the temperature range up to 700°C. In the presence of KOH, however, the curves had two main broad peaks, which indicates that rapid thermal degradation occurred in the temperature range around 200-300°C.

The thermal decomposition behavior of pyrolysis char samples in this study, produced at 500°C in a fast pyrolysis process, likely corresponds to that of lignin or a condensed structure, which remained over the temperature range, rather than whole biomass commonly known for considerable decomposition at 200-300°C due to cleavage of glycosidic bonds in cellulose and degradation of hemicellulose. In that temperature range, remaining propanoid side chains, β-β, C-C, and aryl ether linkages can be cleaved (Brežný et al., 1984; Fiddler et al., 1967; Ludwig & Sarkanen, 1971) to form highly reactive and unstable intermediates that lead to further rearrangement reactions that increase stability. Therefore, peaks could appear by cleavage of the K-C structure complex derived from interaction between KOH and char as the temperature increased.

Then, scission of chemical bonds in the structure of pyrolysis char, that were scarcely reacted or broken without catalyst, was facilitated, resulting in lower thermal stability.

As a result of volatile compounds released from pyrolysis char under different KOH ratios (Table 2-2), a total of 10 aromatic hydrocarbon (AH) and poly AH (PAH) compounds were detected as the main substances, instead of the oxygenated chemicals that are commonly produced from biomass pyrolysis. This result suggests that pyrolysis char already consists of an aromatic backbone structure, and these volatile compounds could derive from the macromolecular lattice of carbonized char by chemical reactions such as dehydrogenation, decarbonylation, and deoxygenation.

As the KOH ratio increased, the total amounts of volatiles increased to 18.46 nmol/g for JPC and 29.56 nmol/g for YPC, which are approximately 6 times and 2 times higher than the amounts without catalyst, respectively. This result corresponds to the DTG results that KOH enhanced degradation of the crystalline char structure, which also leads to pore creation by release of monomeric aromatics during catalytic activation.

Furthermore, the ratio of AH was much higher than that of PAH, and more than 85.1% of the total amount of volatiles consisted of benzene, toluene, ethylbenzene, and xylenes, generally referred to as BTEX, which are valuable compounds in chemical manufacturing. Among these, benzene was the most abundant, accounting for 65.0% and 61.5% of the total volatiles from YPC and JPC, respectively. Although the absolute quantity of benzene increased, its relative proportion gradually decreased with an increase in KOH ratio, whereas the quantities of other compounds increased, specifically toluene and xylenes. There seem to be several possible explanations for this result. It could be assumed that inter-molecular cleavage along with degradation of the char structure occurs more frequently than demethylation as catalyst ratio increased. On the other hand, benzene could be an intermediate that can be converted into

other products under a high ratio of KOH. For instance, gaseous products or alkylated aromatics could be formed by further cracking or an electrophilic substitution reaction by metallic K derived from KOH acting as a catalyst.

For feedstock types, it appears that JPC has a more rigid structure than YPC based on the following results. First, the residue amount for JPC was 83.8%, higher than the 76.8% for YPC, at the final DTG analysis temperature. Next, the main degradation peaks appeared at 220°C and 265°C for JPC, which were 10°C higher than those of YPC. In addition, the amount of volatiles detected from Py-GC-MS analysis of JPC was lower, indicating that its structure is more difficult to decompose. These observations could be attributed to the difference in structural characteristics of the original feedstock. It is generally accepted that there are covalent bonds inside the biomass called lignin-carbohydrate complex (LCC) that differ in softwood and hardwood. According to Jin et al., more than half of cellulose in softwood is combined with lignin, while about one-sixth of the cellulose occurs as lignin complexes in hardwood (Jin et al., 2006). In addition, coniferous lignin is thermally more stable and prone to form a more condensed structure than deciduous lignin due to highly reactive carbonium cations of guaiacyl nuclei as electron-rich aromatic carbons (Müller-Hagedorn et al., 2003; Shimada et al., 1997). Therefore, these differences in inherent structure of feedstock could cause structural rigidity of JPC derived from softwood. During the subsequent catalytic activation, breakdown and rearrangement of the aromatic backbone structure of pyrolysis char could be facilitated by KOH through cleavage of the thermally labile portion of C-C and ether linkages in char, leading to an increase in volatilization of aromatics.

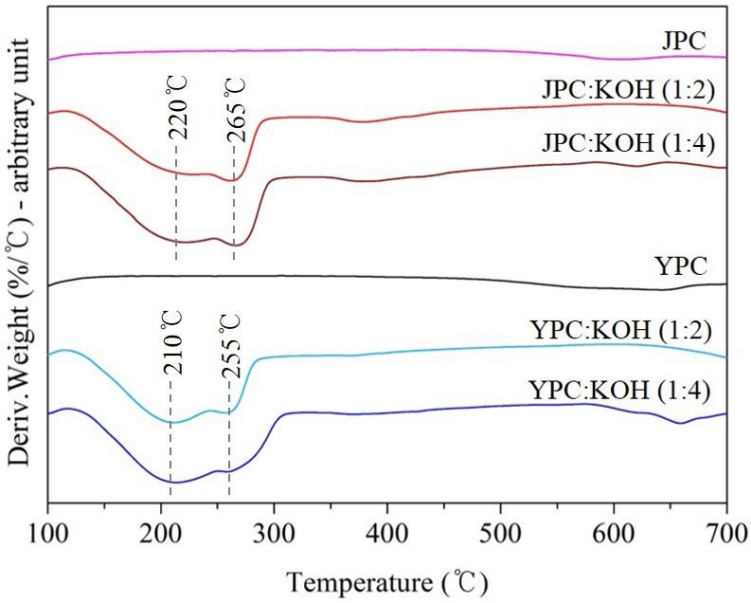

Figure 2-2. DTG curves of pyrolysis char with an addition of different KOH ratios.

Table 2-2. Volatile compounds released from catalytic activation of pyrolysis char by Py-GC-MS analysis.

Type	Compound	YPC:KOH			JPC:KOH		
		No catalyst	1:2	1:4	No catalyst	1:2	1:4
AH[a]	Benzene	0.78*	1.16	1.14	0.16	0.50	0.69
AH	Toluene	0.25	0.68	0.81	0.07	0.29	0.49
AH	Ethylbenzene	0.00	0.02	0.03	0.00	0.00	0.01
AH	p-Xylene	0.01	0.20	0.27	0.00	0.09	0.19
AH	m-Xylene	0.01	0.06	0.08	0.01	0.04	0.05
AH	1,3,5-Trimethylbenzene	0.02	0.02	0.05	0.00	0.03	0.10
	Total AH	**1.08**	**2.13**	**2.38**	**0.25**	**0.95**	**1.53**
PAH[b]	Indene	0.00	0.03	0.07	0.00	0.01	0.05
PAH	Naphthalene	0.11	0.10	0.10	0.01	0.01	0.05
PAH	1-methyl-Naphthalene	0.01	0.05	0.06	0.00	0.00	0.03
PAH	9H-Fluorene	0.01	0.03	0.05	0.00	0.01	0.03
	Total PAH	**0.12**	**0.21**	**0.29**	**0.01**	**0.03**	**0.15**
	Total	**1.20**	**2.34**	**2.67**	**0.26**	**0.98**	**1.68**

* Unit : μg/g char
[a] Aromatic hydrocarbon
[b] Polycyclic aromatic hydrocarbon

3.2. Yields of activated carbon produced from fast pyrolysis char under different KOH ratios

After the practical activation process of fast pyrolysis char using a lab-scale furnace reactor, the yield of activated carbon product was shown in Table 2-3.

Under the same activation process conditions, the activated carbon yield from JPC was higher than that of YPC, also supporting results of the structural degradation studies in Section 3.1 that the condensed and rigid structure of JPC could cause difficulties in thermal degradation.

Without KOH, 78.8 wt% and 91.9 wt% of carbon products were obtained for YP0 and JP0, respectively, and decomposition would occur mainly by the high temperature of 700°C. As the ratio of KOH increased, the residue yield significantly decreased, and even at a catalyst ratio of 4, the yield fell to about half that of the non-catalytic conditions. Therefore, the presence of KOH had a great impact on the production of activated carbon through volatilization of large portion of pyrolysis char. This result could be explained by the change in reactivity and thermal lability of the bonding structure of char by KOH, leading to significant weight loss, as shown in the results of Figure 2-2. In addition, the difference in yield between YPC and JPC was highest without catalyst and gradually decreased with increasing catalyst ratio. This result suggests that the catalytic influence of KOH enhanced degradation of the rigid structure of char that is scarcely decomposed solely by high temperature.

Table 2-3. Yield of activated carbon derived from pyrolysis char.

Product	Yield (wt.%)
YP0	78.8 ± 0.1
YP2	59.2 ± 0.4
YP4	40.5 ± 1.0
JP0	91.9 ± 0.1
JP2	65.5 ± 2.3
JP4	44.5 ± 0.4

3.3. Graphitization and aromatization of pyrolysis char during the KOH activation process

Chemical and structural characteristics of activated carbon products were studied by elemental composition, XRD, Raman spectroscopy, and XPS analysis. From elemental analysis, the carbon ratio of pyrolysis char was 77.6% and 81.9% for YPC and JPC, respectively. As the KOH ratio increased, the product carbon proportion gradually increased to 90.1-90.4%, which was higher than that of AC (86.0%), whereas the hydrogen and oxygen proportions significantly decreased.

Changes in elemental composition in terms of H/C and O/C ratios for biomass feedstock, fast pyrolysis char, and activated carbon products were studied by Van Krevelen plot, as shown in Figure 2-3. Compared to the original feedstock, pyrolysis char had much lower H/C and O/C ratios, which demonstrates that significant structural change of biomass as well as dehydration reactions occurred during fast pyrolysis at 500°C. For JP0 and YP0 carbon product treated at 700°C under non-catalyst conditions, both atomic H/C and O/C ratios decreased compared to those of JPC and YPC. Specifically, the decrease in H/C ratio was more prominent, suggesting that dehydrogenation reactions proceeded at high temperature.

In the presence of KOH, further deoxygenation and dehydrogenation reactions proceeded, and the atomic H/C and O/C ratios of carbon products decreased as much as that of AC, indicating that carbonized material can be obtained by the catalytic activation process using the co-product of fast pyrolysis. In addition, the decrease in these atomic ratios is indicative of growth of aromatic structures in the carbon material (McKendry, 2002); thus, aromaticity of the product gradually increased with KOH activation. This result is related to the observation in Section 3.1 of an increase in release of aromatic

volatiles, which could result from development of a high-degree aromatic structure due to dehydrogenation and deoxygenation enhanced by the catalyst.

In addition, the H/C and O/C ratios of JP-derived carbon products were lower until the KOH ratio was 2. At a KOH ratio of 4, however, the decreases in these ratios were similar regardless of biomass type, demonstrating that a high catalyst loading was effective in promoting degradation of the rigid char structure, as also shown by the yield data in Table 2-2.

Figure 2-4 provides representative data on the structural characteristics of carbon products including XRD analysis and Raman spectroscopy. The XRD pattern in Figure 2-4 (a) shows two broad peaks (15.9° and 20-24°) of JP and YP for the (110) and (200) crystallographic planes with abundant hydroxyl groups involved in a number of intra- and intermolecular bonds in cellulose (Popescu et al., 2011; Wada & Okano, 2001). These peaks disappeared after the fast pyrolysis process, and new peaks corresponding to sp^3-hybridized lattice reflections (around 43°) and graphite fraction (at 21°, 23.5°, and 26.6°) were observed for pyrolysis char and non-catalytic activated carbon products, which can be attributed to degradation of the original biomass structure and creation of crystalline regions. The intensities around 21°, 22°, and 26.6° were also observed for AC, associated with a graphitic structure. In the presence of KOH, the sharp peaks lost intensity, and a broad peak with weak intensity appeared around 43.5°, indicating that intragraphitic layers were decomposed and amorphous carbon material with high porosity formed in the catalytic activation process (Dandekar et al., 1998).

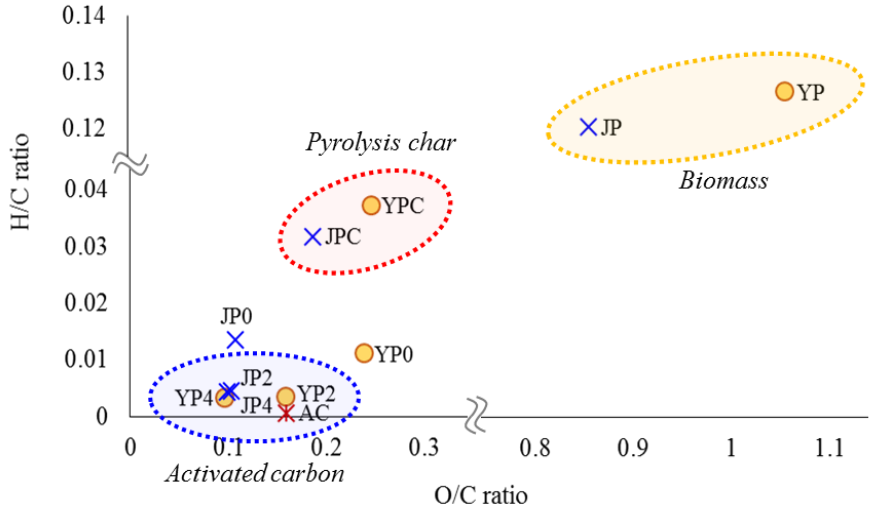

Figure 2-3. Van krevelen diagram of biomass, pyrolysis char, and activated carbon products.

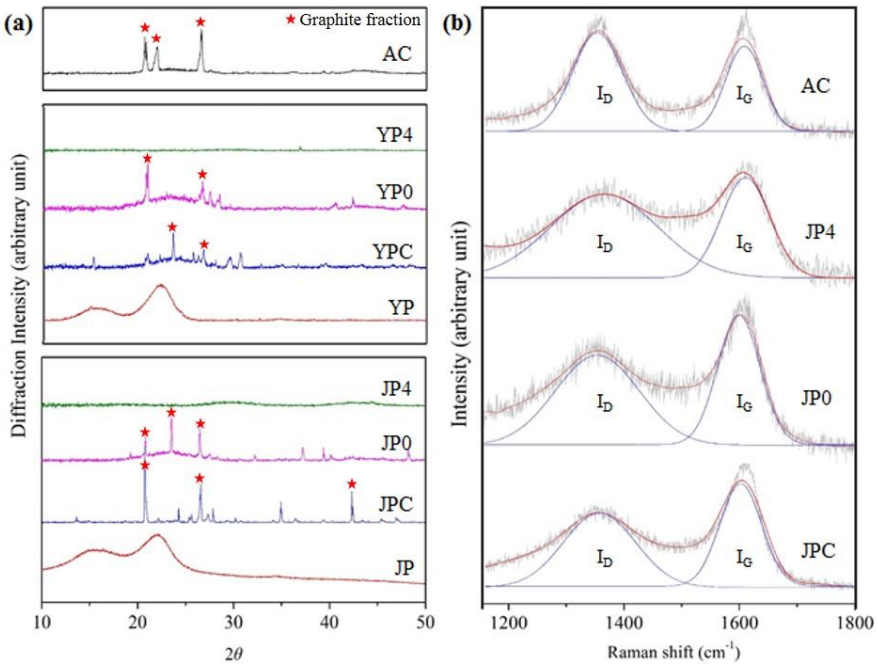

Figure 2-4. Structural analysis of carbon products by (a) XRD and (b) Raman spectroscopy.

From Raman spectra of carbon materials (Figure 2-4 (b)), two main peaks were deconvoluted and represent the presence of a disordered graphitic lattice, C-C bonds between aromatic rings and aromatics, and a medium to large aromatic ring system around 1350 cm^{-1} for the I_D peak and assignment of graphite region and C=C bonds around 1580 cm^{-1} for the I_G peak (Li et al., 2006; Shimodaira & Masui, 2002; Wang et al., 1990). After catalytic activation, the main peaks of JP4 were broader and showed a reduction of the I_G peak compared to those of JPC. This could be attributed to development of amorphous structure rather than graphitization by reaction of KOH and fast pyrolysis char surface (Li et al., 2012; Zhang et al., 2009).

A numerical comparison of disorder and crystallinity of char samples was determined based on the ratio of the integrated intensity of I_D/I_G peaks, as shown in Table 2-3. The ratios of YPC and JPC were 1.09 and 1.24, which increased to 1.51 and 1.85, respectively, when the KOH ratio was 4. The increase in I_D/I_G ratio is attributed to the growth of large aromatic ring systems and the presence of dangling bonds in plane terminations of disordered graphite region in the solid sample (Li et al., 2006; Shimodaira & Masui, 2002; Wang et al., 1990). Thus, significant aromatization of pyrolysis char samples occurred under catalytic activation. These results are in close accord with other observations in this study, enhancement of dehydrogenation and deoxygenation reactions, as suggested in Py-GC-MS and Van Krevelen diagram analyses.

In addition, surface functional characteristics were examined by XPS analysis, and the data are provided in Figure 2-5 and Table 2-4. The results from deconvolution of C1s were classified according to functional groups presented by Zielke et al. (Zielke et al., 1996) as follows: C1s (1) sp^2-graphitic bond, C-C, or C-H (284.5 eV); C1s (2) hydroxyl or ether, C-O (286.0 eV); C1s (3) carbonyl or quinone, C=O (287.0 eV); C1s (4) carboxyl or ester, O=C-O (288.6 eV); and C1s (5) carbonate, CO_3^{2-} (289.5 eV). As seen in Figure 2-5, development of aromatic or conjugated structures after KOH activation was

also confirmed by observing the π-π shake-up satellite tail at a few eV higher than the binding energy of the main peak (Gardella Jr et al., 1986) in XPS spectra of JP4. The produced carbon products mainly consisted of the C1s (1) peak, which could result from a deoxygenated and carbonized structure by high temperature, and they had comparable content to that of AC. Among carbon and oxygen bonds, the C1s (2) peak for C-O bonds was the dominant peak for all carbon products, in agreement with other studies (Azargohar et al., 2014; Dıaz-Terán et al., 2003; Zhao et al., 2016). When inorganic oxide was added to carbon material and the temperature increased, the oxide would transfer to the surface of the char, and bonds between metal and oxygen atoms would dissociate, followed by conversion of -O- free radicals to stable C=O bonds (Xiang et al., 2006). This would result in the appearance of a C1s (3) peak for both YP4 and JP4.

Zeta potential of the activated carbon product and AC was also measured at different pH values as presented in Figure 2-6. As solution pH increased, zeta potential decreased and all the samples have negative zeta potentials over the entire pH ranges, being indicative of negatively charged surface due to the dissociation of acidic functional groups. This accordance with other researches as shown for typical activated carbon (Annadurai et al., 2002; Chen et al., 2016). Catalytic activated carbon exhibited a smaller level of negative charge than non-catalytic product and pyrolysis char. This suggests that reduction degree increased, which could enhance the π-π interaction in the subsequent aromatic organic material adsorption (Wang et al., 2014).

From the results of structural analysis of the produced activated carbon, it could be concluded that both graphitization and aromatization proceeded, with the latter being the more prominent reaction during catalytic activation, along with development of amorphous structure, which could create more edges and corners to react with other substances.

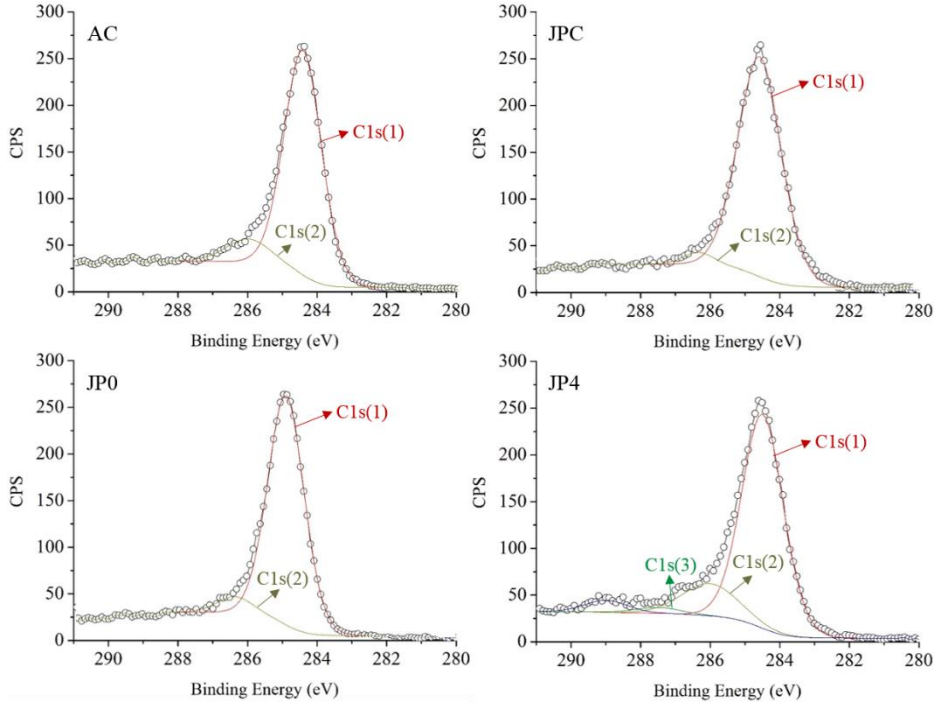

Figure 2-5. XPS scans of C1s photoelectron envelopment for feedstock and carbon products.

Table 2-4. Relative contents of functional groups in the carbon products by XPS spectra and I_D/I_G peak ratios.

Chemical composition (%)	C1s(1)	C1s(2)	C1s(3)	C1s(4)	C1s(5)	I_D/I_G
	sp^2-graphitic or C-C, C-H	C-O	C=O	O=C-O	CO_3^{2-}	
YPC	85.0	15.0	-	-	-	1.09
YP0	83.6	13.2	-	3.2	-	1.18
YP4	78.3	14.7	7.0	-	-	1.51
JPC	96.2	3.8	-	-	-	1.24
JP0	93.6	6.4	-	-	-	1.37
JP4	90.7	8.2	1.1	-	-	1.85
AC	88.9	11.1	-	-	-	1.55

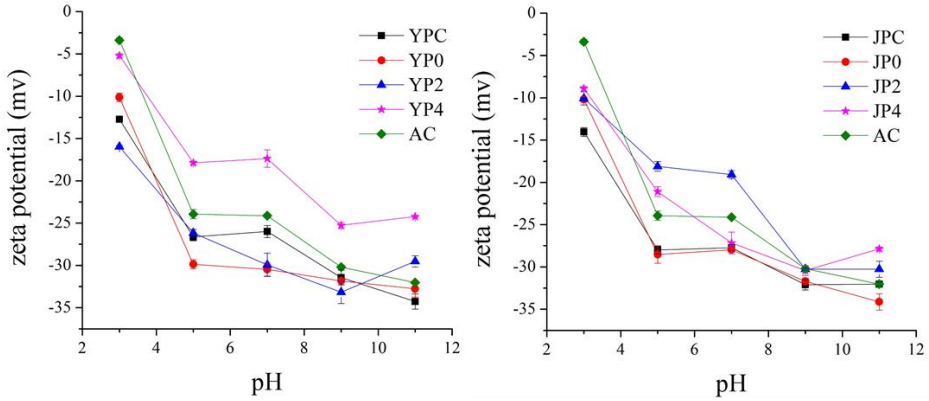

Figure 2-6. Zeta potential curves of carbon products at different pH.

3.4. Changes in morphological and textural features of carbon product

For examination of surface morphological features, SEM analysis was conducted at different magnifications, and the images are shown in Figure 2-7. Before activation, deformation of the biomass structure was observed for YPC and JPC due to pyrolysis at 500°C. For YP4 and JP4, irregularity of the rupturing surfaces was more developed by catalytic cracking; thus, the edge portion could be extended instead of a smooth plane. Specifically, JP4 showed a more fragmented structure than YP4, suggesting there might be more edges that possess reactive sites.

The N_2 adsorption and desorption isotherms are given in Figure 2-8. According to International Union of Pure and Applied Chemistry (IUPAC) classification, catalyzed activated carbon is of type Ⅰ and Ⅳ, representing micropore and mesopore structure. Also, hysteresis loop is shown for catalytic activated carbon and AC, which indicates that bimodal pore structure therein. The features for BET surface area and porosity of the raw carbon material and activated carbon products are presented in Table 2-5 and Figure 2-9. The surface area of fast pyrolysis char from YPC and JPC was low at 9 m^2/g and 27 m^2/g, respectively. As the KOH ratio increased, the surface area dramatically increased to 1908 m^2/g (YP4) and 2711 m^2/g (JP4), which was about three times higher than that of AC. The total pore volume of carbon products generated from catalytic activation also increased to 1.58 cm^3/g for JP4, and most of the volume was composed of mesopores. Interestingly, the proportion and amount of micropores were highest at a KOH ratio of 2, and approximately 68% of the total volume consisted of micropores. Thus, micropores could be transformed into large size pores with an increase in catalyst ratio, while the BET surface area and total pore volume increased. This indicates that it might be possible to

selectively produce a micro- or meso-porous material for an intended purpose by controlling the catalyst ratio.

Figure 2-9 compares the pore size distribution (PSD) of carbon products before and after the activation process with different KOH ratios. From the PSD graph of fast pyrolysis char and non-catalytic activated carbon, a less developed porous structure was observed for both biomass types. During KOH activation, pores with width less than 30 Å were mainly generated, while the pore size of AC was relatively evenly distributed. The decrease in the pore distribution around 20-25 Å of catalytic activated carbon and AC is probably due to tensile strength effect generated by the structural properties as observed in the hysteresis loop in Figure 2-8, which has been reported in other studies (Cao et al., 2014; Groen et al., 2003; Li et al., 2016). The number of supra-nanometer pores significantly increased with increasing KOH ratio, specifically for JP-derived activated carbon rather than YP-derived product. Consequently, the results of this study suggest that fast pyrolysis char can be utilized to prepare highly active carbon materials with comparable properties to commercial activated carbon, and these materials are expected to show high performance in a variety of application fields.

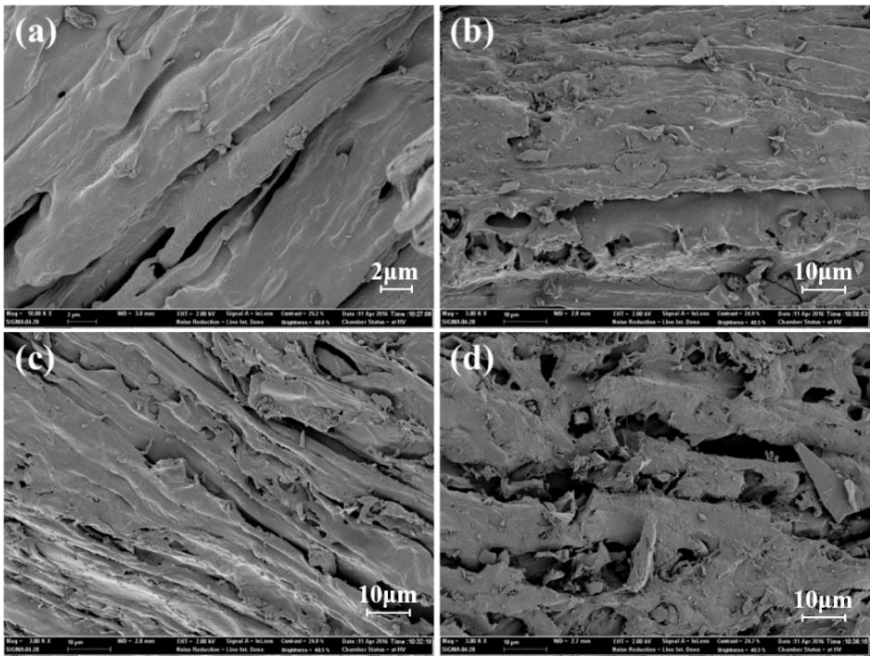

Figure 2-7. The morphological changes of pyrolysis char and activated carbon products ((a): YPC, (b): YP4, (c): JPC, (d): JP4).

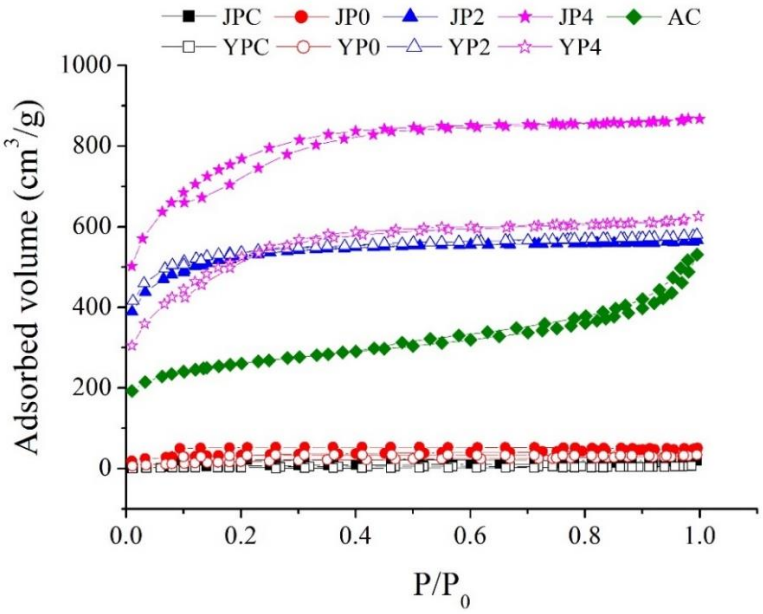

Figure 2-8. N_2 adsorption-desorption isotherms of the produced activated carbon and commercial activated carbon.

Table 2-5. Textural properties of activated carbon products obtained from pyrolysis char.

	S_{total}[a] (m^2/g)	$S_{external}$[b] (m^2/g)	V_{total}[c] (cm^3/g)	V_{micro}[d] (cm^3/g)	V_{meso}[e] (cm^3/g)	D_{avg}[f] (Å)
YPC	9	-	0.14	-	0.14	56.3
YP0	71	47	0.05	-	0.05	43.0
YP2	1825	504	0.90	0.61	0.29	25.4
YP4	1908	1670	0.97	0.08	0.89	23.2
JPC	27	-	0.03	-	0.03	51.4
JP0	116	75	0.08	0.02	0.06	42.9
JP2	1812	716	0.88	0.50	0.38	21.4
JP4	2711	1782	1.58	0.41	1.17	28.0
AC	900	446	0.82	0.21	0.61	49.8

[a] BET specific surface area measured by N_2 adsorption data in the P/P_0 range from 0.06 to 0.20.

[b] External surface area calculated using t-plot method.

[c] Total pore volume determined from the adsorption isotherm at $P/P_0 = 0.99$.

[d] Micropore volume calculated using t-plot method.

[e] Mesopore volume calculated by the difference between V_{total} and V_{micro}.

[f] Average pore diameter determined by the adsorption data using BJH method.

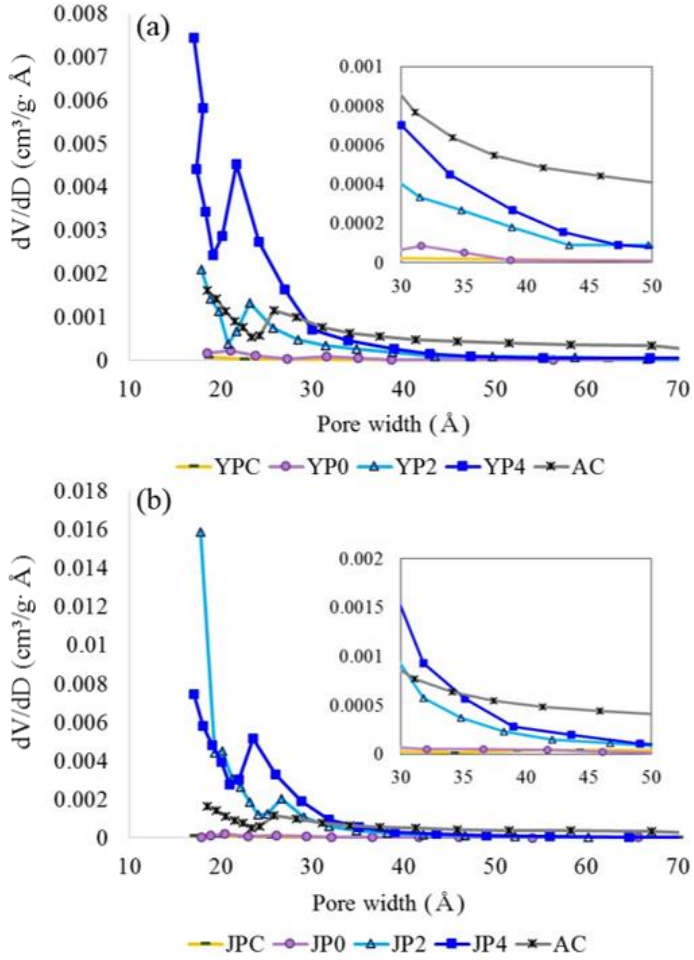

Figure 2-9. Pore size distribution of activated carbon ((a): YP-derived carbon products, (b): JP-derived carbon products; data was determined by BJH method from the adsorption branch).

3.5. Evaluation of phenol adsorption capacity comparing to commercial activated carbon

In order to investigate application potential of the produced activated carbon derived from fast pyrolysis char as natural adsorbent for water remediation, phenol removal test was conducted.

Figure 2-10 shows the phenol adsorption capacity of the carbon products and AC using 200 mg/L of phenol standard solution according to different contact times. The adsorption process proceeded rapidly and it reached equilibrium in the initial 30 min, remaining constant for following times. For fast pyrolysis char and non-catalytic activated carbon samples, adsorption uptake was low and the values were fluctuated probably due to weak-binding interaction caused by a lack of active sites therein. On the other hand, KOH-activated carbon products showed largely improved phenol adsorption capacity, which was higher than that of AC.

As for different solution concentration condition (25-200 mg/L), the amount of phenol uptake increased with an increase in the solution concentration, but a relative adsorption rate based on initial solution gradually decreased for all samples. Thus, it can be assumed that adsorption could be no longer carried out after a certain amount of adsorption had proceeded and not all reactive sites in carbon products could be bound to adsorbate.

In order to assess the efficiency of carbon products for phenol adsorption process, isotherm model study was carried out. Two adsorption isotherms, Langmuir (Eq. (2-3)) and Freundlich model (Eq. (2-4)) which are most frequently used (Li et al., 2011a; Li et al., 2011b; Nursam et al., 2016; Tan et al., 2017), were applied to determine the correlation between the adsorbed amount of phenol and the equilibrium concentration of solutions under different solution concentrations. The models equations are given as follows:

$$\frac{C_e}{Q_e} = \frac{1}{Q_m K_L} + \frac{C_e}{Q_m} \quad (2\text{-}3)$$

$$\ln Q_e = lnK_f + \frac{1}{n} lnC_e \quad (2\text{-}4)$$

where C_e (mg/L) and Q_e (mg/g) are the phenol concentration at equilibrium and the absorbed amount of phenol per 1 g of carbon product, respectively. K_L (L/mg) and K_f ((mg/g)(L/mg)$^{1/n}$) are the Langmuir and Freundlich constant. Q_m (mg/L) is calculated as the equilibrium concentration in the solution. The respective parameters of two models are presented in Table 2-6 and adsorption isotherms for all adsorbent samples was provided in Figure 2-11.

Fast pyrolysis char and non-catalytic activated carbon products did not matched isotherm models due to their unreliable adsorption behavior. For KOH-activated carbon products, however, it can be observed that Langmuir isotherm model described adequately with high R^2 value. Thus, adsorption of phenol could occur through monolayer coverage with identical affinity for the adsorbate on a homogeneous surface of activated carbon products in this study. This result also corresponds to other previous studies (Abussaud et al., 2016; Hameed & Rahman, 2008; Hsieh & Teng, 2000).

In addition, JP4 showed the highest adsorption capacity (Q_m), 625.0 mg/g, which was higher than that of AC (500.0 mg/g). This result was also superior to that of other researches, the adsorption capacity of 243.47 mg/g (Yang et al., 2014) and 149.25 mg/g (Hameed & Rahman, 2008) for phenol obtained by using wood- and rattan-based activated carbon, respectively. Thus, changes in structural features of char precursor during KOH activation significantly influenced on the adsorption capacity. Specifically, highly improved specific psurface area and aromaticity could lead to an increase in π-π dispersion interaction as well as reaction between active site and adsorbate, major mechanisms related to phenol adsorption.

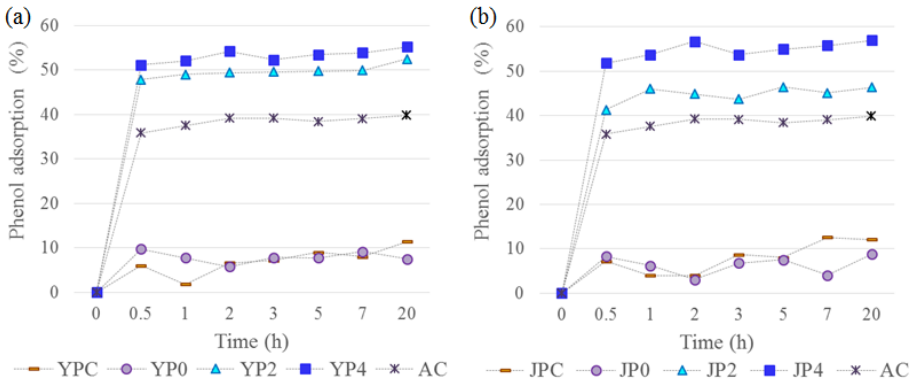

Figure 2-10. Evaluation of phenol adsorption capacity on carbon products according to contact time ((a): Activated carbon from fast pyrolysis char of yellow poplar, (b): Activated carbon from fast pyrolysis char of Japanese red pine).

Table 2-6. Langmuir and Freundlich adsorption parameters of phenol for carbon products and commercial activated carbon.

	Langmuir model			Freundlich model		
	Q_m (mg/g)	K_L	R^2	n	K_f	R^2
YPC	6.2	0.040	0.9867	0.74	1.285	0.4387
YP0	5.0	0.004	0.9310	0.39	2.389	0.8750
YP2	208.3	0.119	0.9994	2.82	46.647	0.9989
YP4	454.5	0.186	0.9999	3.82	148.295	0.9770
JPC	7.4	0.005	0.4789	0.74	1.740	0.5320
JP0	36.9	0.005	0.9077	0.37	2.418	0.7521
JP2	192.3	0.111	0.9992	1.82	41.758	0.9940
JP4	625.0	0.038	0.9996	1.96	54.533	0.9989
AC	500.0	0.075	0.9798	2.55	84.513	0.9391

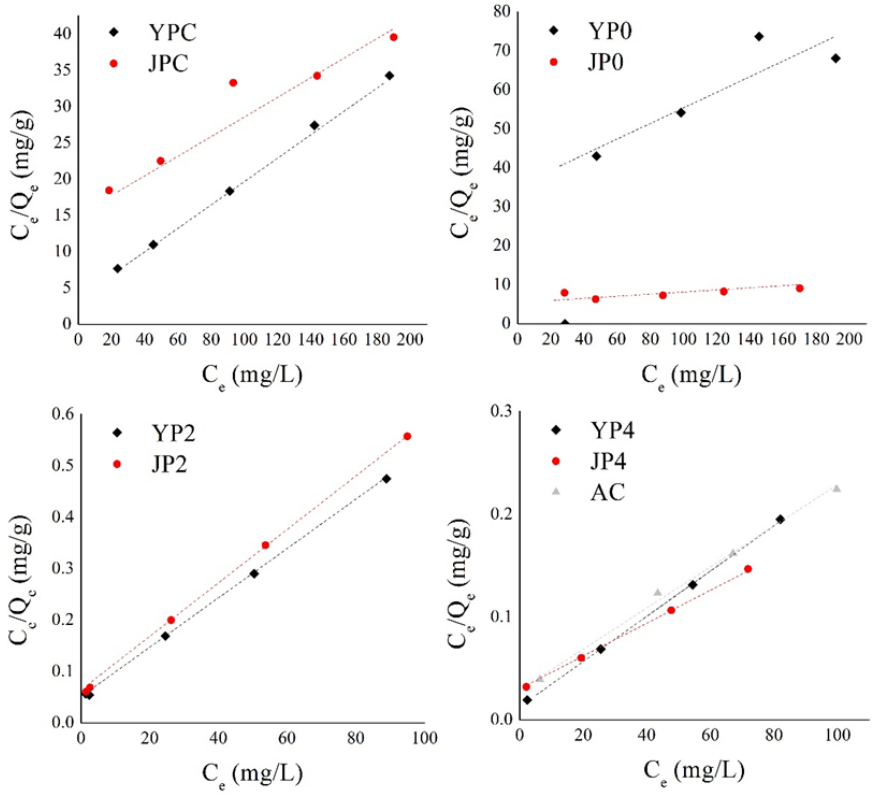

Figure 2-11. Adsorption isotherm for phenol onto activated carbon derived from fast pyrolysis char (The dotted line : Langmuir fits).

To further study on the correlation between features of carbon product and adsorption capacity (Q_m), principal component analysis (PCA) was conducted by SPSS software. Two components was obtained with a description of 96.8 % for overall data set. As shown in Figure 2-12, the value has a correlation with V_{meso}, aromaticity determined by I_d/I_g ratio, .$S_{external}$, and V_{total}. Generally, micropore has been considered as a dominant factor impacting the adsorption behavior because it could provide adsorptive sites rather than mesopore. However, mesopore can play an important role in enhancing adsorption capacity by expanding diffusion path for adsorbate to reach active sites (Hsieh & Teng, 2000). Therefore, a creation of mesopore in carbon product during the process could make the phenol adsorption reaction more favorable by enhancing rapid mass transfer as well as pore accessibility.

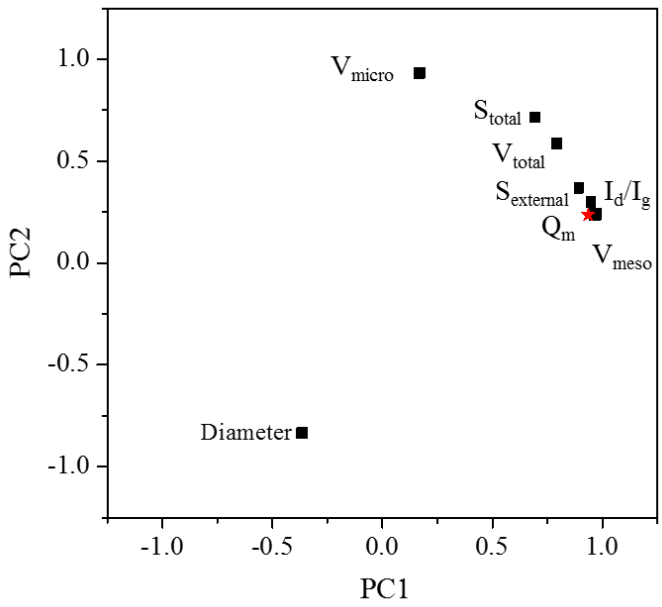

Figure 2-12. Plot from principal component analysis of Langmuir isotherm Q_m and properties of activated carbon prepared from fast pyrolysis char.

4. Conclusions

An approach to structural assessment of nanoporous activated carbon derived from fast pyrolysis char under various catalyst loadings and its application to natural adsorbent for phenol removal was carried out. As a result of Py-GC-MS analyses, an increase in release of aromatic hydrocarbons including a considerable proportion of BTEX were determined, which could be attributed that carbon-carbon bonds in solid char is more likely to be cleaved by KOH catalyst. After the activation process, a high-degree aromatic structure compared to AC was developed with a KOH ratio of 4. Moreover, successful production of microporous or mesoporous carbon material was accomplished with the maximum BET surface area of 2711 m^2/g (JP4), and the created pore size was largely influenced by catalyst loading. As for phenol removal, JP4 showed higher adsorption capability than that of AC and Langmuir model was more suitable to describe adsorption process in this study. In addition, a correlation between V_{meso}, aromaticity, .$S_{external}$, V_{total} and Q_m value from Langmuir model was observed. The results of this study suggest that fast pyrolysis char, co-product of the process, can be utilized to prepare a superior natural adsorbent for phenol as well as highly active carbon materials comparing to AC, and the carbon materials are expected to be applied low-cost and high performance in a variety of application fields.

Chapter 3

Facile surface modification of nanoporous carbon prepared from a co-product of biofuel technologies for efficient biosorbents and carbon electrodes

1. Introduction

Biomass can be converted to liquid fuel through thermochemical processes and has potential to replace fossil fuels with a reduction in greenhouse gas emissions. Fast pyrolysis is one of the most promising conversion processes currently available to produce liquid fuel with high yield. Hydrothermal liquefaction is another process by which to generate a liquid fuel and is suitable for wet biomass under mild conditions by using super- or sub-critical water as a solvent (Toor et al., 2011). Although both processes have been optimized for liquid fuel production, a significant amount of solid char with high carbon content is also obtained (Hwang et al., 2013; Hwang et al., 2015; Lee et al., 2016) as a valuable co-product that can be utilized with further treatment for water remediation (Dąbrowski et al., 2005; Lima et al., 2010) or serve as an electrode material (Wang & Kaskel, 2012). Char has received less research attention than liquid fuels; thus, there are few studies regarding its value-added utilization, except for heat production via direct combustion.

Current research has investigated the characterization of pyrolysis char and hydrochar (solid products from fast pyrolysis and hydrothermal liquefaction, respectively) (Azargohar et al., 2014; Kambo & Dutta, 2015; Kim et al., 2012). Since the pyrolysis reactions in previous studies were carried out under a different reaction medium, temperature, or involved a different decomposition mechanism, the char products significantly differ from each other in terms of chemical and physical properties. The reaction pathway of fast pyrolysis is based on a free-radical process derived from homolytic cleavage of chemical bonds in biomass (Shafizadeh, 1982). On the other hand, the reaction during hydrothermal liquefaction is initiated by hydrolysis of macromolecules, followed by dehydration and condensation in a state of spherically shaped particles (Sevilla & Fuertes, 2009). As a result, hydrochar has a larger number

of functional groups, higher acidity, and lower aromaticity and thermal stability than pyrolysis char. These properties are important to consider for utilization of the products in the proper application field.

Meanwhile, there is a limit in the extent to which char products can be used in industrial purposes due to the relatively low specific surface area, which could result in unsatisfactory performance (Essandoh et al., 2015; Lima et al., 2010; Liu et al., 2010). To overcome this disadvantage, further steps to develop ordered inner and surface structures are required. Activation is one of the representative processes by which to create porosity of a carbonaceous material. Several studies have investigated the preparation of activated carbon using co-products generated in the production of biofuels (Jain et al., 2016; Lima et al., 2010; Zhu et al., 2014). Previous studies focused on investigating the properties of activated carbon products and/or testing the application of single samples.

Surface functionalities are important for improving the availability of activated carbon by enhancing the reactivity with other substances. An acid-modification treatment can provide oxygenated functional groups to the carbon surface and play an important role in the adsorption capacity and conductivity of carbon electrode material by increasing ion accessibility (Lin et al., 2011; Wang et al., 2007). However, the conventional method for acid-modification requires additional steps that complicate the process; thus, a modification method performed simultaneous to the preparation of activated carbon itself needs to be investigated.

In our previous work, a study on characterization and structural development behavior of activated carbon using fast pyrolysis char from two biomasses and a correlated study between its properties and adsorption capacity were conducted (Hwang et al., 2017). It was revealed that the production of activated carbon was highly affected by precursor type, and the different properties closely correlated with adsorption capacity. Correa et al. (Rodríguez Correa et al., 2017) also investigated the effect of carbonization (hydrothermal

carbonization and pyrolysis) on the surface area and chemistry of activated carbon, but did not demonstrate potential for application. In this respect, this study focused on a comparison of activated carbon derived from two different pre-carbonization processes, fast pyrolysis and hydrothermal liquefaction, as a first step in the thermal conversion mechanism, aromaticity, surface functionalities, and pore and surface areas. In addition, an approach facilitating simultaneous surface development by zero air conditions during this process was attempted, and its feasibility as a facile modification was assessed and compared to post-acidification. Furthermore, potential applications of the produced activated carbon for value-added fields, biosorbents, and carbon electrodes were evaluated, and the effects of varied surface and pore properties on the utilization performance were discussed.

2. Materials and methods

2.1. Fast pyrolysis and hydrothermal liquefaction for char production

Larch provided from the Kwanak Arboretum at Seoul National University in Korea, was used as a raw material for producing the precursor char for activated carbon. Biomass was ground to a size of 5 mm by a cutting mill and subjected to two different biofuel production processes, fast pyrolysis and hydrothermal liquefaction.

First, fast pyrolysis was conducted using a fluidized bed-type reactor at 500°C with a residence time of 1.3 s under a N_2 flow of 10 L/min. Biomass was fed into the reactor and converted to volatile compounds to be condensed as liquid oil. The solid was separated by a cyclone connected to the reactor and recovered from a char collector in a furnace after the process.

Next, hydrothermal liquefaction was carried out using a batch-type reactor at a size of 500 cc. De-ionized water (D.I. water) was added as a solvent at a ratio of 10:1 based on biomass (w/w), and the reactor was sealed. N_2 gas was then purged several times in order to maintain an inert state before the process. The reaction was carried out at 300°C for 30 min, with constant stirring at 300 rpm during the process. After the reaction, the reactor was quenched in an ice water bath to cool it to room temperature. The product mixture including liquid oil, a water phase, and solid was diluted with 250 mL of methylene chloride, and the solid product was filtered using a vacuum filter system.

The solid carbon products obtained from fast pyrolysis and hydrothermal liquefaction were referred to as pyrolysis char (PC) and hydrochar (HC), respectively.

2.2. Thermogravimetric and volatile-release analyses of PC and HC during catalytic thermal degradation

In order to investigate the structural degradation process when a precursor, PC or HC, is converted to activated carbon, thermogravimetric (TG) and differential thermogravimetric (DTG) analyses and pyrolysis-gas chromatography-mass spectrometry (Py-GC-MS) were conducted. Each precursor char was mixed with KOH (Sigma Aldrich) in a ratio of 1:4 (char:catalyst, w:w), and the mixtures were used in both experiments.

For TG-DTG analyses, a sample mixture of about 10 mg was placed in a crucible in the instrument chamber (TGA/DSC 3+(LF-1100) (Mettler-Toledo AG, Switzerland)), and the change in weight according to temperature was observed at a heating rate of 10°C /min up to 700°C under a nitrogen atmosphere.

The identification of released volatile compounds from PC and HC samples during thermal decomposition with or without catalyst was conducted using a Py-GC-MS equipped with a coil-type CDS Pyroprobe 5000 (CDS Analytical Inc., Oxford, PA, USA) and GC–MS/FID (Agilent Technologies 7890A/Agilent Technologies 5975A, USA) with a DB-5 capillary column (30 m × 0.25 mm ID × 0.25 μm film thickness).

A 15 mg sample mixture was put into a quartz tube that was then stoppered with glass wool on both sides. An internal standard (1.3 mg of fluoranthene/mL of methanol) was added to each sample in the tube and then pyrolyzed to 700°C at a heating rate of 10°C/ms for 20 s. The oven temperature was maintained at 50°C for 5 min, increased at a heating rate of 3°C/min to 280°C, and was held there for 10 min. The volatile compounds were identified based on NIST MS Search 2.0 (NIST/EPA/NIH Mass Spectral Library; NIST 02), and a quantitative analysis was conducted with consideration of response factors (Rf)

of each compound, as suggested in a previous study (Kim et al., 2015). The amount of volatiles released from the char with different catalyst ratios was calculated with the following equation:

$$\text{Amount of volatiles } (\mu g/\text{g char}) = \text{Rf} \times \frac{A_{volatiles}}{A_{I.S}} \times \frac{Q_{I.S}\ (\mu g)}{Q_{char}\ (g)} \qquad (3\text{-}1)$$

where Rf is the response factor, $A_{volatiles}$ and $A_{I.S}$ are the peak areas of the volatile compounds and internal standard, respectively, and $Q_{I.S}$ and Q_{char} are the amounts of internal standard and char sample.

2.3. Preparation of activated carbon

2.3.1. Catalytic activation under different atmospheric conditions

Activated carbon was produced from PC and HC by chemical activation using KOH as a catalyst. The precursor char sample and KOH were added to a batch-type reactor at a ratio of 1:4 (char:catalyst, w:w). The atmospheric condition was controlled by N_2 or zero air (extremely pure without hydrocarbons or moisture) at a flow rate of 250 mL/min. The reactor was put into the furnace and heated to 700°C, with the reaction gas continuously circulated during the process. After 2 h, the reactor was removed from the furnace and cooled. The residue mixture within the reactor was washed using 1 M of HCl solution and D.I. water and collected with a vacuum filter. Finally, the activated carbon product was obtained after drying overnight in an oven. The products were named N_2-activated pyrolysis char (NPC), N_2-activated hydrochar (NHC), air-activated pyrolysis char (APC), and air-activated hydrochar (AHC) based on atmospheric conditions and the type of precursor.

2.3.2. Post-modification by acid treatment

For modification of the surface functionalities of N_2-activated carbon samples, post-acid treatment using HNO_3 solution was conducted using a modified method suggested in previous research (Ternero-Hidalgo et al., 2016). Activated carbon (1.0 g) was put in the flask with 50 ml of 5 M HNO_3, and the flask was heated in a water bath at 80°C for 3 h. Then, each sample was washed thoroughly with D.I. water while filtering. The acid-treated samples were recovered after drying overnight and are referred to as NPC-A and NHC-A, respectively.

2.4. Characterization of activated carbon

The elemental composition (C, H, and N) of the carbon samples was analyzed using a US/CHNS-932 (LECO, USA), and the ratio of oxygen was calculated by the difference. The surface functionalities of the carbon samples were determined by Fourier transform infrared spectroscopy (FT-IR; Nicolet 6700, Thermo Scientific, USA) equipped with attenuated total reflectance (ATR). All spectra for each sample were collected over a range of 600 to 4000 cm^{-1} with an 8 cm^{-1} resolution and 32 scans. In addition, X-ray photoelectron spectroscopy (XPS) was performed using AXIS-HSi (KRATOS, UK) to study the binding energies of C1s photoelectrons of the surface groups on the carbon products. For structural analysis, Raman spectroscopy was carried out using LabRAM HV Evolution (HORIBA Scientific, Japan) with an Ar Laser (514 nm) in the range of 1000-1800 cm^{-1}.

High-resolution field-emission scanning electron microscopy (FESEM) of the samples was performed using a SIGMA instrument (Carl Zeiss, UK). The texture features were determined by Brunauer-Emmett-Teller (BET) analysis of specific surface area from N_2 adsorption, the Barrett-Joyner-Halenda (BJH) method for pore size and average diameter using an adsorption branch, and the t-plot method for micropore structure using an ASAP 2010 (Micrometrics, Canada) under a N_2 adsorption-desorption isotherm at 77 K.

2.5. Evaluation of Pb^{2+} adsorption efficiency and electrochemical properties

Pb^{2+} adsorption tests for char precursors and the produced activated carbon including post-modified carbon were carried out in a simple batch-type experiment. First, Pb^{2+} standard solution (50 ppm) was prepared using $Pb(NO_3)_2$ (Sigma Aldrich). Each carbon sample was added into the solution at a dose of 1 g/L, and the mixture was agitated at 28°C for 12 h at 150 rpm. After the test, the mixture was filtered, and the filtrate was analyzed by inductively coupled plasma-emission spectroscopy using an ICPS-1000IV instrument (Shimadzu, Japan) to calculate the remaining lead ion concentration.

In addition, coated-type electrode samples were fabricated to measure the electrochemical properties of carbon samples in this study. All carbon samples were ground into a fine powder and mixed with polytetrafluoroethylene (PTFE; binder) and carbon black (conducting material) at a ratio of 85:10:5 (w/w). Then, 400 μl of ethanol was added to produce an electrode slurry that was then sonicated for 2 h to ensure complete mixing. After the slurry was pasted onto the Ni-foam current collector, it was dried in an oven overnight. Thereafter, it was pressed at 10 MPa for 1 min to prepare a final electrode sample with a mass loading of about 10 mg/cm^2. Electrochemical characteristics were determined by a three-electrode system using 6 M KOH aqueous solution as an electrolyte. The prepared electrode sample served as a working electrode, and Pt wire and Ag/AgCl were used as a counter and reference electrode, respectively. Cyclic voltammetry (CV) was performed using a VersaSTAT4-200 (Princeton Applied Research, USA) electrochemical workstation. The voltage range for CV was varied from -1.0 to 0 V at a scan rate of 10 mV/s. The gravimetric specific capacitance was calculated by equation (3-2).

$$\text{Specific capacitance (F/g)} = \frac{\int iv\,dv}{2\mu m\Delta V} \quad (3\text{-}2)$$

where i and v are the current and potential, respectively, in the CV test (total area of curve); μ is the scan rate (V/s); m is the mass of the carbon sample (g); and ΔV is the width of the potential window (V). In addition, coin cell type electrode was also prepared by using modified method as reported in a previous study (Han et al., 2017).

Figure 3-1 shows the overall scheme for this study, consisting of preparation of precursor char, structural degradation analysis, N_2 and air activation, post-surface modification, and application. All experiments were conducted in duplicate, and average values are presented.

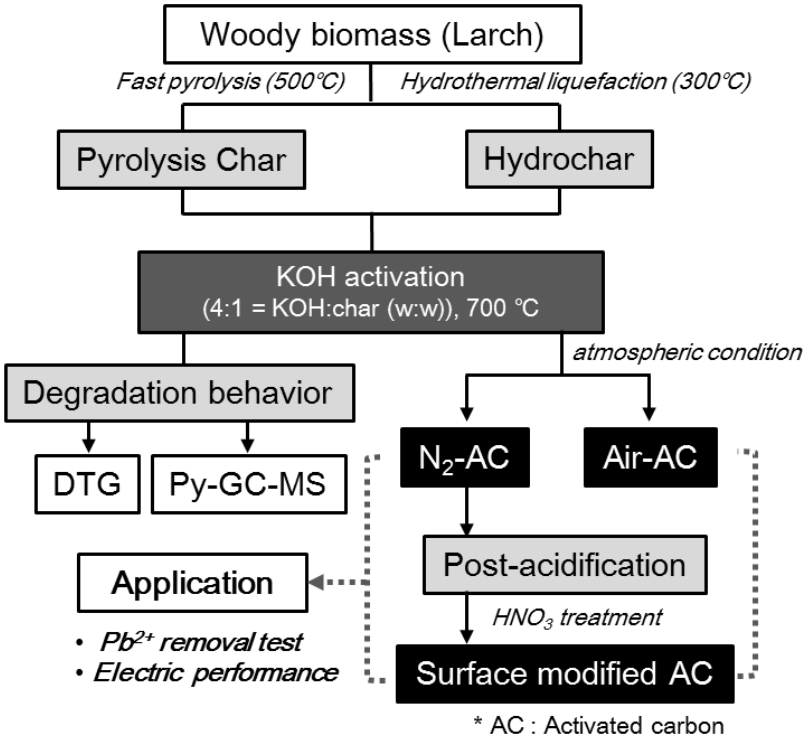

Figure 3-1. Overall schematic procedure to investigate the effects of pre-carbonization steps and reactive gas on properties of activated carbons and their application.

3. Results and discussion

3.1. Changes in the thermal stability and volatile release of HC and PC by catalytic thermal decomposition

In order to more specifically understand the thermal decomposition mechanisms of PC and HC as a precursor for KOH-activated carbon, DTG and Py-GC-MS analyses were conducted before any process applications. Figure 3-2 shows the DTG curves of different precursors with or without catalyst.

In the case of HC, decomposition began above 320°C, whereas that of PC was almost linear. At the final temperature of 700°C, the residual solid amount for HC was calculated as 12.7 wt.%, while a higher amount of 87.8 wt.% was left for PC. These results could be attributed to differing reaction temperatures, 500°C and 300°C for PC and HC, respectively. Generally, 300°C is not high enough to break down all components of biomass other than hemicellulose units or glycosidic linkages of cellulose (Arseneau, 1971; Nair et al., 2000). Thus, the weight loss of HC was probably due to the degradation of its rigid structure such as the cellulose crystalline region or lignin complex remaining after hydrothermal liquefaction.

With the addition of catalyst, both HC and PC were remarkably decomposed at a relatively low temperature range of 160-250°C. A similar tendency was observed in our previous study (Hwang et al., 2017), which indicates that KOH facilitates the cleavage of propanoid side chains, aryl ether, and C-C bonds in precursors (Brežný et al., 1984; Fiddler et al., 1967; Ludwig & Sarkanen, 1971). In addition, the main weight loss temperature for HC was 160°C, whereas additional points of 217°C and 253°C appeared for PC. The weakest side chain, such as an ether bond, would likely be broken at a lower temperature, while the

relatively thermally stable C-C bonds are broken at higher temperatures; thereby, PC consists of a more condensed structure with a higher thermal stability than HC.

The volatile compounds released from HC and PC during KOH-thermal decomposition were identified and are quantified as shown in Table 3-1. Volatile aromatic compounds containing 6 kinds of aromatic hydrocarbons (AH) and 7 kinds of oxygenated aromatics (OA) were detected by the decomposition of precursors. These OAs were only detected only from HC, which was probably due to degradation of the residual carbohydrates, while these were not observed in PC with a condensed structure.

With the addition of catalyst, the amount of AH from both precursors increased, while the amount of OA released from HC was reduced markedly from 18.26 μg/g to 2.56 μg/g. This could be explained by the finding that potassium can act as an electron acceptor, which reduces energy barriers for the dehydration reaction (Nimlos et al., 2003). Thus, bonding cleavage could be facilitated in the presence of catalyst. Specifically, the amounts of 4 major compounds of OA (2,4-dimethylphenol, 3,4-dimethylphenol, 3-methylpyrocatechol, and 4-methylpyrocatechol) significantly decreased, whereas those of benzene, toluene, and xylene (BTX) increased. Therefore, it can be assumed that those OA compounds (xylenols and catechols) were converted to AH (BTX) by dehydration through inter-molecular cleavage promoted by catalyst. In addition, an increase in AH could also have resulted from further fragmentation of the polycyclic structure of the precursors. As can be seen in the data of PC, an amount about 1.6 times higher was detected with the addition of catalyst. Among those, an increase in benzene, which had no side chain, was the largest.

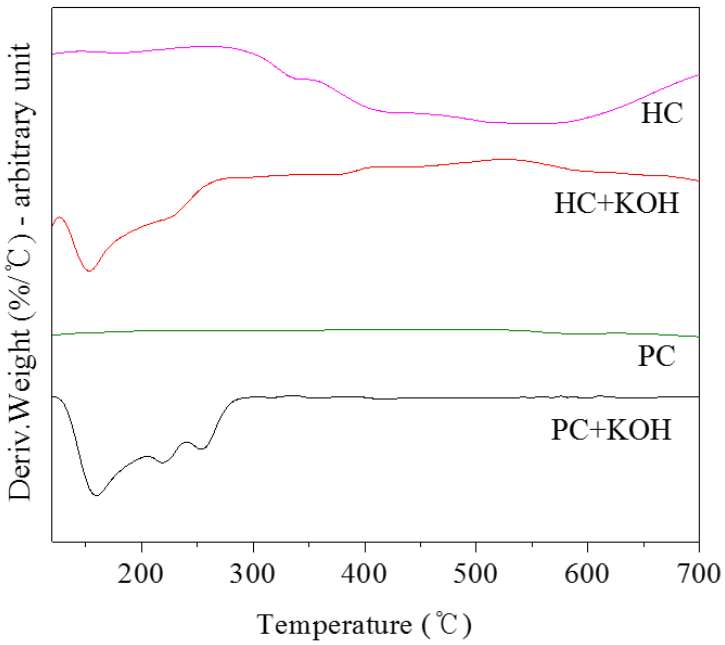

Figure 3-2. DTG curves of HC and PC before and after the addition of KOH catalyst.

Table 3-1. Volatile compounds released from catalytic thermal conversion of PC and HC by Py-GC/MS analysis.

Type	Compound	PC	PC w/ KOH	HC	HC w/ KOH
AH[a]	Benzene	0.30	0.68	0.55	1.94
AH	Toluene	0.21	0.25	0.62	2.30
AH	Ethylbenzene	0.04	0.03	0.09	0.53
AH	p-Xylene	0.03	0.03	0.26	1.19
AH	Styrene	0.08	0.02	0.16	0.69
AH	1,3,5-Trimethylbenzene	0.00	0.00	0.17	0.44
	Total AH	**0.65**	**1.01**	**1.85**	**7.09**
OA[b]	2,5-Dimethylfuran	0.00	0.00	0.14	0.04
OA	Phenol	0.00	0.00	0.62	0.35
OA	o-Cresol	0.00	0.00	0.66	0.53
OA	2,4-Dimethylphenol	0.00	0.00	3.00	0.64
OA	3,4-Dimethylphenol	0.00	0.00	1.16	0.54
OA	3-Methylpyrocatechol	0.00	0.00	3.28	0.30
OA	4-Methylpyrocatechol	0.00	0.00	9.41	0.17
	Total OA	**0.00**	**0.00**	**18.26**	**2.56**
	Total	**0.65**	**1.01**	**20.11**	**9.65**

[*] Unit : μg/g

[a] AH: Aromatic hydrocarbon

[b] OA: Oxygenated aromatics

3.2. Chemical activation of PC and HC under different atmospheric conditions

The yield of activated carbon products from PC and HC with the addition of KOH is given in Figure 3-3 according to conditions of N_2 and zero air. The highest yield was 48.4 wt.% for PC under N_2, and the lowest yield was 17.1 wt.% for HC under air. This could be due to the thermally labile structure of HC. As for atmospheric conditions, the generation of activated carbon was considerably lower under air conditions, which can alter the reactivity of the carbon surface and are liable to produce gaseous products. As atmospheric conditions and precursor type affect the production of activated carbon, it is also expected that the structures of the products will be different.

The carbon recovery rate was calculated from data pertaining to the yield and elemental analysis and can be considered as an indicator of functional group loss and carbon fixation after activation. As shown in Figure 3-3, the rate was similar or higher comparing to each product yield, indicating that weight loss due to other elements occurred more frequently than that due to carbon after the activation process.

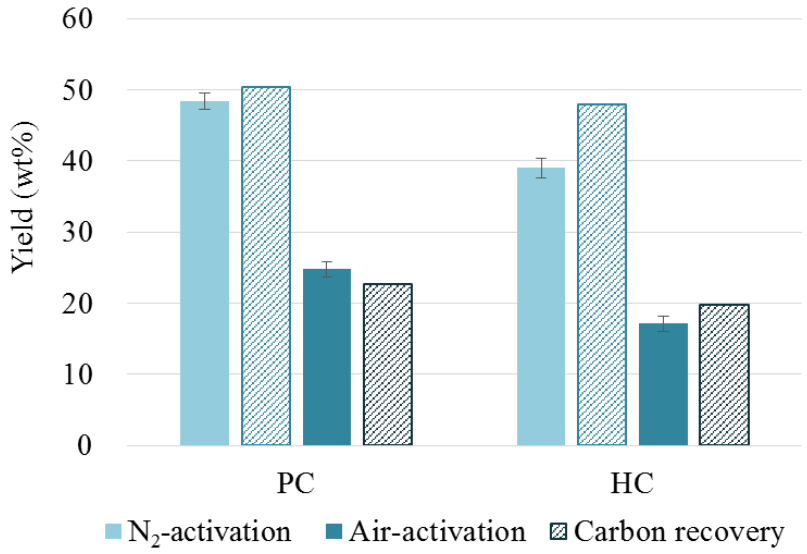

Figure 3-3. Yield and carbon recovery rate after N_2 or air activation of PC and HC.

3.3. Characterization of carbon products after the activation process and post-modification

3.3.1. Elemental composition and surface functionalities

After post-modification of surface functionalities of N_2-activated carbon products, NPC-A and NHC-A samples were characterized and compared with other carbon products. A Van krevelen diagram was drawn to investigate changes in elemental composition related to degree of carbonization. As can be seen in Figure 3-4, HC has a lower carbon content and a higher oxygen content, which means it has more functional side chains than PC. Thus, PC has more C-C cross-linked structure, resulting in high thermal stability, as determined by the DTG and Py-GC-MS results. Meanwhile, dehydrogenation of both precursor chars was induced by chemical activation, and N_2 activation led to a product with higher carbon-intensive material than air activation. On the other hand, post-modification by acid treatment oxidized NPC and NHC, so high H/C and O/C values of NPC-A and NHC-A are shown on the graph.

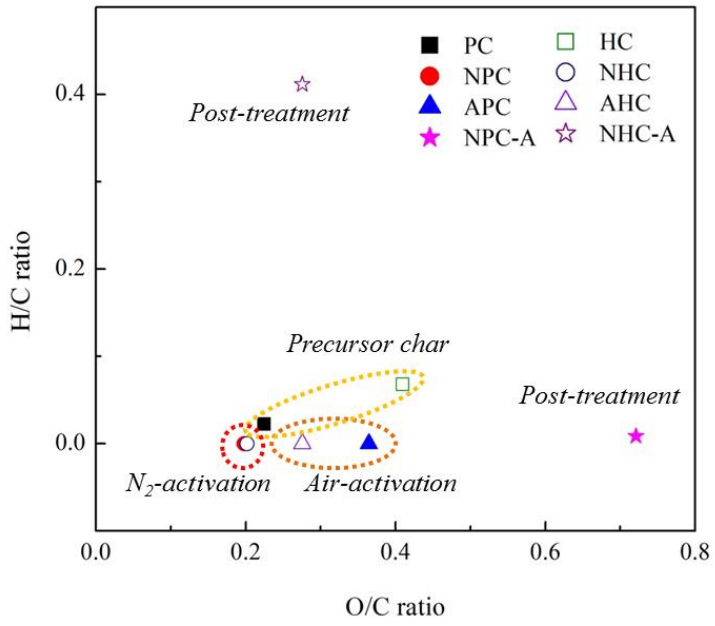

Figure 3-4. Van Krevelen diagram of carbon samples.

Figure 3-5 and Table 3-2 show changes in surface functionalities of the carbon products analyzed by FT-IR and XPS analysis, respectively. A large number of functional groups were observed in HC in contrast to PC; in particular, C-O or phenyl alkyl ether groups at 1048 cm^{-1} and 1270 cm^{-1}, conjugated C=C or stretching C=C bond at 1580 cm^{-1}, conjugated aromatic carbonyl and carboxyl group at 1725 cm^{-1}, aliphatic CH_x asymmetric stretching vibration at 2900 and 2975 cm^{-1}, and –OH stretching vibration at 3400 cm^{-1} were observed (Gomez-Serrano et al., 1996; Lin et al., 2014; Pavia et al., 2008). After the activation process, the peaks nearly disappeared. Only small peaks around 1045, 1600, 2900, and 2975 cm^{-1} remained, which represent aromatic ring and aliphatic carbons (Gomez-Serrano et al., 1996; Lin et al., 2014; Pavia et al., 2008). Meanwhile, the post-modification treatment certainly introduced hydrophilic functional groups to the carbon products. Almost all of the peaks present in HC were observed in NPC-A and NHC-A, although their intensities were much greater. Specifically, peaks around 1040, 1226, 1600, 1725, and 3400 cm^{-1}, which correspond to ether, carbonyl, and hydroxyl groups (Gomez-Serrano et al., 1996; Lin et al., 2014; Pavia et al., 2008), were identified as main peaks.

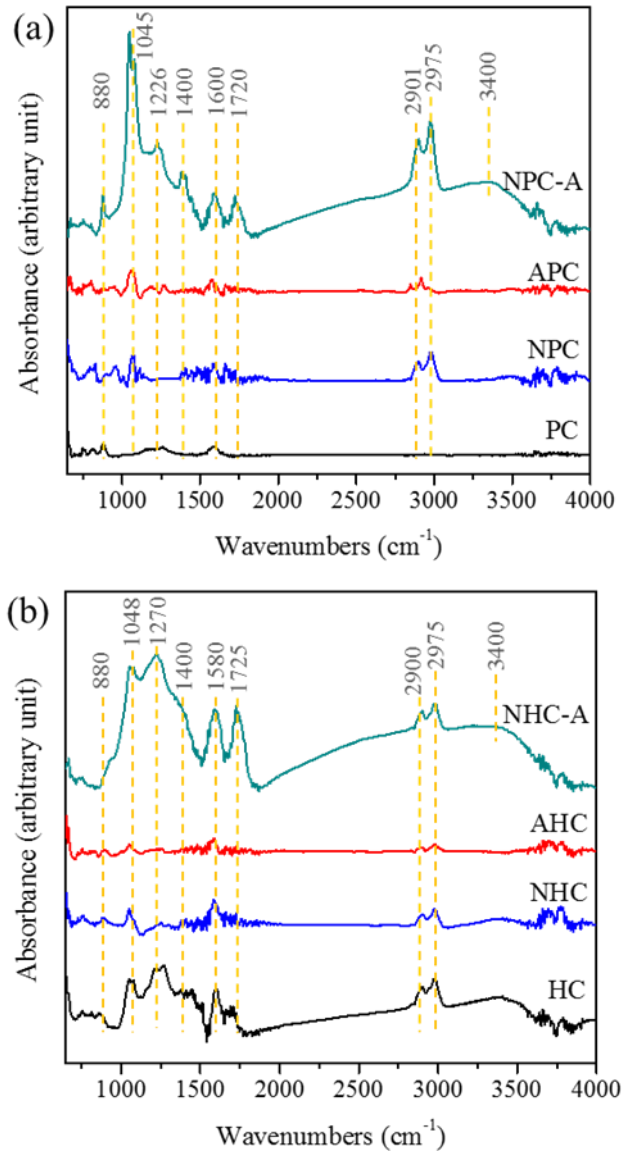

Figure 3-5. FT-IR spectra of precursor char and activated carbon samples ((a) carbon products derived from fast pyrolysis char, (b) carbon products derived from hydrochar).

An XPS analysis was conducted to better understand the chemical bonding composition of the carbon product, and the curve of high-resolution of C1s spectra was fitted to five peaks. The main peak C1s(1) was attributed to sp^2-graphitic or C-C bond (284.6 eV), and peaks C1s(2), C1s(3), C1s(4), and C1s(5) were assigned to C-O (286.0 eV), C=O (286.6 eV), O=C-O (288.9 eV), and carbonates (289.5 eV), respectively. The relative contents of each component are shown in Table 3-2.

For precursor char, all components in HC over 70 % represented oxygen-related bonding. Thus, HC has a number of functional groups, consistent with the FT-IR results of carboxyl and carbonyl groups at 1400 and 1700 cm^{-1} for C1s(2), C1s(3), and C1s(4) peaks. After chemical activation, the C1s(1) peak for graphitic carbon increased, which indicated development of a carbonized and aromatic structure. Since N_2-activated carbon has more carbon-related bonding than air-activated carbon, it can be assumed that the hydrophobicity of N_2-activated carbon is higher. However, the C1s(1) peak decreased drastically during the post-modification process, while oxygen-related components increased. A new peak of C1s(4) appeared and corresponds to O=C-O groups in carboxyl or ester groups, as also shown in the FT-IR graph at 1700 cm^{-1}. Therefore, it was determined that surface oxidation by acid treatment successfully provided hydrophilic functional groups to the surface of the activated carbon product.

Table 3-2. Chemical composition of raw precursors, activated carbon, and post-treated activated carbon by XPS spectra.

Chemical composition (%)	C1s(1)	C1s(2)	C1s(3)	C1s(4)	C1s(5)
	sp^2-graphitic or C-C, C-H	C-O	C=O	O=C-O	CO_3^{2-}
PC	71.1	22.8	6.1	-	-
NPC	82.8	14.6	2.6	-	-
APC	74.1	20.3	2.9	2.7	-
NPC-A	66.6	26.9	0.9	5.6	-
HC	29.7	23.1	42.1	5.1	-
NHC	77.3	18.4	4.3	-	-
AHC	75.1	17.6	7.3	-	-
NHC-A	69.4	11.3	6.2	5.6	7.5

3.3.2. Structural features

Raman spectroscopy provides information about chemical bonding, symmetry of molecules, and crystallographic orientation of solid carbon samples. The curve fitting of the Raman spectra with five Gaussian bands was carried out and represents typical structures, as shown in Figure 3-6 (Lin-Vien et al., 1991; Tuinstra & Koenig, 1970; Wang et al., 1990). The deconvoluted bands were as follows; the D peak at 1320 cm^{-1} indicated the condensed benzene region, C-C between aromatic rings, and aromatics with no fewer than 6 rings; the V_R peak at 1380 cm^{-1} represented semi-circle breathing of aromatic rings and methyl groups in amorphous carbon structures; the V_L peak at 1465 cm^{-1} indicated semi-circle breathing of aromatic rings and methylene groups in amorphous carbon structures; the G_R peak at 1540 cm^{-1} was for aromatics with 3-5 rings and amorphous structures; and the G peak at 1580 cm^{-1} represented graphite, aromatic ring quadrant breathing, and alkene C=C bonds (Lin-Vien et al., 1991; Tuinstra & Koenig, 1970; Wang et al., 1990). The ratios of intensities were calculated for semi-quantitative evaluation of changes in carbon structure, and Figure 3-7 presents the ratio values of the carbon products in this study.

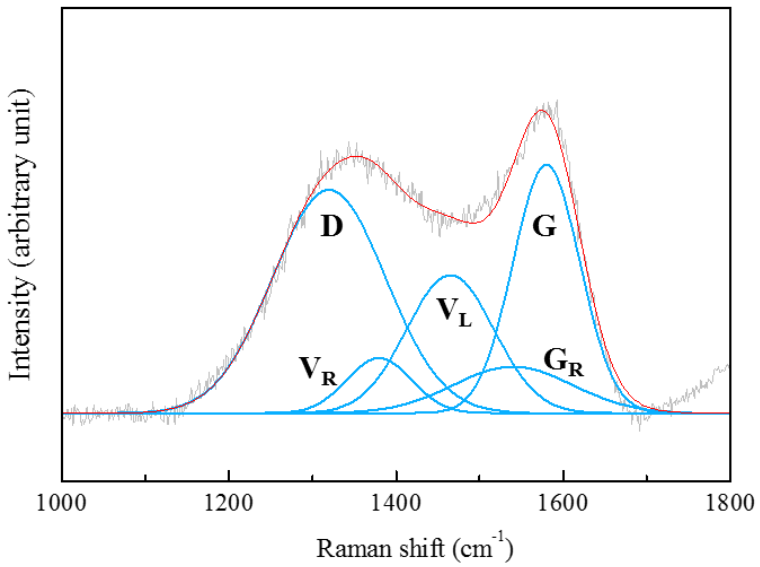

Figure 3-6. The deconvolution of Raman spectra by 5 Gaussian bands.

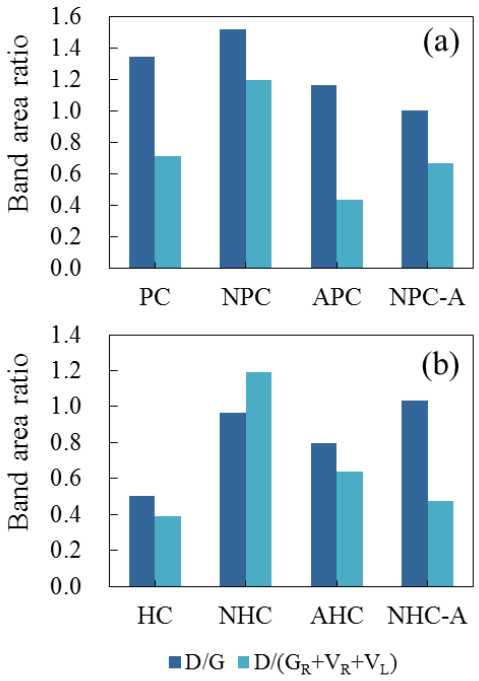

Figure 3-7. Raman peak ratio of carbon samples ((a) carbon products derived from fast pyrolysis char, (b) carbon products derived from hydrochar).

Compared to PC, the D/G and D/(G_R+V_R+V_L) ratios of HC were lower, indicating that the aromatic structure was less developed in HC. After N_2 activation, both ratios increased; thus, it can be assumed that aromatic rings with a disordered carbon lattice were enlarged by intra- and inter-molecular rearrangement of the structure through dehydrogenation and deoxygenation facilitated by the catalyst. The ratios of APC and AHC were lower than those of N_2-activated products, particularly the D/(G_R+V_R+V_L) ratio; thus, a graphite-like structure and a small aromatic ring system were better formed under air, possibly due to incomplete polymerization. In addition, a decrease in the D/(G_R+V_R+V_L) ratio of post-treated carbon samples was observed. Therefore, structural deformation occurred by acid treatment, which could result in the loss of a defective region and a large quantity of small aromatic ring structures grafted with alkyl groups due to introduction of functional groups. Considering the results from surface and structural analysis in this study, the plausible chemical structure of activated carbon products developed by activation and post-modification was suggested in Figure 3-8.

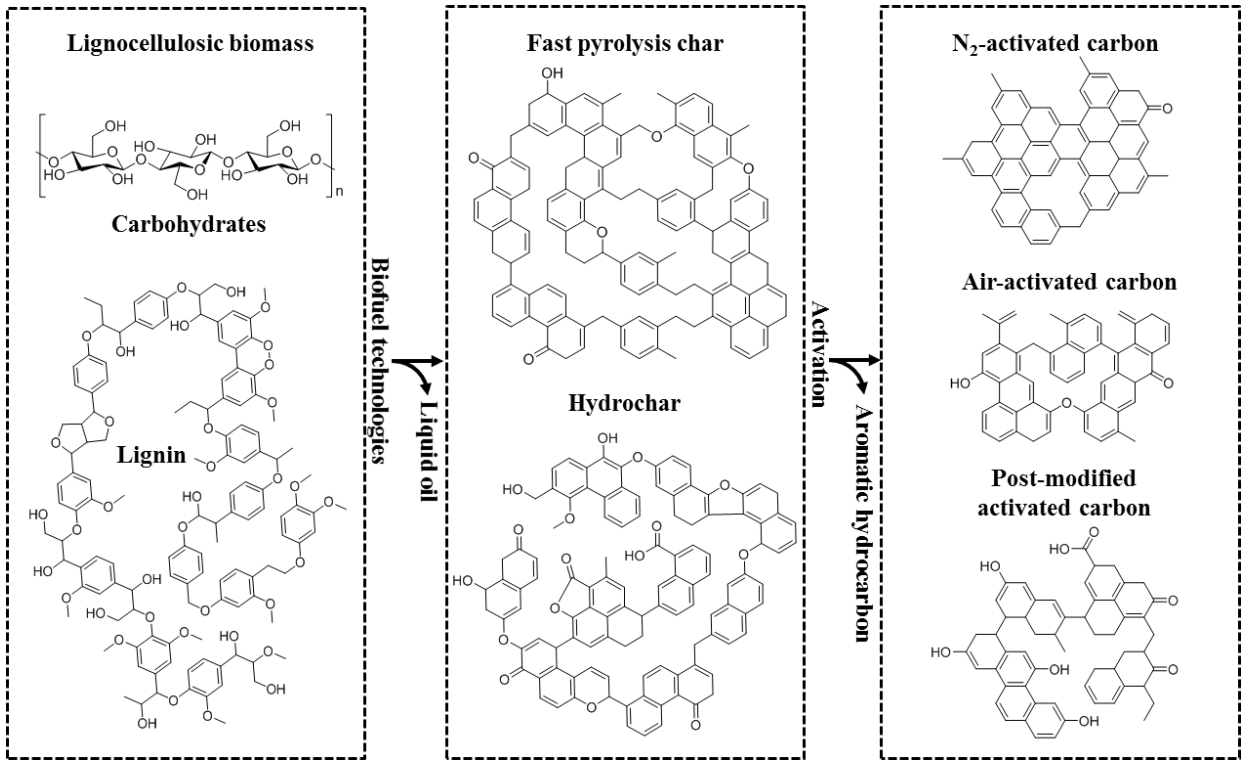

Figure 3-8. Plausible mechanism of structural development of activated carbon product obtained from biomass-derived precursor chars.

3.3.3. Morphological and textural characteristics

The surface morphological features of all carbon samples were observed by SEM analysis (Figure 3-9). The surface of the PC was smooth because it was produced under dry and high reaction temperature conditions compared to those of HC. Meanwhile, a cracked, thin layer with increased surface roughness was observed in activated carbon samples. After post-treatment, the entire surface structure was destroyed along with a collapse of the thin layer.

Changes in specific surface area and pore distribution were analyzed by N_2 adsorption-desorption isotherms. The isotherm curves of carbon products are given in Figure 3-10. According to the International Union of Pure and Applied Chemistry (IUPAC) classification, the activated carbon products are of types Ⅰ and Ⅳ, indicating microporous and mesoporous structures, respectively.

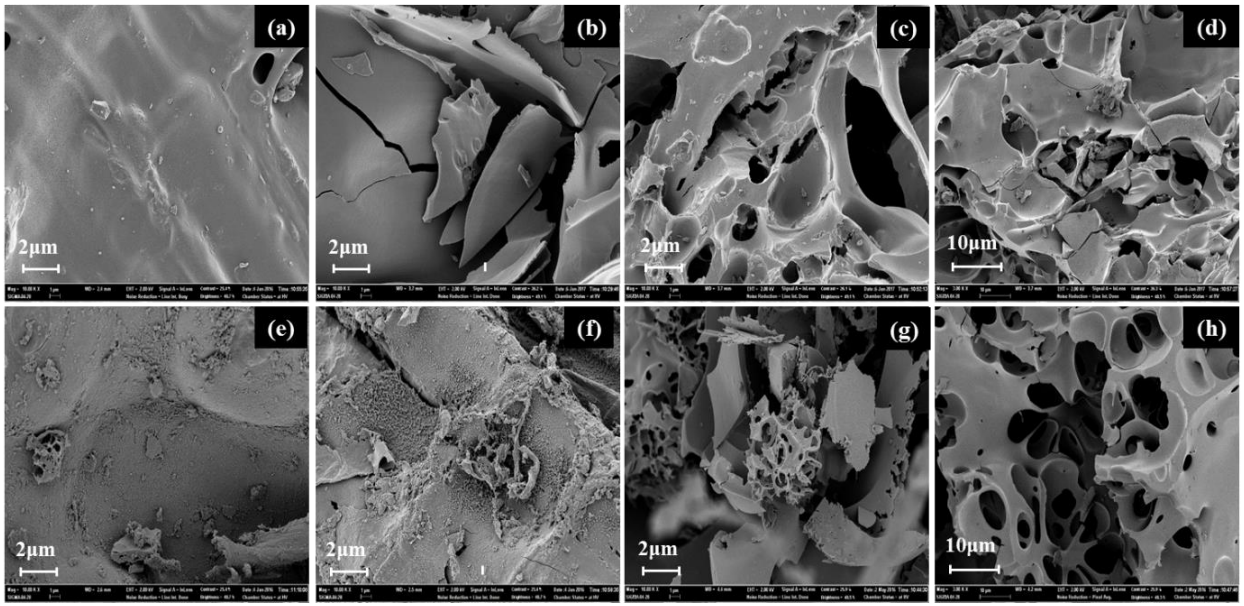

Figure 3-9. The morphological features of carbon samples before and after activation/post-treatment ((a) PC, (b) NPC, (c) APC, (d) NPC-A, (e) HC, (f) NHC, (g) AHC, (h) NHC-A).

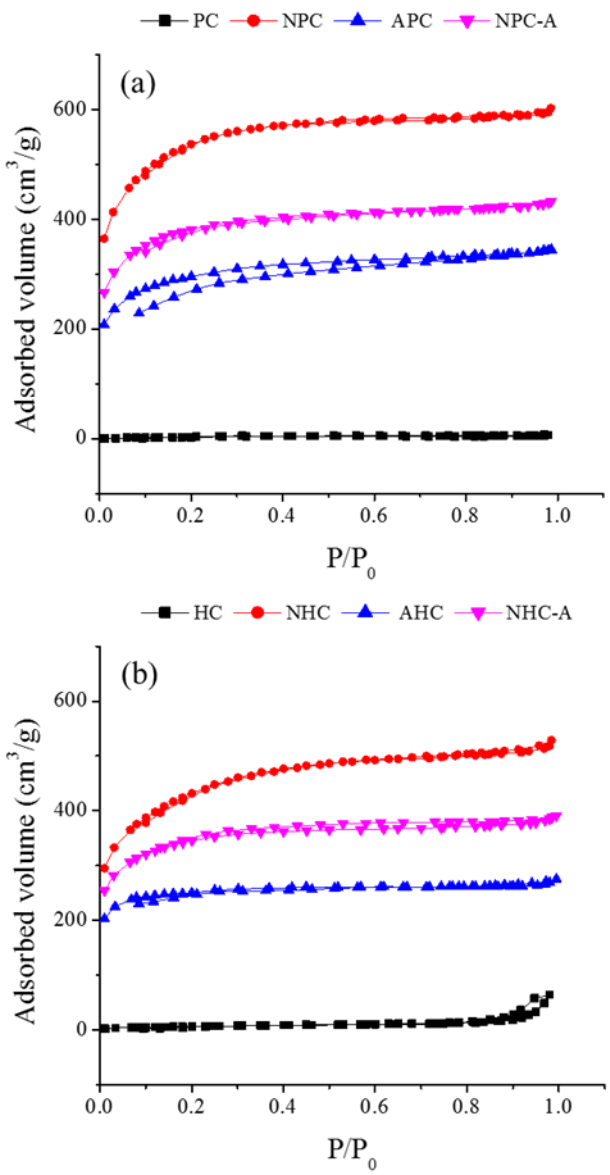

Figure 3-10. N_2 adsorption-desorption isotherm curves for carbon samples before and after activation/post-treatment ((a) carbon products derived from fast pyrolysis char, (b) carbon products derived from hydrochar).

The textural properties and pore size distribution of the carbon products are shown in Table 3-3 and Figure 3-11. As confirmed in Figure 3-10, BET specific surface area of the raw precursor char was low, and the PC had a large amount of meso- or macropores (Figure 3-11). After activation, however, the specific surface area remarkably increased to 1879 m^2/g for NPC and 1515 m^2/g for NHC along with a large increase in total pore volume. Most pores were about 40 Å or less, supra-nanometer size. For APC and AHC, specific surface area and pore volume were lower than in the N_2 activation condition. This can be explained by the increased reactivity of the carbon surface in the presence of oxygen in the air-flow condition due to increased formation of key intermediates in the catalytic reaction. It is generally understood that the main mechanism of KOH activation follows these reactions (3-3) to (3-7) (Lozano-Castello et al., 2007; Otowa et al., 1993; Raymundo-Pinero et al., 2005).

$$2KOH \rightarrow K_2O + H_2O \quad (3\text{-}3)$$

$$C + H_2O \rightarrow CO + H_2 \quad (3\text{-}4)$$

$$CO + H_2O \rightarrow CO_2 + H_2 \quad (3\text{-}5)$$

$$CO_2 + K_2O \rightarrow K_2CO_3 \quad (3\text{-}6)$$

$$K_2CO_3 + 2C \rightarrow 2K + 3CO \quad (3\text{-}7)$$

Among those, metallic K compound has been reported to expand the intercalation structure of carbon lattice (Romanos et al., 2011). Furthermore, it has been suggested that K_2CO_3 would be a key intermediate directly related with carbon destruction by providing a stable supply of melted KOH into pores (Dıaz-Terán et al., 2003; Dıaz-Teran et al., 2001). In the presence of excess oxygen, it is presumed that potassium peroxide is produced from KOH, which reacts with carbon due to its unstable state and forms K_2CO_3. The plausible reaction mechanism is suggested as follows.

$$4KOH + O_2 \rightarrow 2K_2O_2 + 2H_2O \quad (3\text{-}8)$$

$$2K_2O_2 + C \rightarrow K_2CO_3 + K_2O \quad (3\text{-}9)$$

Reaction (3-9) leads to reaction (3-7); thus, the reaction of metallic K

compound with carbon could be further promoted by shortening the reaction step. Consequently, excess air allows the activating agent to penetrate into the carbon structure by increasing the formation of intermediate, resulting in deformation of the carbon product and, in severe cases, structural collapse.

Meanwhile, post-modification by acid treatment also affected the textural properties of the carbon samples. Specific surface area and pore volume were reduced to 1322 m^2/g and 0.91 cm^3/g (NPC-A) and 1191 m^2/g and 0.60 cm^3/g (NHC-A), indicating physical structure collapse as well as chemical changes. As shown in Figure 3-11, the formation of macropores increased after acid treatment, while the distribution of micropores decreased.

Table 3-3. Specific surface area and pore volume of carbon products.

	S_{total}[a] (m^2/g)	$S_{external}$[b] (m^2/g)	V_{total}[c] (cm^3/g)	V_{micro}[d] (cm^3/g)	V_{meso}[e] (cm^3/g)	D_{avg}[f] (Å)
PC	8	6	0.01	-	0.01	67.9
NPC	1879	1045	1.16	0.37	0.79	32.4
APC	1022	485	0.85	0.24	0.61	46.2
NPC-A	1322	618	0.91	0.32	0.59	36.8
HC	23	16	0.14	-	0.14	251.1
NHC	1515	962	1.05	0.25	0.80	33.5
AHC	842	168	0.43	0.31	0.12	29.3
NHC-A	1191	520	0.60	0.31	0.29	22.4

[a] BET specific surface area measured by N_2 adsorption data in the P/P_0 range from 0.06 to 0.20.

[b] External surface area calculated using t-plot method.

[c] Total pore volume determined from the adsorption isotherm at $P/P_0 = 0.99$.

[d] Micropore volume calculated using t-plot method.

[e] Mesopore volume calculated by the difference between V_{total} and V_{micro}.

[f] Average pore diameter determined by the adsorption data using BJH method.

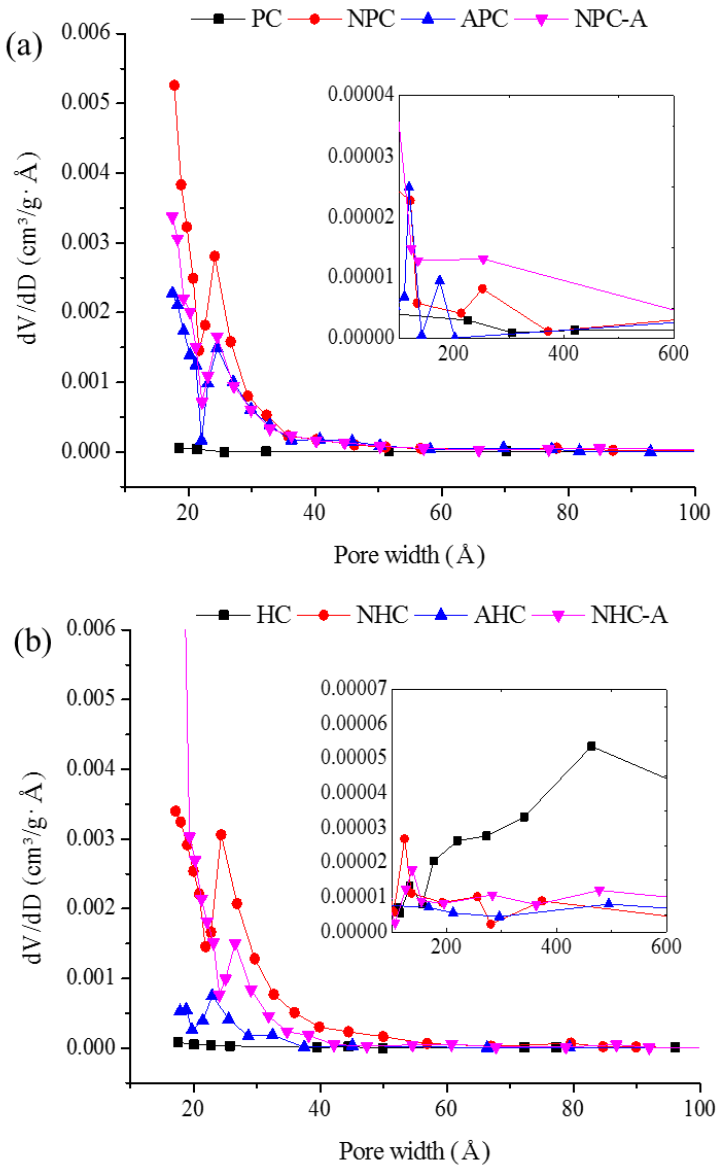

Figure 3-11. Pore size distribution of carbon samples ((a) carbon products derived from fast pyrolysis char, (b) carbon products derived from hydrochar).

3.4. Application in Pb^{2+} removal and as supercapacitor electrode

The Pb^{2+} adsorption efficiency and electrochemical properties of the carbon products derived from different precursors, atmospheric conditions, and post-treatments were evaluated to determine the potential use of these products in industry. The data for this work are shown in Table 3-4.

First, the carbon product was utilized as a biosorbent for water remediation to remove Pb^{2+} in aqueous solution. The precursor char and N_2-activated carbon exhibited a similar adsorption capacity (8.6-19.8 mg/g) to that of commercial activated carbon (15.5 mg/g). This result is consistent with other research wherein the adsorption capacity of pyrolysis char from different wood biomasses was in the range of 2.4-13.1 mg/g (Liu & Zhang, 2009; Mohan et al., 2007).

On the other hand, the capacity of air-activated carbon was as high as 20.3 mg/g (APC) and 41.1 mg/g (AHC), which are comparable to that of the acidified carbon sample using H_2O_2 (22.8 mg/g) or H_3PO_4/HNO_3 (35.5 mg/g) agent, as seen in previous studies (Tao & Xiaoqin, 2008; Xue et al., 2012). This means that the activated carbon produced under air-flow conditions could exhibit a similar efficiency to the heavy metal adsorption capacity of the carbon material treated with additional acidification. This could be attributed to a highly-developed pore structure possessing high oxygen-related bonds and fewer carbon-intensive characteristics than the carbon structure activated only by N_2 gas, as mentioned in Section 3.3.1. and 3.3.3.

After post-treatment, the adsorption efficiency of the carbon products increased to 45.1 mg/g (NPC-A) and 44.2 mg/g (NHC-A) along with an increase in cation exchange capacity as measured by Boehm titration (Boehm, 1994). The large number of functional groups detected in the FT-IR spectra

could lead to high cation exchange capacity, which can strengthen the association between adsorbate and adsorbent.

Next, CV analysis was conducted for both coated-type and coin cell type of electrode by using the carbon products in this study to evaluate their electrochemical properties. An experiment on AHC was not conducted because yields were too low to assemble a sample electrode. The calculated results of the coated-type electrode is provided in Table 3-4. The specific capacitance was calculated in the order of NPC (139.2 F/g) < NHC (159.5 F/g) < APC (185.9 F/g), which is comparable to an advanced carbon material (Burke, 2007) and commercial activated carbon (Jiang et al., 2013; Sevilla & Mokaya, 2014).

Interestingly, APC did not have the highest specific surface area (Table 3-3), but it showed the highest specific capacitance. This indicates that high specific surface area can but does not necessarily have a positive effect on the performance of carbon electrode material. One of the factors that enhances the electrical capacity might be the porous structure of APC with a high mesopore ratio, which could promote the accessibility of electrolyte ions to the inner surface or micropore of the carbon electrode by reducing the diffusion path. Additionally, higher hydrophilicity than N_2-activated carbon, as shown in Section 3.3.1., could be another factor by resulting in the good wetting property of carbon materials in aqueous electrolyte. These factors could attribute to the high conductivity of the carbon electrode.

The post-treated activated carbon has very poor electrochemical properties, as seen in Table 3-4. It was revealed that mild acidification that preserves the intrinsic structure would be helpful to increase electrical capacity by introducing hydrophilic groups, but harsh conditions could produce an adverse effect on the structure (Liu et al., 2012). Therefore, destruction of the surface and pore structure of activated carbon by post-modification, as observed in Section 3.3.3., could result in a low specific capacitance of 10.8 F/g (NPC-A) and 25.0 F/g (NHC-A), which could render the material unsuitable as an

electrode material.

The results of the coin cell type is shown in Figure 3-12. Activated carbon shows a quasi-rectangular shape, implying a near-ideal capacitive behavior (Figure 3-12(a)). Specifically for NHC shows more stable electric performance compared to NPC, which could be attributed that most of inorganic compounds that can be converted to ash were removed during hydrothermal liquefaction process by water solvent. Therefore, ion transport between the pores of NHC-derived electrode could be more facilitated than NPC-derived electrode, which has high ash content. For further understanding of the electric stability of the electrode, cycling life test was performed for 3000 cycles at a current density of 5 mA/cm^2 (Figure 3-12(b)). As a result, good cycling life of the electrode along with 96% of its original capacity was observed. It demonstrates that stable and high performance of electrode can be prepared from co-product of biorefinery through hydrothermal pre-carbonization process.

Table 3-4. Evaluation of Pb^{2+} adsorption and electric properties of coated-type electrode by using carbon products after activation process.

	Pb^{2+} adsorption capacity (mg/g)	Cation exchange capacity (mmol/g)	Specific capacitance (F/g)
PC	11.4	4.8	-
NPC	14.6	7.8	139.2
APC	20.3	5.3	185.9
NPC-A	45.1	13.5	10.8
HC	8.6	-	-
NHC	19.8	8.3	159.5
AHC	41.1	8.9	-
NHC-A	44.2	11.5	25.0

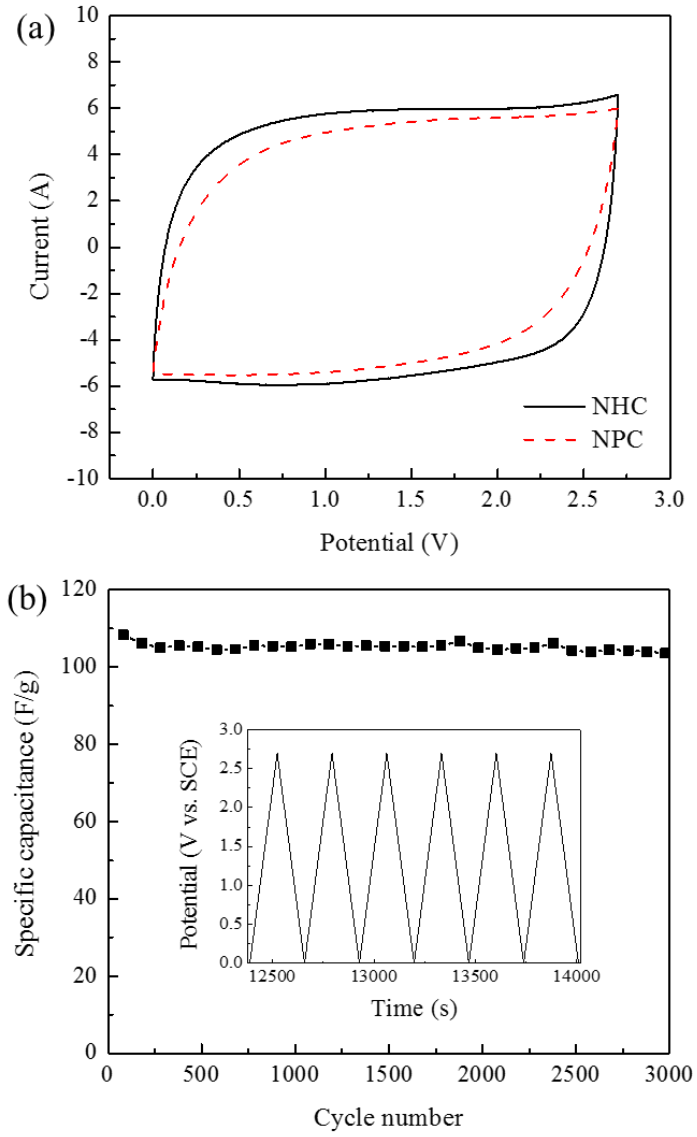

Figure 3-12. Electrochemical performance of the coin cell type electrode fabricated by using NPC and NHC ((a) cyclic voltammetry curves at a scan rate of 10 mV/s, (b) long-term cycling stability of electrode from NHC at 5 mA/cm^2).

4. Conclusions

Preparation and modification of activated carbon derived from different precursor chars under different atmospheric conditions (N_2 and zero air) and by post-acidification (HNO_3) were performed in this study. Additionally, an evaluation of their potentials for application as adsorbent and carbon electrode was carried out. The preliminary tests to investigate the structural degradation mechanism by Py-GC-MS analysis showed that HC has a thermally labile structure to decompose to OA, while PC mainly released AH. After the activation process, activated carbon was produced at a yield of 17.1-48.4 wt.% with a de-functionalized carbon-intensive structure, but post-acidification introduced a large number of functional groups to the surfaces of the carbon products. The specific surface area of raw precursor chars was very low, but it remarkably increased to 1515-1879 m^2/g for N_2-activated carbon and 842-1022 m^2/g for air-activated carbon. It could be presumed that excess air facilitates reactions by which pores are developed by increasing the formation of key intermediates, which can lead to structural collapse. In addition, different characteristics of the prepared carbon products resulted in different performance in various applications. Post-treated carbon products were suitable for Pb^{2+} adsorption because of their large number of functional groups, but these were not available to serve as an electric material due to the destructed surface. Meanwhile, air-activated carbon showed a high capacity for Pb^{2+} adsorption and a specific capacitance of 185.9 F/g due to its high hydrophilic oxygen-related bond content and mesopore ratio, which lead to good wettability and enhancement of accessibility, respectively. The result indicated that simultaneous modification using reactive gas conditions could be a facile method to improve the availability of carbon products compared to a conventional post-treatment.

Chapter 4

Lignin-derived hierarchically porous carbon under various reaction parameters for high-performance adsorbent and supercapacitor

1. Introduction

Lignocellulosic biomass is a renewable energy resource composed of cellulose, hemicellulose, and lignin. Among these materials, lignin typically constitutes 15-35% of lignocellulosic biomass, and it is the most abundant aromatic resource on earth (Azadi et al., 2013). Currently, lignin is generated as a co-product from the pulp industry at a large amount of ca. 70 million tons globally (Liu et al., 2015), and from bioethanol production technologies. Most industrial lignin is burned to generate energy, accounting for 95% of its use (Kleinert & Barth, 2008). However, this can cause some environmental problems related to the emissions of persistent organic pollutants due to incomplete combustion of lignin (Shen et al., 2011). With regard to this application, global interest in a sustainable conversion system to valorize lignin has been intensely investigated. Indeed, lignin has large potential to be converted to functional materials because of its carbon-condensed structure containing aromatics and functional groups. As a result, it is possible to utilize lignin to produce low-cost carbon materials and aromatic compounds (Kai et al., 2016; Xu et al., 2014).

Activated carbon is one of the approaches to utilize the macromolecular form of lignin by employing a thermal conversion process. Activated carbon has several advantages such as high specific surface area and porosity, commercially available processing, high stability, and good thermal and electrical properties. Therefore, it can be utilized in various applications including catalyst (Kastner et al., 2012) support, pollutant adsorbent (Dąbrowski et al., 2005; Lima et al., 2010), and electrode material (Wang & Kaskel, 2012). The commercial global market of activated carbon is estimated to reach 3 million Mtons by 2024, driven by stringent environmental regulations for clean water and air (Global：Industry：Analysts：Inc., 2017). However,

activated carbon is currently largely derived from bituminous coal, which is a fossil fuel. Therefore, if lignin is used for the preparation of activated carbon, it can be a suitable precursor and can replace expensive fossil fuel-based resources, which are not environmentally friendly or economically sustainable.

Since the activation mechanism and properties of the final product are highly dependent on various parameters such as temperature, time, amount of catalyst, and feedstock type, studies regarding their effects have been carried out (Gao et al., 2013; Romanos et al., 2011). It was suggested that an increase in reaction temperature and time resulted in expansion of mesopores and total porosity, indicating that pore characteristic selection is possible by controlling the process conditions. However, the previous studies have focused on pore structure development of activated carbon, but there are also other significant features such as the aromatic structure along with ring enlargement or condensation, thermal cleavage, and the release of chemical molecules that require investigation in order to better understand the catalytic mechanism of activation. In particular, the precise structure of lignin is still unknown, and there is a lack of study regarding its activation mechanism by catalytic reactions. Therefore, it is necessary to study the change of chemical structure of activated carbon derived from lignin as a function of various parameters that might directly affect its performance in further industrial applications.

Recently, several studies have investigated lignin activation (Carrott & Carrott, 2009; Fu et al., 2013) and further utilization for biosorbent or supercapacitor electrode (Gao et al., 2013; Hu & Hsieh, 2017; Saha et al., 2014). Gao et al. used black liquor lignin to prepare activated carbon for nickel ion adsorption, and revealed that its adsorption capacity was enhanced above pH 5 due to electrostatic attraction. Carbon electrodes fabricated using KOH-activated carbon derived from alkali lignin and kraft lignin showed high specific capacitances of 149 and 92 F/g, respectively. The results suggest that several factors such as specific surface area and oxygen-containing groups affect

capacitance performance. However, controversy remains, and estimation of the contributions of each factor is required.

In our previous study, fast pyrolysis char, another co-product of biofuel technologies, was employed to prepare activated carbon for phenol adsorption (Hwang et al., 2017). As a result, highly activated carbon with a specific surface area of 2711 m^2/g was successfully produced and exhibited excellent adsorption capacity, which demonstrates that it has good potential to be applied as a biosorbent. As a high-value application of solid co-products obtained from a biorefinery process, this study focused on the development of high performance carbon material using lignin under various parameters. Two kinds of lignin samples were used as precursors where the reaction temperatures , times, and catalyst loadings were adjusted in the range of 700-800°C, 0.5 h-2 h, and 0-1:6 (w:w = lignin:catalyst) respectively, to evaluate the chemical and porous structural changes obtained under different reaction conditions. The process was streamlined by one-step activation, and the obtained activated carbon was typically characterized in terms of its surface functionalities based on morphological and porous analyses. In addition, the detailed thermal decomposition mechanism was investigated using powerful tools including pyrolysis-gas chromatography-mass spectrometry (Py-GC-MS) and Raman spectroscopy to monitor the released volatiles and carbon crystalline structure. Finally, lignin-derived activated carbon was employed as a biosorbent and carbon electrode material to investigate its potential use in industrial fields. The objective of this study was to advance the valorization of lignin for use in low-cost and renewable activated carbon electrodes as well as to conduct a comprehensive study of the relationships between the reaction parameters and properties of the products.

2. Materials and methods

2.1. Preparation and characterization of lignin samples

Two kinds of lignins, Asian lignin (AL) and Inbicon lignin (IL), were utilized for production of activated carbon. AL was purchased from GreenValue Enterprises LLC (USA) and was treated with NaOH under sulfur-free conditions. IL was kindly provided by DONG Energy (Denmark) in pellet form and was produced from hydrothermal treatment. The lignin sample was ground to a 2 mm powder size by a cutting mill (PULVERISETTE 19, Germany).

The elemental compositions (C, H, N, and S) of the lignins were analyzed using a US/CHNS-932 (LECO, USA) to calculate the elemental ratios where the amount of oxygen was calculated based on the difference. Because the two lignins were isolated from different processes, the lignin content excluding other constituents or impurities was determined using the TAPPI method (T222 om-88). Thermogravimetric analysis (TGA) was conducted in the temperature range of 40°C to 700°C under inert N_2 conditions using a TGA/DSC 3+(LF-1100) (Mettler-Toledo AG, Switzerland). Table 4-1 shows the fundamental analysis data of the raw lignin samples.

Table 4-1. Fundamental and thermogravimetric analysis of raw lignin samples.

	Lignin (wt.%)	Elemental analysis (%)					Thermogravimetric analysis		
		C	H	S	N	O*	Volatiles (wt.%)	Residue (wt.%)	Temperature at max. rate (°C)
AL	94.9	61.7	5.9	1.0	0.6	30.8	66.1	33.9	362
IL	63.3	48.5	5.6	0.2	0.7	45.0	74.2	25.8	318

* by difference.

.

2.2. Chemical activation by varying reaction parameters

In order to prepare lignin-derived activated carbon, 5 g of lignin was added to a batch reactor (100 ml) with KOH (4:1, weight based on the lignin sample), and the mixture was homogeneously mixed. The reactor was sealed and kept under inert conditions with a N_2 gas flow rate of 300 ml/min for 10 min. At the desired reaction temperature, the reactor was then placed in a heated furnace and the reaction was allowed to proceed for the set time. In this study, the process parameters varied were with temperature (700, 750, and 800°C), reaction time (0.5, 1, and 2 h), and catalyst loading (0, 1:1, 1:2, 1:4, and 1:6 (w:w = lignin:catalyst). The other process conditions were fixed at 750°C, for 1 hour, and catalyst ratio of 1:4 respectively. After the process, the reactor was taken out, cooled to room temperature, and the mixture inside was collected. The carbon product was neutralized and washed with 250 ml of HCl (1 M) and 1 L of D.I. water under vacuum filtration, followed by drying in an oven at 105°C overnight. The activated carbon product (AC) is referred to as ALAC or ILAC depending on the type of raw lignin and is named according to the process parameters, such as AL-700°C, AL-750°C, AL-0.5h, AL-1h, AL-Cat.1, AL-Cat.2, and AL-Cat.4, etc..

2.3. Characterization of lignin-derived activated carbon

Elemental analysis was carried out using the same method employed for lignin. The surface chemical characteristics of activated carbon were analyzed by Fourier transform infrared spectroscopy (FT-IR; Nicolet 6700, Thermo Scientific, USA) equipped with attenuated total reflectance (ATR) over the range from 600 to 4,000 cm^{-1} with a resolution of 8 cm^{-1} and 32 scans. X-ray photoelectron spectroscopy (XPS) was conducted using an AXIS-HSi

(KRATOS, UK) instrument. The binding energies of the C1s photoelectron shifted with peak deconvolution at 284.5 eV. Changes in structural degradation were investigated by Py-GC-MS analysis and Raman spectroscopy. The volatiles released from the catalytic thermal decomposition of lignin were identified and quantified by Py-GC-MS equipped with a coil-type CDS Pyroprobe 5000 (CDS Analytical Inc., Oxford, PA, USA) and GC–MS/FID (Agilent Technologies 7890A/Agilent Technologies 5975A, USA) with a DB-5 capillary column (30 m × 0.25 mm ID × 0.25 μm film thickness). The mixture of lignin and KOH was simultaneously pyrolyzed in a quartz tube at reaction temperatures of 700, 750, and 800°C, and the organic volatiles were monitored. The detailed injector and oven settings as well as a quantitative equation have been described in a previous study (Hwang et al., 2017). Raman spectra were obtained in the range of 1,000-1,800 cm^{-1} using LabRAM HV Evolution (HORIBA Scientific, Japan) installed at the National Center for Inter-university Research Facilities (NCIRF) at Seoul National University. The morphology of activated carbon was observed by field-emission scanning electron microscopy (FESEM) using a SIGMA (Carl Zeiss, UK) at the National Instrumentation Center for Environmental Management (NICEM). For pore characterization, N_2 adsorption-desorption isotherm analysis was carried out at 77 K using an ASAP 2010 (Micrometrics, Canada) instrument. The Brunauer-Emmett-Teller (BET) surface area was determined using the N_2 isotherm, where the Barrett-Joyner-Halenda (BJH) method was used to determine the pore size and average diameter using the adsorption branch. To evaluate the micropore structure, the t-plot method was used.

2.4. Utilization as an adsorbent for removal of heavy metal and organic pollutants

For evaluating a heavy metal and organic pollutants removal ability of the produced activated carbon, a batch adsorption test for lead, cadmium, phenol, bisphenol-A (BPA), and 2,4-dichlorophenoxyacetic acid (2,4-D) were performed. Chemical structure of each organic pollutants was provided in Table 4-2. $Pb(NO_3)_2$, $Cd(NO_3)_2$, and other organic pollutants were purchased from Sigma-Aldrich and used for preparing of standard solution. The carbon product was added with a fixed dose of 1 g/L to each pollutant solution (100 ppm) and agitated for 12 h at 28°C. After the adsorption, the filtrate was recovered and calculated the adsorbed amount from the initial concentration. Concentrations of heavy metals were analyzed by inductively coupled plasma-emission spectroscopy (ICP-ES) using iCAP 7400 (Thermo Scientific, USA) and those of organic pollutants were determined by high-performance liquid chromatography (HPLC) using Ultimate 3000 (Thermo Scientific, USA). The mixture of acetonitrile and D.I. water was used as a mobile phase for the analysis, and UV wavelength of phenol, BPA, and 2,4-D was 260. 228, and 280 nm, respectively. For a comparison, commercial activated carbon (CAC; Sigma-Aldrich) was subjected to the same experiment procedures.

Table 4-2. Chemical structure of organic pollutants.

Pollutant	Phenol	Bisphenol-A (BPA)	2,4-Dichlorophenoxyacetic acid (2,4-D)
Chemical structure	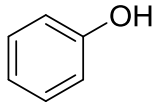	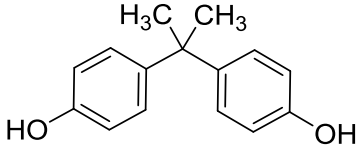	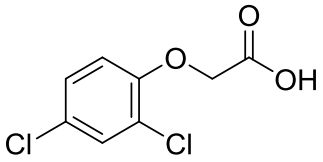

2.5. Fabrication of carbon electrode

In order to utilization of lignin-derived activated carbon, carbon electrode for supercapacitor was fabricated and tested. The ground activated carbon samples were mixed with polytetrafluoroethylene (PTFE, binder) and carbon black (conducting material) at a ratio of 85:10:5 (w/w). Then, 400 μl of ethanol was added to make an electrode slurry that was then sonicated for 2 h to result in better mixing. After the slurry was pasted onto Ni foam, which was used as the current collector, it was dried in an oven overnight. Then, it was pressed at 10 MPa for 1 min to prepare the final electrode sample. The mass loading of the sample was about 10 mg/cm^2. The electrochemical characteristics were evaluated using a three-electrode system and a 6 M KOH aqueous solution as the electrolyte. The prepared electrode sample served as the working electrode, and Pt wire and Ag/AgCl were used as the counter and reference electrode, respectively. Cyclic voltammetry (CV) and electrochemical impedance spectroscopy (EIS) were employed using a VersaSTAT4-200 (Princeton Applied Research, USA) electrochemical workstation. The voltage range for the CV analysis varied from -1.0 to 0 V with a scan rate of 10 mV/s. The gravimetric specific capacitance was calculated using equation (4-1).

$$\text{Specific capacitance (F/g)} = \frac{\int iv\,dv}{2\mu m\Delta V} \quad (4\text{-}1)$$

where i is the current, v is the potential in the CV test (total area of the curve), μ is the scan rate (V/s), m is the mass of the carbon sample (g), and ΔV is the width of the potential window (V). The EIS was determined at frequencies ranging from 10 mHz to 0.1 MHz with an amplitude of 5 mV. In addition, coin cell type electrode was also fabricated by a modified method as described in a previous study (Han et al., 2017). All experiments were carried out in duplicate, and the average values are presented.

3. Results and Discussion

3.1. Manufacturing of lignin-derived activated carbon

Table 4-3 shows the yield and elemental composition of activated carbon obtained from the two lignins under different conditions. The yield of activated carbon was higher with a yield of 9.2-43.8 wt.% when AL was used compared to IL (4.3-36.2 wt.%). This could be explained by the results shown in Table 4-1, where AL has relatively higher lignin content, residual amount, and a maximum degraded temperature, which results in higher thermal stability during the thermal decomposition process. As the reaction time increased, the yields of both samples gradually decreased due to a further cracking reaction. The high catalyst ratios were also significantly lower in the yield of activated carbon due to the excessive reaction that could destroy the carbon rigid structure.

The carbon content of the products was in the range of 65.2-86.3 % except for IL-Cat.1 (60.9 %) and IL-0.5h (51.8 %). Carbon on the surface can react with the catalyst and results in structural development (Lozano-Castello et al., 2007), but the carbon content of IL was relatively lower than that of AL. Therefore, IL requires more reaction time for sufficient catalytic conversion. Thus, there was little difference between activated carbon obtained from IL in 0.5 h or with catalyst ratio of 1 and raw lignin (48.5 %). As the catalyst ratio increased to 4, the carbon content increased, but when it reached 6, it decreased while the oxygen content increased. This indicates that graphitization and aromatization proceeded by proper catalyst ratios, but carbon loss occurred with excessive catalytic amounts. In addition, the hydrogen and oxygen contents (5.6-5.9 % and 30.8-45.0 %, respectively) of the raw lignin samples sharply decreased after the activation process, indicating that dehydrogenation and deoxygenation occurred.

Table 4-3. Yield of activated carbon from lignin samples under different reaction parameters.

Sample	Temp. (°C)	Time (hour)	Catalyst ratio	Yield (wt.%)	Elemental composition (%)				
					C	H	N	S	O*
ALAC	700	2	4	26.3	82.3	0.1	0.0	0.2	17.4
	750	2	4	19.4	80.6	0.0	0.0	0.3	19.1
	800	2	4	20.2	86.3	0.0	0.0	0.2	13.5
	750	0.5	4	24.9	79.9	0.0	0.0	0.7	19.5
	750	1	4	21.4	85.1	0.0	0.0	0.8	14.1
	750	1	0	32.1	73.4	0.4	0.0	1.4	24.8
	750	1	1	43.8	74.7	0.1	0.0	0.8	24.4
	750	1	2	32.9	83.9	0.0	0.0	1.2	14.9
	750	1	6	9.2	77.1	0.0	0.0	1.1	21.8
ILAC	700	2	4	8.6	75.5	0.0	0.0	0.3	24.2
	750	2	4	7.4	78.0	0	0	0.6	21.4
	800	2	4	7.2	85.7	0	0	0.3	14.0
	750	0.5	4	17.7	51.8	1.4	0.0	0.6	46.2
	750	1	4	12.0	74.9	0.0	0.0	0.7	24.4
	750	1	0	38.6	65.2	0.4	0.0	0.7	33.7
	750	1	1	36.2	60.9	0.4	0.0	0.8	37.9
	750	1	2	27.9	70.9	0.3	0.0	0.8	28.0
	750	1	6	4.3	68.8	0.5	0.0	0.7	30.0

* by difference.

3.2. Surface functionalities after chemical activation process

FT-IR and XPS analyses were performed to observe the surface functionalities of the produced activated carbon. Figure 4-1 shows the FT-IR spectra of lignin-derived activated carbon according to reaction temperature and time.

The raw lignin samples (AL and IL) have a large number of functional groups on their surface, and the main peaks can be identified as C-O stretching or the phenyl alkyl ether group (1035 cm^{-1} and 1265 cm^{-1}), secondary alcohol (1118 cm^{-1}), tertiary alcohol or phenol (1215 cm^{-1}), CH_x- aliphatic chains or C-O-H (1460 cm^{-1}), conjugated aromatic ring vibration or stretching C=C (1600 cm^{-1}), conjugated aromatic carbonyl or carboxyl C=O (1700 cm^{-1}), CH_x- asymmetric stretching vibration (2940 cm^{-1} and), and –OH stretching vibration (3400 cm^{-1}) (Gomez-Serrano et al., 1996; Lin et al., 2014; Pavia et al., 2008).

After the activation process above a temperature of 700°C, the peaks at 1050, 1380, 1600, 2900, and 2985 cm^{-1} representing for phenyl alkyl ether, aliphatic chains, conjugated aromatic ring vibration, and aliphatic carbon asymmetric stretching vibration, respectively, decreased but remained. For the spectra of IL-0.5h, a small peak corresponding to the -OH stretching band derived from the raw sample was still observed; after reaction for 1 h, it diminished along with other functional group peaks.

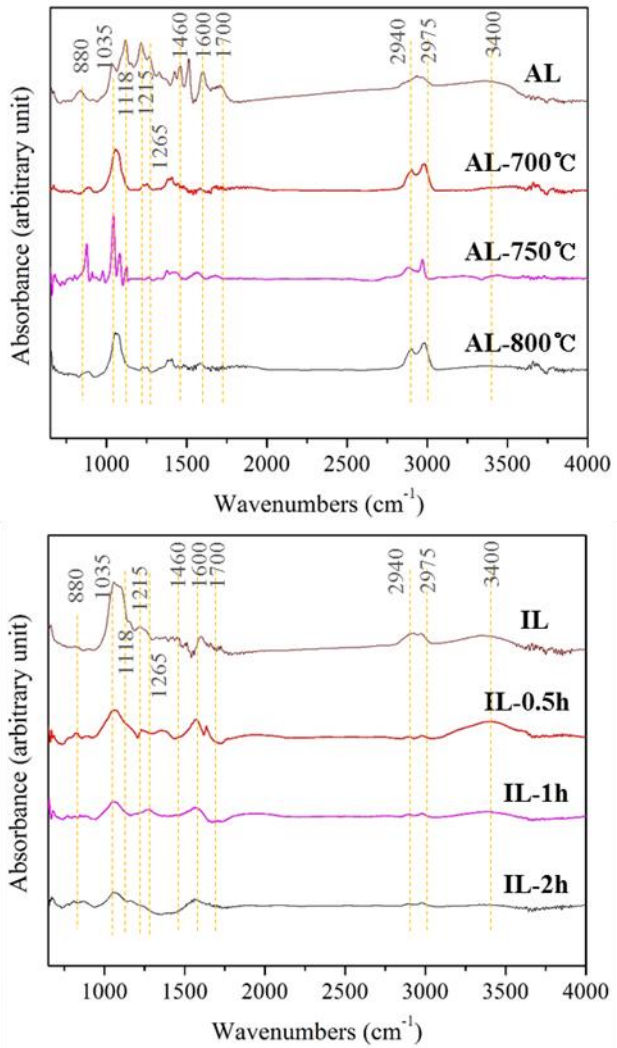

Figure 4-1. FT-IR spectra of raw lignin and lignin-derived activated carbon under different reaction temperatures and times.

Table 4-4 shows the surface chemical composition of the lignin and carbon products. The XPS curve was fitted by shifting the main C1s(1) peak at 284.5 eV, and four deconvoluted peaks were obtained. The largest peak of C1s(1) represents C-C/C=C groups (284.5 eV) and the other peaks of C1s(2), C1s(3), and C1s(4) correspond to C-O (286.0 eV), C=O (286.6 eV), and O=C-O (288.9 eV), respectively. The relevant contents of the C1s(1) peak of AL and IL were 70.9 % and 44.0 %; however after the activation process, the amounts increased, whereas the other oxygen-related binding contents decreased. Because of the thermal instability of carbon-oxygen bonding, oxygen can be easily eliminated to form –C free radicals, which can then be converted to a stable C=C structure form by polycyclization. Concerning the reaction time, the intensity of the C1s(1) peak of the products obtained with a reaction time of 0.5 h was relatively low while that of the oxygen-related peak was high. This could be due to formation of an alkali oxide-carbon complex. Therefore, this result indicates that the catalytic reaction could begin from the external surface. Further reactions were observed from the products obtained under harsh process conditions. In particular, the C1s(1) intensity was highest for the activated carbon produced at 800°C. This could be attributed to alkali metal on the external basal plane, which gradually penetrated and dispersed into the internal space, and then reacted with the carbon lattice, resulting in a carbonized surface (McKee, 1982). In addition, the intensity of C1s(1) for carbon product produced without the catalyst was higher than that of the catalytic activated carbon, which could be attributed that only the carbonization occurred by high temperature condition. As catalyst ratio increased, a similar tendency of elemental composition was observed that the carbon related peaks were similar or increased until the catalyst ratio of 4, but it decreased when the catalyst ratio was 6.

Table 4-4. Relative chemical composition of activated carbon by deconvoluted XPS curves.

Sample	Temp. (°C)	Time (hour)	Catalyst ratio	Chemical binding compositon (%)			
				sp^2-graphitic or C-C, C-H (C1s(1))	C-O (C1s(2))	C=O (C1s(3))	O=C-O (C1s(4))
AL	-	-	-	70.9	10.5	17.0	1.5
	700	2	4	85.3	8.5	6.2	-
	750	2	4	81.3	8.7	10.0	-
	800	2	4	88.1	6.0	5.9	-
	750	0.5	4	74.8	19.3	5.9	-
ALAC	750	1	4	84.3	7.4	8.3	-
	750	1	0	83.2	16.8	-	-
	750	1	1	77.8	20.7	1.5	-
	750	1	2	79.4	12.1	8.6	-
	750	1	6	82.1	8.7	9.2	-
IL	-	-	-	44.0	16.0	22.5	17.4
	700	2	4	78.2	9.5	6.4	5.9
	750	2	4	80.6	8.1	9.1	2.3
	800	2	4	85.0	4.0	11.0	-
	750	0.5	4	75.2	7.7	12.0	5.1
ILAC	750	1	4	84.1	5.9	5.7	4.4
	750	1	0	92.6	5.3	2.1	-
	750	1	1	84.6	7.1	8.3	-
	750	1	2	86.8	10.0	3.2	-
	750	1	6	81.0	19.0	-	-

3.3. Changes in structural features

In order to investigate the structural features during and after the activation process, DTG analysis, Py-GC-MS analysis and Raman spectroscopy were performed in this study.

First, simultaneous thermal decomposition behavior of lignin was observed by DTG analysis with or without catalyst (Figure 4-2). The weight loss for raw lignin samples began above 300°C, but it significantly lowered around the range of 150-270°C in the presence of catalyst. As the catalyst ratio increased, the amount of weight loss increased and the decomposition temperature range widened. The bonding structure such as benzyl alkyl, aryl ether, and C-C including β-β can be cleaved by those temperature ranges (Brebu & Vasile, 2010), thus KOH could change the thermal stability of lignin and facilitate structure degradation at low temperature.

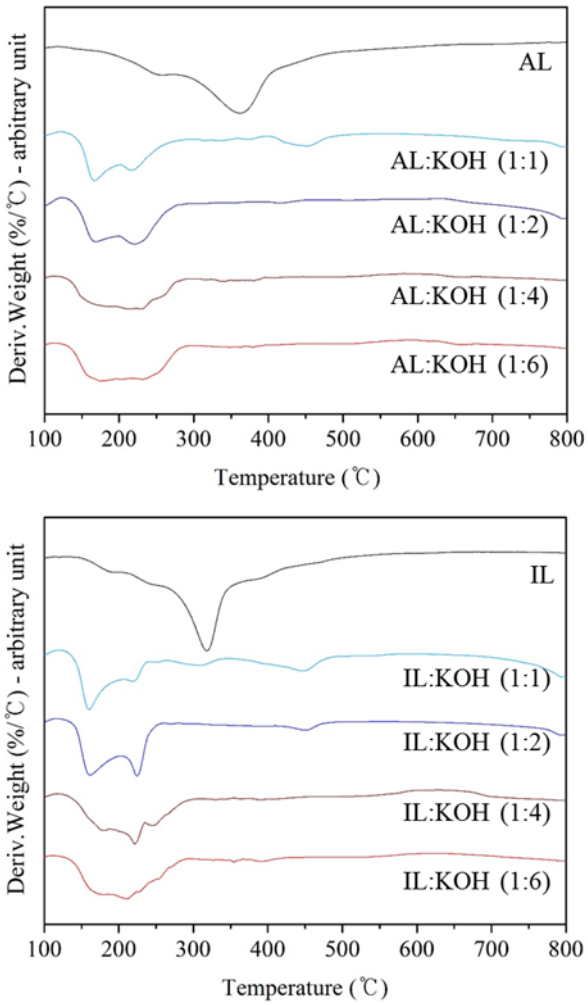

Figure 4-2. DTG curves of raw lignin and lignin with different catalyst ratios.

In addition, the volatile compounds released from the raw lignin samples during catalytic thermal decomposition as a function of reaction temperature were qualified and quantified as shown in Figure 4-3 and Table 4-5. The main volatiles were 5 kinds of aromatic hydrocarbons (AH) and 3 kinds of polyaromatic hydrocarbons (PAH), which were deoxygenated compounds. The total amounts of the released compounds were 12.04-18.88 mg/g for AL and 7.09-10.92 mg/g for IL. Considering the TGA results of the residual amount (Table 4-1) and the yield after the activation process (Table 4-3), the lower volatile amount of IL could be attributed to the conversion of CO and CO_2 by gasification of intermediate volatiles. For raw lignin without catalyst, significant amounts of oxygenated volatile compounds such as phenol, cresol, 4-vinyl phenol, 2-allyl phenol, and vinyl guaiacol were also released as well as aromatic hydrocarbons. In the presence of catalyst, only AH and PAH were detected and the relative proportions of AH increased with an increase in catalyst ratio. This indicates that deoxygenation and demethylation could be promoted during catalytic activation, followed by the conversion of volatiles into light compounds. As the temperature increased, the relative proportions of benzene and naphthalene increased whereas the amounts of toluene, ethylbenzene, and xylene decreased. This indicates that a side chain cleavage reaction including dealkylation and demethylation was promoted at high temperature, particularly above 750°C.

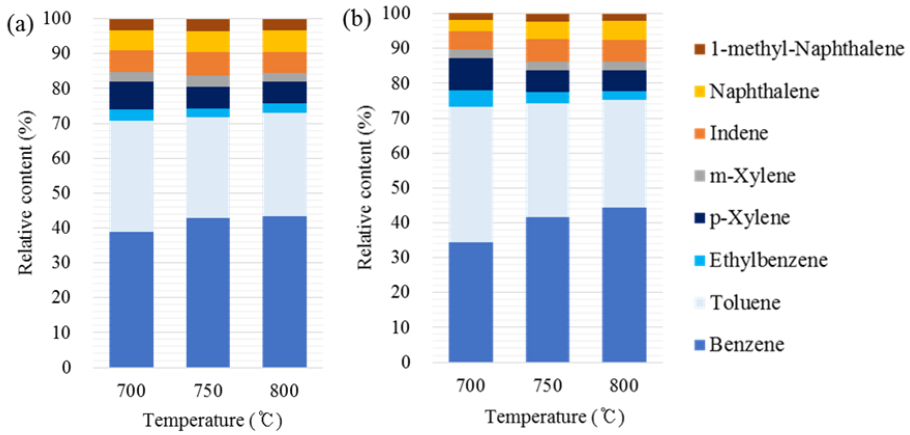

Figure 4-3. Volatile compounds released from lignin during catalytic thermal conversion process under different reaction temperatures ((a) AL (b) IL).

Table 4-5. Volatile compounds released from lignin during catalytic thermal conversion process under different catalyst ratios.

Type	Compound	AL:KOH					IL:KOH				
		No catalyst	1:1	1:2	1:4	1:6	No catalyst	1:1	1:2	1:4	1:6
AH[a]	Benzene	8.22	7.54	6.57	5.16	6.24	5.38	3.44	2.66	3.60	2.69
AH	Toluene	5.03	5.07	4.46	3.48	4.12	3.11	3.51	3.74	2.82	2.55
AH	Ethylbenzene	0.33	0.46	0.43	0.29	0.27	0.42	0.50	0.53	0.27	0.37
AH	p-Xylene	0.90	0.94	0.92	0.75	0.58	0.42	0.79	0.91	0.55	0.45
AH	m-Xylene	0.34	0.31	0.25	0.39	0.28	0.13	0.26	0.31	0.21	0.24
	Total AH	14.83	14.31	12.62	10.08	11.48	9.46	8.50	8.16	7.45	6.30
PAH[b]	Indene	1.57	1.06	0.96	0.82	0.98	0.59	0.55	0.37	0.55	0.42
PAH	Naphthalene	1.75	1.42	1.09	0.71	0.77	0.67	0.55	0.38	0.42	0.22
PAH	1-methyl-Naphthalene	0.74	0.58	0.64	0.42	0.37	0.20	0.45	0.26	0.21	0.16
	Total PAH	4.06	3.05	2.68	1.95	2.11	1.47	1.56	1.01	1.19	0.79
	Total	18.88	17.36	15.30	12.04	13.59	10.92	10.05	9.17	8.64	7.09

* Unit : mg/g lignin

[a] AH: Aromatic hydrocarbon

[b] PAH: Polycyclic aromatic hydrocarbon

The Raman curves of each activated carbon product were also obtained and fitted by 5 Gaussian bands to better understand the typical structural features. The deconvoluted bands represent the condensed benzene region, C-C between aromatic rings, and aromatics with not less than 6 rings (D peak at 1320 cm^{-1}), semi-circle breathing of the aromatic rings and methyl groups in amorphous carbon structures (V_R peak at 1380 cm^{-1}), semi-circle breathing of aromatic rings and methylene groups in amorphous carbon structures (V_L peak at 1465 cm^{-1}), aromatics with 3-5 rings and amorphous structures (G_R peak at 1540 cm^{-1}), and graphite, aromatic ring quadrant breathing, and alkene C=C bonds (G peak at 1580 cm^{-1}) (Lin-Vien et al., 1991; Tuinstra & Koenig, 1970; Wang et al., 1990).

The product obtained at 750°C showed the highest D/G ratio, indicating that a turbostratic disorder structure possessing a large aromatic ring system (more than 6 rings) with a small particle size was developed. As the temperature increased to 800°C, both the D/G ratio and $D/(G_R+V_R+V_L)$ ratio decreased for ALAC. Since the $(G_R+V_R+V_L)$ ratio corresponds to a small aromatic ring system and the aromatic ring breathing mode in an amorphous structure, the result could be explained by an increase in graphitization region with remaining or new small aromatic rings.

A low $D/(G_R+V_R+V_L)$ ratio were observed for both products obtained from AL and IL with a reaction time of 0.5 h. This could be due to incomplete polymerization of aromatic rings and less graphitization. For longer reaction times, an increase in graphite content or continual enlargement of the aromatic ring was observed in ALAC while conversion of the small to large aromatic ring system and a stacking disorder structure occurred in ILAC. This difference between the two samples could have resulted from the initial structures, as shown in Table 1. AL has a higher lignin content associated with the aromatic ring content and thermal stability, such that further ring condensation that decreases C-C between aromatic rings at the D peak could be promoted for a

prolonged reaction time. On the other hand, IL has a lower lignin content and, thus might require relatively more time to form a large aromatic ring system by transition from the small ring structure.

Catalyst ratio also affected the structural characteristics of activated carbon. At the catalyst ratio of 2, the highest ratio of $D/(G_R+V_R+V_L)$ was observed which implies that discontinuity of carbon lattice increased by breaking of symmetry crystalline structure, resulting in stacking disorder. The disordered structure still maintained at the catalyst ratio of 4, but ring condensation might occurr as shown in a decrease of $D/(G_R+V_R+V_L)$ ratio. With an addition of large amount of catalyst, both peak ratios decreased, implying that loss of defective region by destruction.

Based on the above analysis, the plausible structural degradation mechanism of lignin during catalytic activation process is shown in Figure 4-5 and Figure 4-6. As the reaction time increased, aromatic ring structure of lignin could be gradually enlarged and condensed with a release of aromatic hydrocarbon volatiles. As for Figure 4-6, decomposition and rearrangement of lignin structure at low catalyst loadings is similar to that described above, but as the catalyst amount increased, the disorderness of carbon lattice could be further enhanced and then it destroyed at high catalyst ratio.

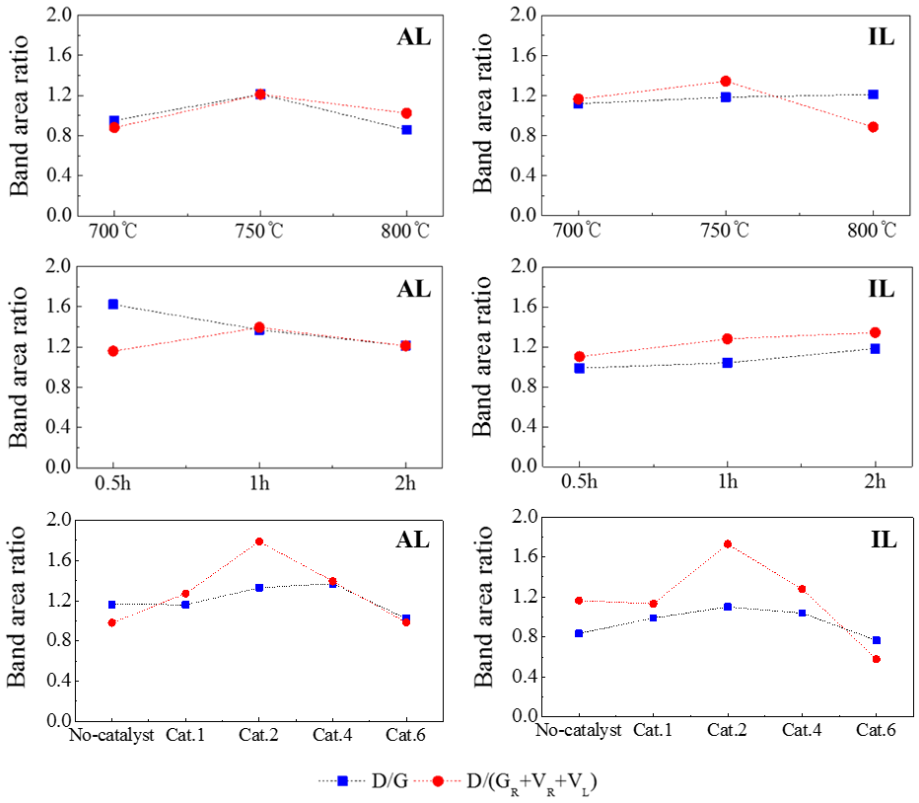

Figure 4-4. Raman peak ratio of activated carbon under different reaction parameters.

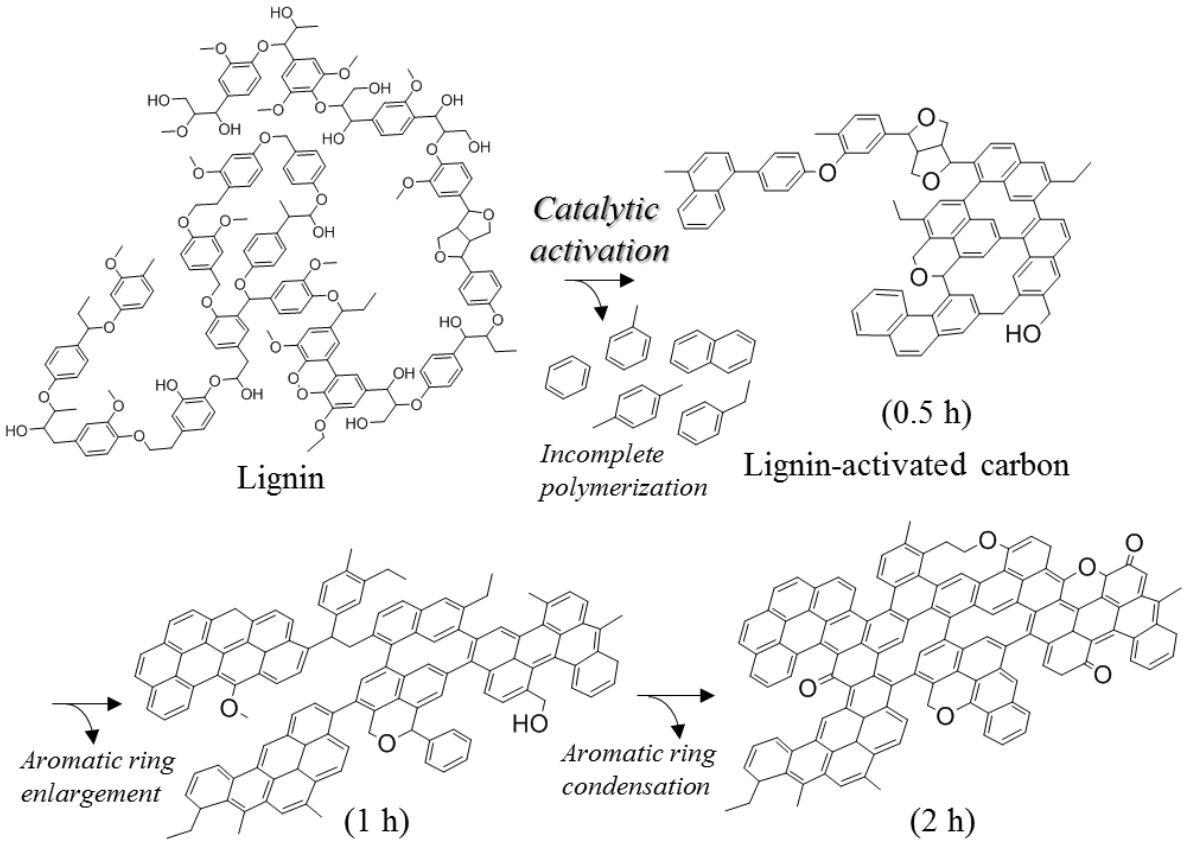

Figure 4-5. Structural development mechanism of lignin-derived activated carbon as a function of reaction times.

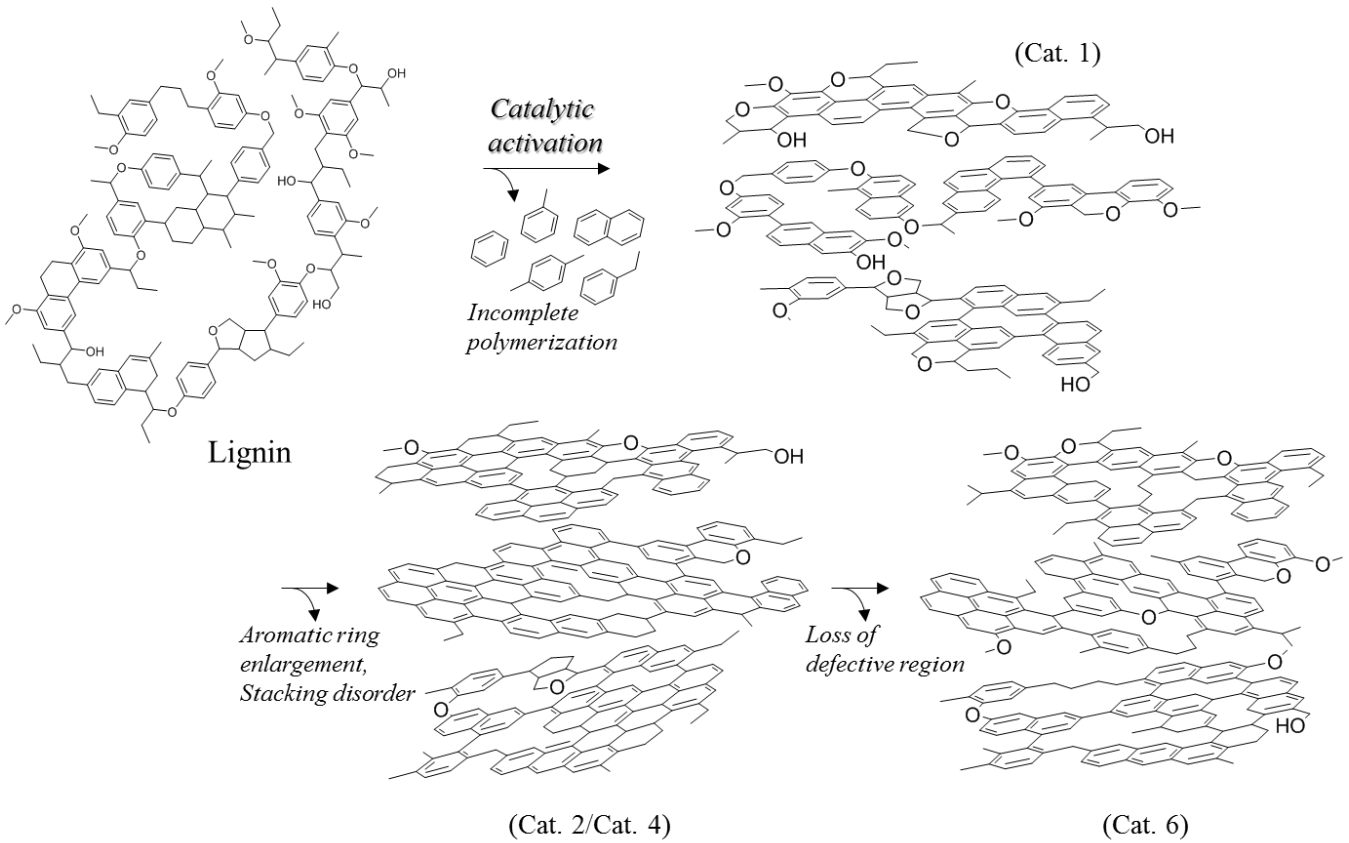

Figure 4-6. Structural development mechanism of lignin-derived activated carbon as a function of catalyst loadings.

3.4. Morphological and textural properties

The surface morphologies of the raw lignins and the activated carbon produced were observed by SEM analysis. Figure 4-7 shows the SEM images of each sample obtained under different process conditions. The raw lignin (Figure 4-7(a)) was in the shape of a cluster, but it was fragmented and cracked with the creation of pores on the surface after the activation process (Figure 4-7(b)-(d)). At a reaction temperature of 800°C (Figure 4-7(d)), surface erosion can be observed due to the harsh conditions. For a reaction time of 0.5 h, it is shown that a relatively thick wall possessing pores exists in IL-0.5h (Figure 4-7(e)). As the reaction time was increased, the layer became thinner and pores were created on the internal layer, which can provide more reactive sites to other substances. In addition, the carbon surface of IL-2h (Figure 4-7(g)) shows structural collapse with rough edges. In addition, as shown in Figure 4-7(i), surface cannot be developed without catalyst in spite of high reaction temperature condition of 750°C. However, a small amount of catalyst significantly changed the surface morphology to porosity (Figure 4-7(j)) and surface layer became thinner until the catalyst ratio of 4. At the catalyst ratio of 6, as similar tendency as other properties, pores in thin layer was less observed due to loss of weak external regions.

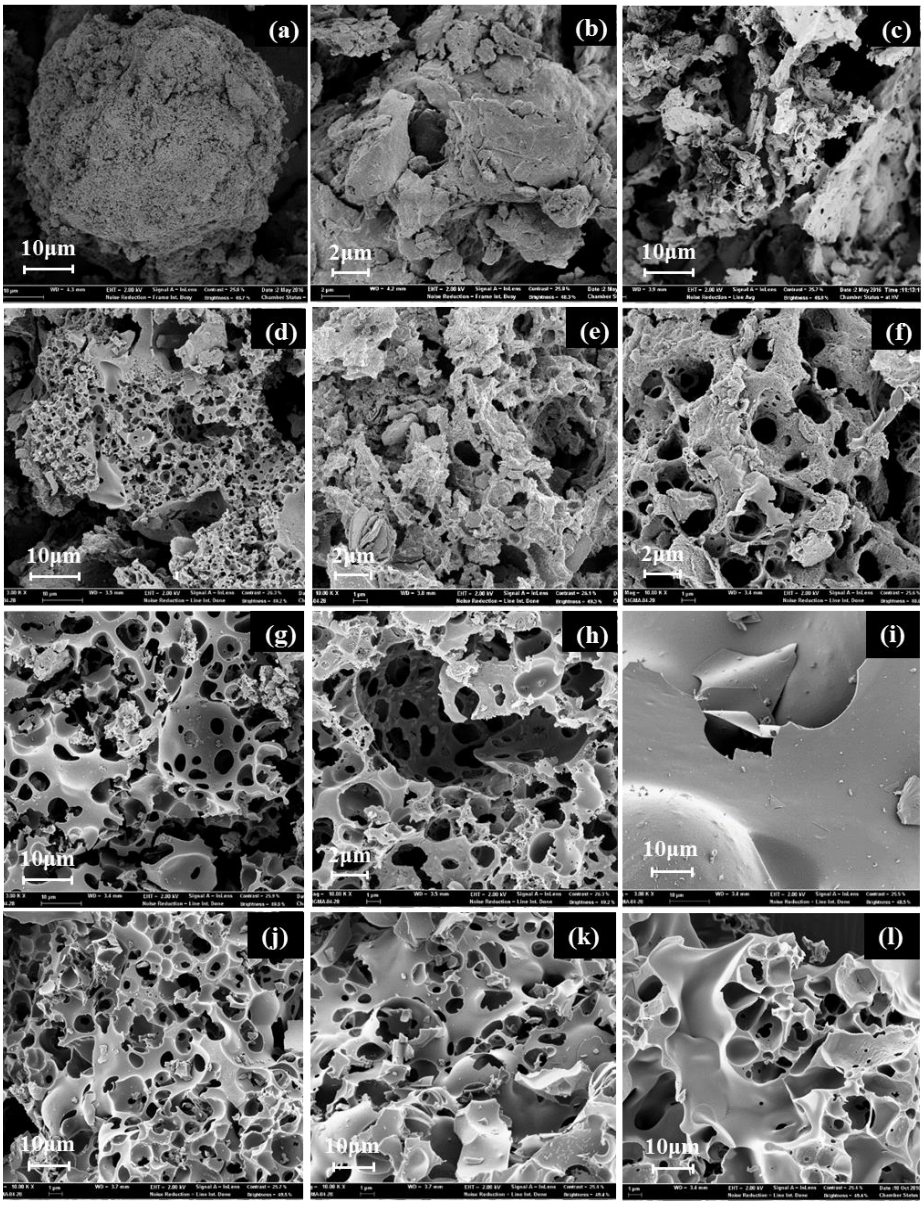

Figure 4-7. SEM images of lignin and activated carbon ((a) AL, (b) IL, (c)-(e) ILAC with different temperatures (700, 750, 800°C, respectively), (f)-(h) ILAC with different reaction times (0.5, 1, 2 h, respectively), (i)-(l) ALAC with different catalyst ratios (0, 1, 2, 6, respectively).

It is well known that textural properties such as surface area, pore volume, and pore size distribution of carbon products can be determined by N_2 adsorption-desorption analysis. Figure 4-6 shows the isotherm curves of the raw lignin samples and the produced lignin-derived activated carbons. Obviously, AL and IL possess limited adsorption capacity as they are non-porous materials. However, the adsorption volume increases after chemical activation. According to the International Union of Pure and Applied Chemistry (IUPAC) classification, lignin-derived activated carbon exhibited a type Ⅰ or type Ⅳ characteristics, reflecting microporous and mesoporous materials, respectively. The hysteresis loop caused by the pore network effect of internal voids, which is a typical characteristic of a type Ⅳ isotherm, was also observed in the P/P_0 range of 0.4-1.0.

The BET surface area and porous structures of each product obtained under various parameters are summarized in Table 4-6. As also observed in Figure 4-8, the raw lignins have low BET surface areas. For activated carbon without catalyst, BET data was not detected because of its smooth surface as shown in Figure 4-7. However, BET surface area increased even at low catalyst ratios, which may be synergistic effect with a large amount of inorganic elements in lignin.

After activation at 700°C, porous activated carbon possessing a comparable BET surface area to commercial activated carbon (Hwang et al., 2017) was produced. The maximum BET surface area of 2782 m^2/g was obtained with AL at 750°C, and a reaction time of 2 h with mesoporous characteristics. At the reaction temperature of 800°C, the BET surface area decreased while the average pore diameter increased, which is consistent with the yield and SEM analysis results in which destruction could occur from a thinned layer due to further decomposition. In addition, IL-0.5h was not fully developed, exhibited a low BET surface area and pore volume, and was largely composed of

micropores. Above a reaction time of 1 h, the micropores were converted to meso or macropores and a highly improved pore structure with a high BET surface area was produced from both lignins. The BET surface area was also affected by catalyst ratios. Activated carbon with an addition of catalyst ratio of 1 showed increased BET surface area compared to raw lignin, but the values still need to be improved for commercial use. At the catalyst ratio of 2, activated carbon with distribution of narrow pore and a comparable value of BET surface area with commercial one was obtained. The highest values of BET surface area and total pore volume were observed in activated carbon with the catalyst ratio of 4, but they decreased due to structural collapse by excessive catalyst amount. Furthermore, the overall BET surface area of ILAC (233-2227 m^2/g) was lower than that of ALAC (691-2782 m^2/g). This could be attributed to the lower contents of lignin and carbon in the raw lignin which can provide a rigid carbon structure supporting a thinned layer after the activation process.

More detailed data of the porous structure development of each product are shown in Figure 4-9. Pores in the size range of 20-50 Å were mainly generated, and relatively large pores above 100 Å were distributed more in IL while pores below 70 Å were more prevalent in AL. In addition, it was observed that pore creation and distribution properties were similar temperatures above 750°C and reaction times over 1 h, implying that more severe conditions do not help to further improve the porous structure.

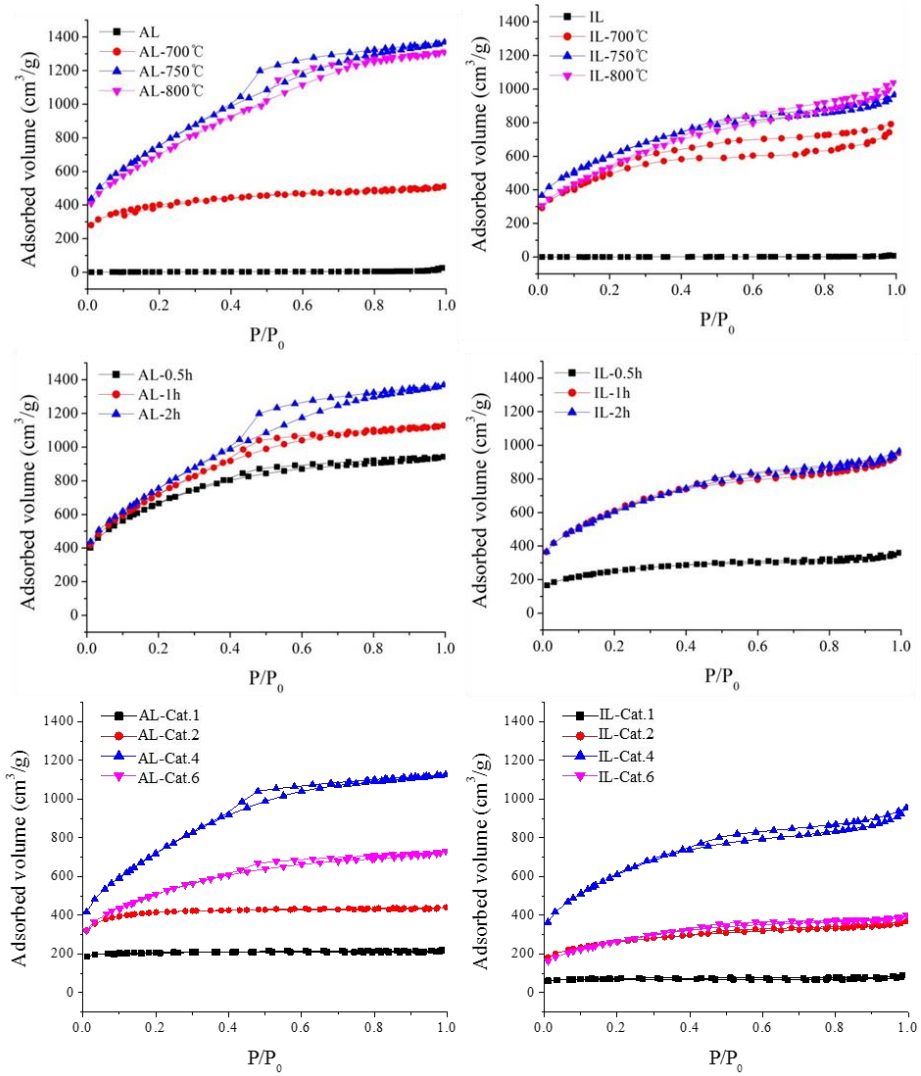

Figure 4-8. N_2 adsorption and desorption isotherms of the raw lignins and lignin-derived activated carbon.

Table 4-6. Textural features of the raw lignins and activated carbon under various reaction parameters.

Sample	Temp. (°C)	Time (hour)	Catalyst ratio	S_{total}[a] (m^2/g)	V_{total}[b] (cm^3/g)	V_{micro}[c] (cm^3/g)	V_{meso}[d] (cm^3/g)	D_{avg}[e] (Å)
AL	-	-	-	7	0.04	-	0.04	240.6
ALAC	700	2	4	1402	0.79	0.26	0.53	27.4
	750	2	4	2782	2.12	0.44	1.68	29.9
	800	2	4	2587	2.03	0.43	1.60	30.2
	750	0.5	4	2419	1.46	0.39	1.07	26.3
	750	1	4	2645	1.74	0.45	1.29	29.0
	750	1	1	691	0.47	0.29	0.18	80.6
	750	1	2	1417	0.68	0.46	0.22	24.0
	750	1	6	1821	1.13	0.11	1.02	27.4
IL	-	-	-	-	0.01	-	0.01	262.8
ILAC	700	2	4	1807	2.11	0.27	1.84	43.8
	750	2	4	2200	1.49	0.21	1.28	29.4
	800	2	4	1988	1.61	0.23	1.38	31.9
	750	0.5	4	895	0.56	0.19	0.37	29.5
	750	1	4	2227	1.48	0.24	1.24	28.8
	750	1	1	233	0.24	0.10	0.14	107.4
	750	1	2	921	0.57	0.14	0.43	29.9
	750	1	6	957	0.62	0.02	0.60	27.8

[a] BET specific surface area measured by N_2 adsorption data in the P/P_0 range from 0.06 to 0.20.
[b] Total pore volume determined from the adsorption isotherm at $P/P_0 = 0.99$.
[c] Micropore volume calculated using t-plot method.
[d] Mesopore volume calculated by the difference between V_{total} and V_{micro}.
[e] Average pore diameter determined by the adsorption data using BJH method.

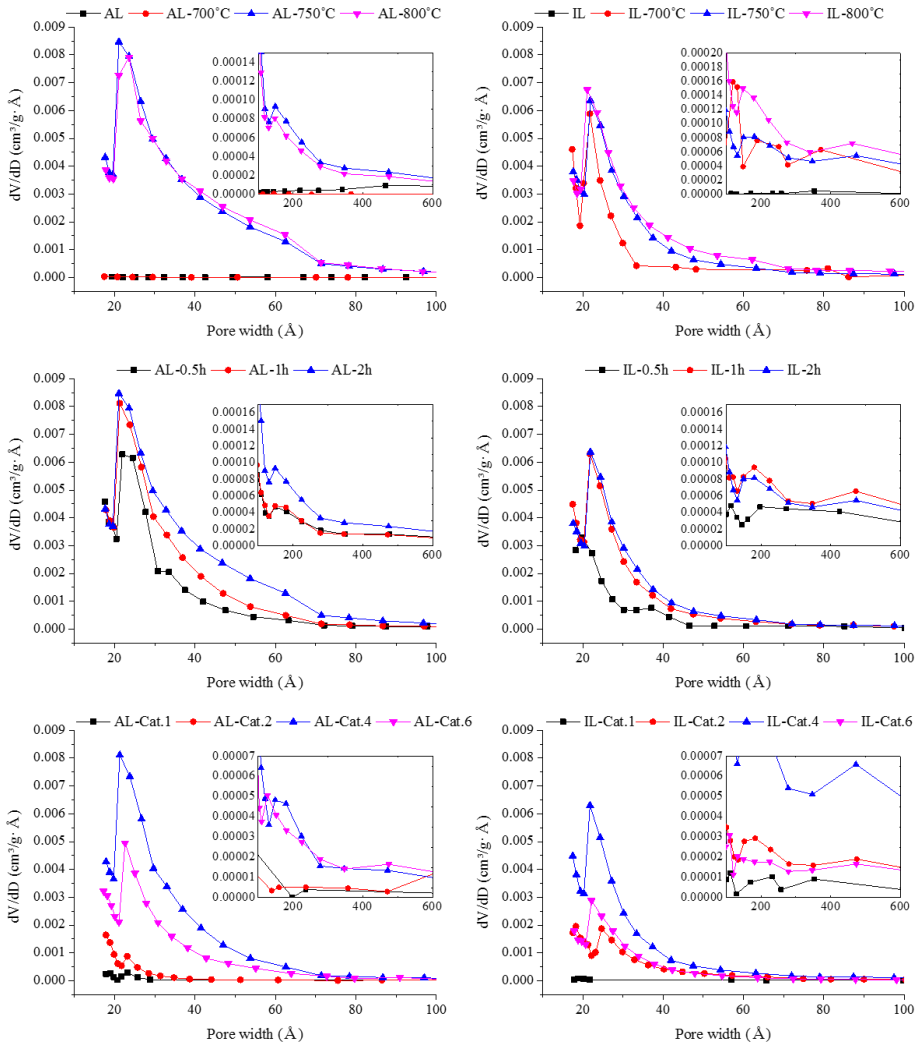

Figure 4-9. Pore size distribution of the raw lignins and lignin-derived activated carbon.

3.5. Application of lignin-derived activated carbon in value-added fields

3.5.1. Biosorbent for heavy metal or organic pollutants in aqueous solution

In order to utilization of lignin-derived activated carbon in value-added industrial fields, it was evaluated as a biosorbent for removal of aqueous pollutants. The results of adsorption capacity of ALAC and ILAC, produced under the condition of 750°C and 1 h with the catalyst ratio of 4, for 2 kinds of heavy metal (Pb^{2+} and Cd^{2+}) and 3 kinds of organic compounds (Phenol, BPA, and 2,4-D) were provided in Figure 4-10(a). For heavy metal pollutants, the adsorption capacity of lignin-derived activated carbon was 41.4-46.9 % for Pb^{2+} and 14.4-17.2 % for Cd^{2+}, which were similar or higher compared to that of CAC, 32.3 % and 18.5 %, respectively. On the other hand, lignin-derived activated carbon exhibited high adsorption capacity for organic pollutants. As described in the results of surface properties, loss of surface functional groups by dehydrogenation and deoxygenation during catalytic activated could be one of contributing factors to low removal rate of heavy metal compounds reacting in ionized form. Because each organic compound contains aromatic ring, combining interaction between adsorbate and adsorbent could increase by enhancing π-π bonding (Wang et al., 2014), which lead to high adsorption capacity for organic pollutants. Figure 4-10(b) shows the adsorption capacity using AL and ALAC produced from different catalyst ratios for 2,4-D. The capacity of AL was 25.1 % whereas that of ALAC was 100 % regardless of catalyst ratios. This indicates that the products possessing over a certain level of BET surface area around 700 m^2/g can exhibit the same adsorption

performance as that of highly activated carbon with large BET surface area (2645 m^2/g). Thus, lignin activated with only a small amount of catalyst also can be used as a high efficient adsorbent.

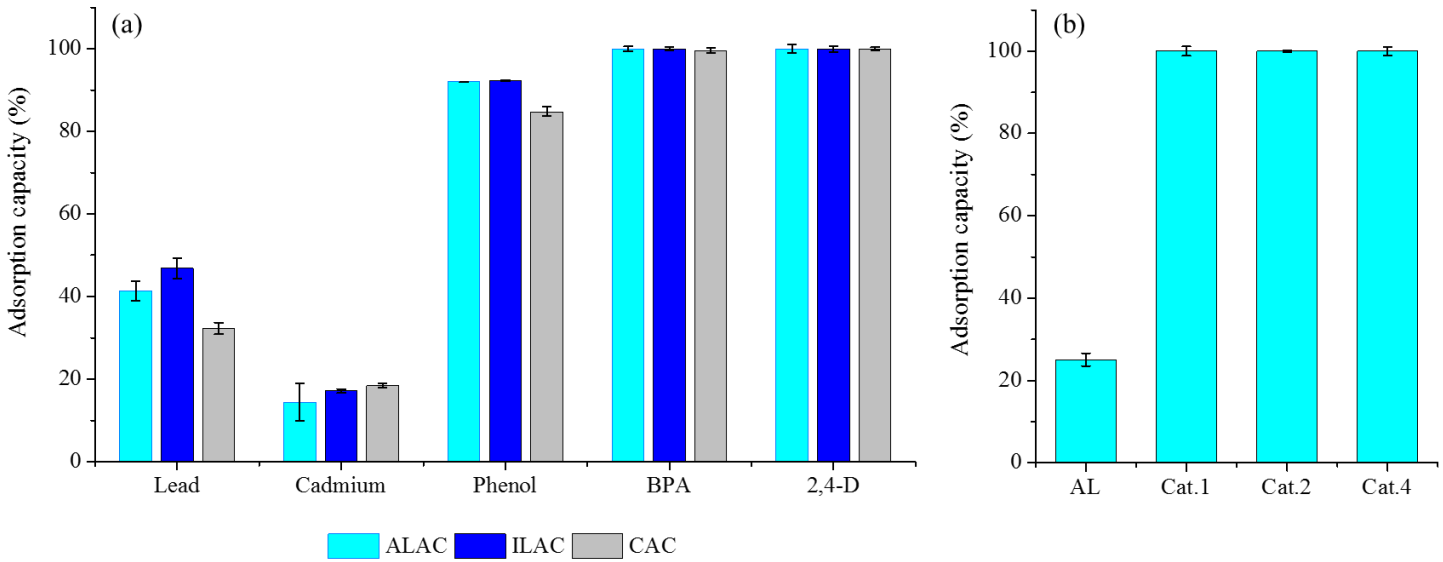

Figure 4-10. Adsorption efficiency of lignin-derived activated carbon ((a) Adsorption capacity for various heavy metals and organic compounds, (b) Adsorption capacity for 2,4-D by using activated carbon produced under different catalyst ratios).

3.5.2. Utilization as a carbon electrode for supercapacitor

The activated carbon produced from lignin under various parameters was evaluated for utilization in carbon electrodes. Both coated-type electrode and coin cell electrode were fabricated and analyzed. The results of the electrochemical performance of ALAC are shown in Figure 4-11 and Table 4-7.

The CV curves of the electrode (Figure 4-11(a)) showed a relatively nearly rectangular shape at a low scan rate, which confirms stable capacitance behavior. As the scan rate increased, a distortion in CV curves was observed due to the limited diffusion of electrolyte ion and irregularity of charge-discharge behavior at a high scan rate. Cycling stability of the electrode at a current density of 5 mA/cm^2 for 3000 cycles is shown in Figure 4-11(b). Compared to the sample from AL-Cat.1 which has a low BET surface area, the samples from AL-Cat.2 and AL-Cat.4 exhibit high stability that maintain more than 95% of their initial capacity. It demonstrates that the coin cell electrode fabricated by using lignin-derived activated carbon produced with a proper catalyst ratio has excellent cycle stability and reversibility. On the other hand, the electric properties of the sample from AL-Cat.6 was quite unstable after 500 cycle probably due to its defective structure which could be prone to occur deformation reaction during electric test.

From the coated-type electrode prepared by using lignin-activated carbon with various reaction parameters, the specific capacitance was calculated and the results were shown in Table 4-7. Except for non-catalytic activated carbon with little pore and surface area due to its crystalline structure, the electrode fabricated from AL-700°C and AL-Cat.1 had the low capacitance value of 176.3 F/g and 145.0 F/g, respectively. As can be seen in Table 4-6, their BET surface area (1402 m^2/g and 691 m^2/g) was much lower than those of the other ALAC

products. Generally, the electrochemical capacity and delivery are significantly related to the porous properties of carbon where macro and mesopores store electrolyte and improve ion diffusion, and micropores interact with ions and trap them (Zhi et al., 2013). Therefore, this sample exhibited a low rate capability due to ion diffusion and storage limitations.

Catalyst ratio also had effects on an electric capacity that it gradually increased up to 214.0 F/g as the ratio increased, but it decreased to 170.7 F/g at the catalyst ratio of 6 due to impaired structure of activated carbon. The capacitance of lignin-derived activated carbon is a comparable or higher value to that obtained from CAC in other researches (Burke, 2007; Jiang et al., 2013; Sevilla & Mokaya, 2014). Furthermore, the capacitance values of the other samples with the catalyst ratio of 4 were in the range of 200.3-214.0 F/g, implying that electrode material with high capacitance and conductivity can be manufactured by highly activated carbon derived from lignin, which is a co-product of a biorefinery process.

In order to investigate the correlation between properties and specific capacitance of lignin-derived activated carbon, principal component analysis (PCA) was used by SPSS software. For effect of properties (Figure 4-12(a)), three components were obtained, describing 88 % of the total variation in the data set. In addition, the influence of process conditions was also evaluated (Figure 4-12(b)), and two components were extracted with description of 71 %. As a result, capacitance stands closer to total specific surface area, total pore volume, and mesopore volume than other factors (Figure 4-12(a)) which can enhance the ion diffusion and storage. Catalyst ratio (Figure 4-12(b)) also largely related with capacitance because it had great effects on those properties mentioned above. Consequently, it could be possible to adjust properties of activated carbon by controlling the reaction parameters, specifically for catalyst loadings, leading to utilization of high-performance carbon electrode in industrial fields

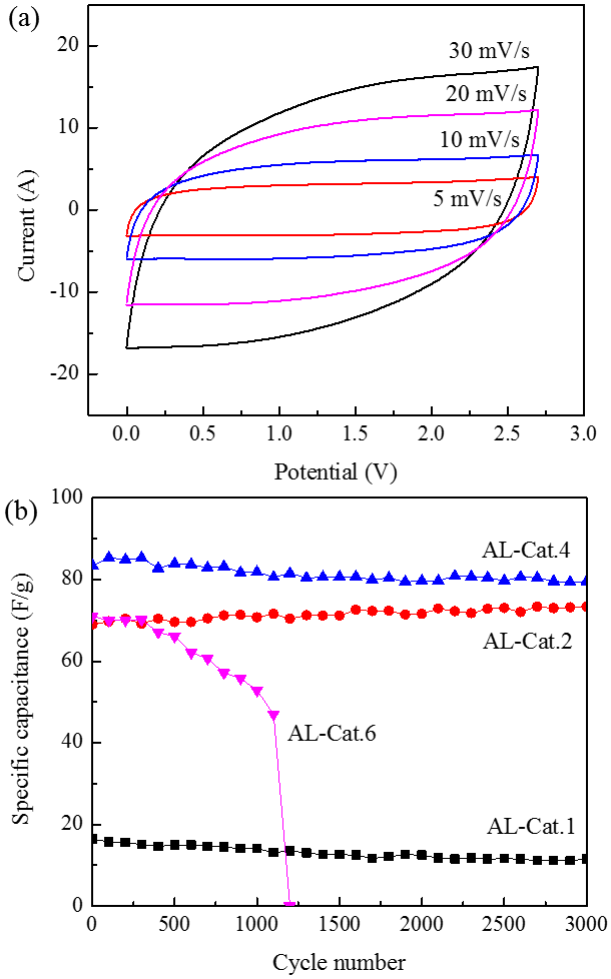

Figure 4-11. Electrochemical properties of coin cell electrode fabricated by using lignin ((a) cyclic voltammetry curves of AL-cat.2-derived electrode with different scan rates (b) cycle life data of electrode by using lignin-AC produced under different catalyst ratio).

Table 4-7. Specific capacitance of coated-type carbon electrode from lignin-derived activated carbon.

Sample	Temp.(°C)	Time (hour)	Catalyst ratio	Specific capacitance (F/g)
ALAC	700	2	4	176.3
	750	2	4	200.3
	800	2	4	205.4
	750	0.5	4	211.6
	750	1	4	214.0
	750	1	0	25.7
	750	1	1	145.0
	750	1	2	182.7
	750	1	6	170.7

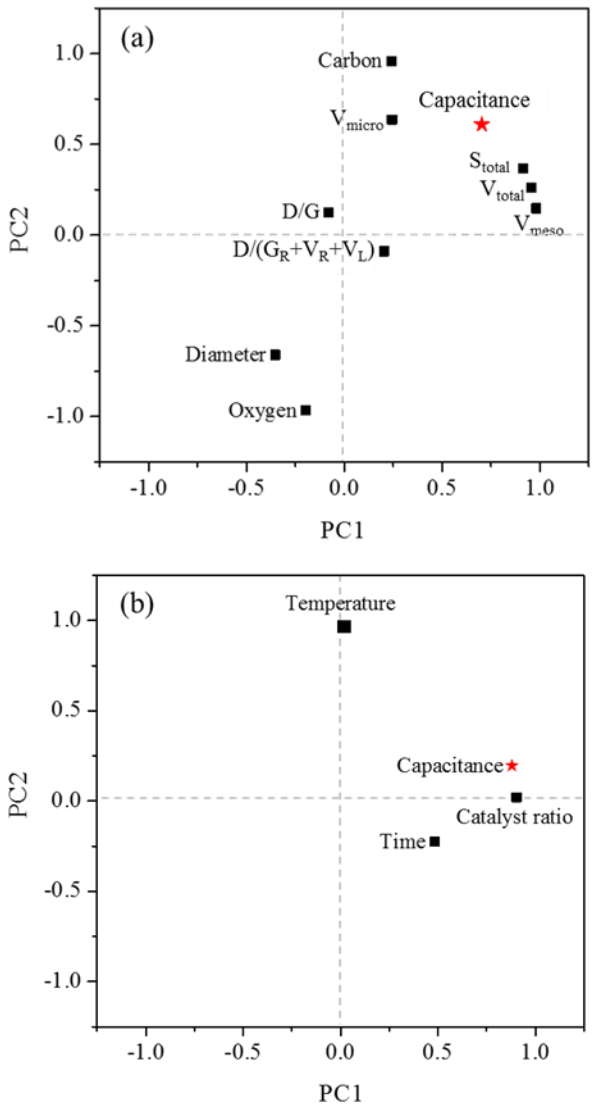

Figure 4-12. Plots from principal component analysis of specific capacitance and (a) properties of activated carbon, or (b) reaction influence factor.

4. Conclusions

In this study, activated carbon was prepared by using lignin under various temperatures, reaction times, and catalyst loadings. Characterization of the carbon products in terms of surface functionalities and structural features was performed. In addition, adsorption capacity for various heavy metals and organic pollutants and electric properties of carbon electrode by using the activated carbon were assessed. The yields of activated carbon were 19.4-26.3 wt.% for AL and 5.5-17.7 wt.% for IL. The difference could be attributed to the higher thermal stability of AL compared to IL. The raw lignins had a large number of functional groups on their surface, which decreased after the activation process. As the temperature increased, a more carbonized surface was observed due to dispersion of catalyst from the external region into the internal lattice. The structural features also changed, the turbostratic disorder structure with large aromatic ring system broke down under severe conditions along with an increase in release of benzene and naphthalene volatiles. As a result of the BET analysis, the process conditions with a temperature of 700°C and a reaction time of 0.5 h did not disrupt the carbon structure. The maximum specific surface area of 2782 m^2/g was obtained with the AL precursor at 750°C for 2 h. Furthermore, activated carbon had a large adsorption capacity for organic pollutants which comparable to that of commercial one. In addition, the carbon electrode using lignin-derived activated carbon has a potential to be used as a supercapacitor electrode. This work illustrates the influence of essential reaction parameters on the surface, structural, and porous properties of activated carbon products obtained from lignin. In addition, high performance of the products was demonstrated in the valuable industrial application of water remediation and carbon electrode. This might lead to the valorization of lignin, which is a low-cost and abundant co-product of a biorefinery process.

Chapter 5

Concluding remarks

Lignocellulosic biomass is renewable energy resources that can be converted to liquid fuel through biofuel technologies such as fast pyrolysis, hydrothermal liquefaction, and bioethanol production. Since those processes have been optimized for liquid fuel production, solid co-product has received less research attention; thus, there are few studies regarding its value-added utilization. Activated carbon is one of the approaches to utilize the macromolecular form of co-product with improving its availability by conversion to porous material. Recently, global interest has been focused on not only preparation of activated carbon using co-product, but also further steps to its application in industrial fields.

In this study, fast pyrolysis char, hydrochar, and lignin were used as precursors for preparing activated carbon by thermal catalytic conversion. The effects of various reaction parameters on characteristics of activated carbon were basically demonstrated. Changes in aromatic macromolecules and released volatile compounds during the process were investigated for better comprehensive understanding of structural development mechanism. Furthermore, its potential as an adsorbent and carbon electrode was evaluated in comparison with commercial activated carbon, and the correlation between product properties and performance was investigated.

For fast pyrolysis char, successful production of microporous or mesoporous carbon material was accomplished with the maximum specific surface area of 2711 m^2/g, and the created pore size was largely influenced by catalyst loading. After the process, aromatization in amorphous structure by reaction of KOH and fast pyrolysis char surface was more dominant rather than graphitization. As for phenol removal, the activated carbon product with the catalyst ratio of 4 showed higher adsorption capability than that of commercial activated carbon and Langmuir model was more suitable to describe adsorption process. In addition, a strong positive correlation between mesopore volume and equilibrium adsorption capacity from Langmuir model was observed, indicating

that enhanced mass transfer and pore accessibility by mesopore.

In order to control the carbon surface characteristics by facile method and investigate its effect on application performance, simultaneous modification of activated carbon by using fast pyrolysis char and hydrochar was performed under different atmospheric conditions (N_2 and zero air), and the products were compared with conventional post-acidified carbon. The preliminary tests to investigate the structural degradation mechanism by Py-GC-MS analysis showed that hydrochar has a thermally labile structure to decompose to oxygenated aromatics, while fast pyrolysis char mainly released aromatic hydrocarbon. After the activation process, activated carbon was produced at a yield of 17.1-48.4 wt.% with a de-functionalized carbon-intensive structure, but post-acidification introduced a large number of functional groups to the surfaces of the carbon products. The specific surface area and pore volume of air-activated carbon were lower than those of N_2 activated carbon. This could be attributed that excess air facilitates reactions by which pores are developed by increasing the formation of key intermediates, which can lead to structural collapse. In addition, different characteristics of the prepared carbon products resulted in different performance in various applications. Post-treated carbon products were suitable for Pb^{2+} adsorption because of their large number of functional groups, but these were not available to serve as an electric material due to the destructed surface. Meanwhile, air-activated carbon showed a high capacity for Pb^{2+} adsorption and a specific capacitance of 185.9 F/g due to its high hydrophilic oxygen-related bond content and mesopore ratio, which lead to good wettability and enhancement of accessibility, respectively.

Furthermore, two lignins (Asian lignin and Inbicon lignin) were subjected to produce activated carbon under various reaction parameters (temperature, time, and catalyst loading). High yield of activated carbon was obtained from raw lignin sample with high thermal stability and high carbon content. As temperature increased, more carbonized surface was observed by dispersion of

catalyst from external region into internal lattice. Structural features also changed that turbostratic disorder structure with large aromatic ring system broke down at severe condition along with an increase in release of benzene and naphthalene volatiles. Specific surface area was also largely affected by reaction parameters, particularly catalyst ratio. Above the catalyst ratio of 2, specific surface area of activated carbon was comparable to that of commercial product, and then it further increased up to 2782 m^2/g with the ratio of 4. When the activated carbon was used as an adsorbent for removal of heavy metals, the adsorption efficiency was 41.4-46.9 % for Pb^{2+} and 14.4-17.2 % for Cd^{2+}, which were similar or higher compared to that of commercial product. For organic pollutants, the adsorption efficiency reached about 100 % for phenol, bisphenol-A, and 2,4-dichlorophenoxyacetic acid due to an increase in π-π interaction between adsorbent and adsorbate. In addition, carbon electrode fabricated by using lignin-derived activated carbon exhibited a potential for a practical use in future. From the principal component analysis, it was revealed that total specific surface area, total pore volume, and mesopore volume are highly related with the electric performance.

This study investigated high-value application of solid co-products from biorefinery process by catalytic activation under various reaction parameters. Based on these results, co-product including char and lignin was proven to be an excellent alternative to a precursor of activated carbon, by development of macromolecular structure. Besides, it was demonstrated that effects of reaction conditions on quality of activated carbon, also related to its performance on industrial use. Thus, it can be possible to control the performance for an appropriate use by adjusting an important reaction factor, specifically for catalyst ratio. The results of this study proposed that solid co-product has a great potential for conversion to a superior functional carbon material.

References

Abussaud, B., Asmaly, H.A., Saleh, T.A., Gupta, V.K., Atieh, M.A. 2016. Sorption of phenol from waters on activated carbon impregnated with iron oxide, aluminum oxide and titanium oxide. *Journal of Molecular Liquids*, **213**, 351-359.

Altenor, S., Carene, B., Emmanuel, E., Lambert, J., Ehrhardt, J.-J., Gaspard, S. 2009. Adsorption studies of methylene blue and phenol onto vetiver roots activated carbon prepared by chemical activation. *Journal of Hazardous Materials*, **165**(1), 1029-1039.

Amen-Chen, C., Pakdel, H., Roy, C. 2001. Production of monomeric phenols by thermochemical conversion of biomass: a review. *Bioresource technology*, **79**(3), 277-299.

Annadurai, G., Juang, R.-S., Lee, D.-J. 2002. Use of cellulose-based wastes for adsorption of dyes from aqueous solutions. *Journal of Hazardous Materials*, **92**(3), 263-274.

Arseneau, D.F. 1971. Competitive reactions in the thermal decomposition of cellulose. *Canadian Journal of Chemistry*, **49**(4), 632-638.

Azadi, P., Inderwildi, O.R., Farnood, R., King, D.A. 2013. Liquid fuels, hydrogen and chemicals from lignin: A critical review. *Renewable and Sustainable Energy Reviews*, **21**, 506-523.

Azargohar, R., Dalai, A. 2006. Biochar as a precursor of activated carbon. *Appl Biochem Biotechnol*, **131**(1-3), 762-773.

Azargohar, R., Nanda, S., Kozinski, J.A., Dalai, A.K., Sutarto, R. 2014. Effects of temperature on the physicochemical characteristics of fast pyrolysis bio-chars derived from Canadian waste biomass. *Fuel*, **125**, 90-100.

Barrett, E.P., Joyner, L.G., Halenda, P.P. 1951. The determination of pore volume and area distributions in porous substances. I. Computations from nitrogen isotherms. *Journal of the American Chemical society*, **73**(1), 373-380.

Beesley, L., Moreno-Jiménez, E., Gomez-Eyles, J.L., Harris, E., Robinson, B.,

Sizmur, T. 2011. A review of biochars' potential role in the remediation, revegetation and restoration of contaminated soils. *Environmental Pollution*, **159**(12), 3269-3282.

Bobleter, O. 1994. Hydrothermal degradation of polymers derived from plants. *Progress in polymer science*, **19**(5), 797-841.

Boehm, H. 1994. Some aspects of the surface chemistry of carbon blacks and other carbons. *Carbon*, **32**(5), 759-769.

Boehm, H. 2002. Surface oxides on carbon and their analysis: a critical assessment. *Carbon*, **40**(2), 145-149.

Brebu, M., Vasile, C. 2010. Thermal degradation of lignin—a review. *Cellulose Chemistry & Technology*, **44**(9), 353.

Brežný, R., Šurina, I., Košík, M. 1984. Low Temperature Thermolysis of Lignins-II. Thermofractography and Thermal Analysis of β-0-4 Model Compounds. *Holzforschung-International Journal of the Biology, Chemistry, Physics and Technology of Wood*, **38**(1), 19-24.

Bridgewater, A.V. 2004. Biomass fast pyrolysis. *Thermal science*, **8**(2), 21-50.

Bridgwater, A., Meier, D., Radlein, D. 1999. An overview of fast pyrolysis of biomass. *Organic geochemistry*, **30**(12), 1479-1493.

Brunauer, S., Emmett, P.H., Teller, E. 1938. Adsorption of gases in multimolecular layers. *Journal of the American chemical society*, **60**(2), 309-319.

Burke, A. 2007. R&D considerations for the performance and application of electrochemical capacitors. *Electrochimica Acta*, **53**(3), 1083-1091.

Canadell, J.G., Schulze, E.D. 2014. Global potential of biospheric carbon management for climate mitigation. *Nature communications*, **5**.

Cao, L., Chen, D., Li, W., Caruso, R.A. 2014. Hierarchically Porous Titania Networks with Tunable Anatase: Rutile Ratios and Their Enhanced Photocatalytic Activities. *ACS applied materials & interfaces*, **6**(15), 13129-13137.

Carrott, P., Carrott, M.R. 2009. Using alkali metals to control reactivity and porosity during physical activation of demineralised kraft lignin. *Carbon*, **47**(4), 1012-1017.

Chen, J.P., Wu, S. 2004. Acid/base-treated activated carbons: characterization of functional groups and metal adsorptive properties. *Langmuir*, **20**(6), 2233-2242.

Chen, L., Ji, T., Mu, L., Shi, Y., Brisbin, L., Guo, Z., Khan, M.A., Young, D.P., Zhu, J. 2016. Facile synthesis of mesoporous carbon nanocomposites from natural biomass for efficient dye adsorption and selective heavy metal removal. *RSC Advances*, **6**(3), 2259-2269.

Czernik, S., Bridgwater, A. 2004. Overview of applications of biomass fast pyrolysis oil. *Energy & Fuels*, **18**(2), 590-598.

Dąbrowski, A., Podkościelny, P., Hubicki, Z., Barczak, M. 2005. Adsorption of phenolic compounds by activated carbon-a critical review. *Chemosphere*, **58**(8), 1049-1070.

Dandekar, A., Baker, R., Vannice, M. 1998. Characterization of activated carbon, graphitized carbon fibers and synthetic diamond powder using TPD and DRIFTS. *Carbon*, **36**(12), 1821-1831.

Demirbas, A. 2004. Effects of temperature and particle size on bio-char yield from pyrolysis of agricultural residues. *Journal of Analytical and Applied Pyrolysis*, **72**(2), 243-248.

Dıaz-Terán, J., Nevskaia, D., Fierro, J., López-Peinado, A., Jerez, A. 2003. Study of chemical activation process of a lignocellulosic material with KOH by XPS and XRD. *Microporous and mesoporous materials*, **60**(1), 173-181.

Dıaz-Teran, J., Nevskaia, D., López-Peinado, A., Jerez, A. 2001. Porosity and adsorption properties of an activated charcoal. *Colloids and Surfaces A: Physicochemical and Engineering Aspects*, **187**, 167-175.

Dinjus, E., Kruse, A., Troeger, N. 2011. Hydrothermal carbonization–1.

Influence of lignin in lignocelluloses. *Chemical Engineering & Technology*, **34**(12), 2037-2043.

Essandoh, M., Kunwar, B., Pittman, C.U., Mohan, D., Mlsna, T. 2015. Sorptive removal of salicylic acid and ibuprofen from aqueous solutions using pine wood fast pyrolysis biochar. *Chemical Engineering Journal*, **265**, 219-227.

Fiddler, W., Parker, W.E., Wasserman, A.E., Doerr, R.C. 1967. Thermal decomposition of ferulic acid. *Journal of agricultural and food chemistry*, **15**(5), 757-761.

Figueiredo, J., Pereira, M., Freitas, M., Orfao, J. 1999. Modification of the surface chemistry of activated carbons. *carbon*, **37**(9), 1379-1389.

Fu, K., Yue, Q., Gao, B., Sun, Y., Zhu, L. 2013. Preparation, characterization and application of lignin-based activated carbon from black liquor lignin by steam activation. *Chemical engineering journal*, **228**, 1074-1082.

Gao, Y., Yue, Q., Gao, B., Sun, Y., Wang, W., Li, Q., Wang, Y. 2013. Preparation of high surface area-activated carbon from lignin of papermaking black liquor by KOH activation for Ni (II) adsorption. *Chemical Engineering Journal*, **217**, 345-353.

Gardella Jr, J.A., Ferguson, S.A., Chin, R.L. 1986. $\pi^* \leftarrow \pi$ shakeup satellites for the analysis of structure and bonding in aromatic polymers by X-Ray Photoelectron Spectroscopy. *Applied spectroscopy*, **40**(2), 224-232.

Girgis, B.S., Temerk, Y.M., Gadelrab, M.M., Abdullah, I.D. 2007. X-ray Diffraction Patterns of Activated Carbons Prepared under Various Conditions. *Carbon letters*, **8**(2), 95-100.

Global：Industry：Analysts：Inc. 2017. Stringent environmental regulations to boost growth in the global activated carbon market. *Global Industry Analysts, Inc.*

Gomez-Serrano, V., Pastor-Villegas, J., Perez-Florindo, A., Duran-Valle, C., Valenzuela-Calahorro, C. 1996. FT-IR study of rockrose and of char and activated carbon. *Journal of analytical and applied pyrolysis*, **36**(1), 71-80.

Gong, G.-z., Qiang, X., Zheng, Y.-f., Ye, S.-f., Chen, Y.-f. 2009. Regulation of pore size distribution in coal-based activated carbon. *New Carbon Materials*, **24**(2), 141-146.

González-García, P., Centeno, T., Urones-Garrote, E., Ávila-Brande, D., Otero-Díaz, L. 2013. Microstructure and surface properties of lignocellulosic-based activated carbons. *Applied Surface Science*, **265**, 731-737.

Grand View Research. 2016. Activated Carbon Market Analysis By Product (Powdered Activated Carbon (PAC), Granular Activated Carbon (GAC)), By Application (Liquid Phase, Gas Phase), By End-Use (Water Treatment, Food & Beverages, Pharmaceutical & Medical, Automotive, Air Purification) And Segment Forecasts To 2024. in: *Market Research Report*.

Greenhalf, C., Nowakowski, D., Harms, A., Titiloye, J., Bridgwater, A. 2013. A comparative study of straw, perennial grasses and hardwoods in terms of fast pyrolysis products. *Fuel*, **108**, 216-230.

Groen, J.C., Peffer, L.A., Pérez-Ramírez, J. 2003. Pore size determination in modified micro-and mesoporous materials. Pitfalls and limitations in gas adsorption data analysis. *Microporous and Mesoporous Materials*, **60**(1), 1-17.

Hameed, B., Rahman, A. 2008. Removal of phenol from aqueous solutions by adsorption onto activated carbon prepared from biomass material. *Journal of Hazardous Materials*, **160**(2), 576-581.

Han, J., Kwon, J.H., Lee, J.-W., Lee, J.H., Roh, K.C. 2017. An effective approach to preparing partially graphitic activated carbon derived from structurally separated pitch pine biomass. Carbon, 118, 431-437.

He, Y., Pang, Y., Liu, Y., Li, X., Wang, K. 2008. Physicochemical characterization of rice straw pretreated with sodium hydroxide in the solid state for enhancing biogas production. *Energy & Fuels*, **22**(4), 2775-2781.

Hsieh, C.-T., Teng, H. 2000. Influence of mesopore volume and adsorbate size on adsorption capacities of activated carbons in aqueous solutions. *Carbon*, **38**(6), 863-869.

Hu, S., Hsieh, Y.-L. 2017. Lignin derived activated carbon particulates as an electric supercapacitor: carbonization and activation on porous structures and microstructures. *RSC Advances*, **7**(48), 30459-30468.

Hwang, H., Oh, S., Cho, T.-S., Choi, I.-G., Choi, J.W. 2013. Fast pyrolysis of potassium impregnated poplar wood and characterization of its influence on the formation as well as properties of pyrolytic products. *Bioresource technology*, **150**, 359-366.

Hwang, H., Oh, S., Choi, I.-G., Choi, J.W. 2015. Catalytic effects of magnesium on the characteristics of fast pyrolysis products–Bio-oil, bio-char, and non-condensed pyrolytic gas fractions. *Journal of Analytical and Applied Pyrolysis*, **113**, 27-34.

Hwang, H., Oh, S., Kim, J.-Y., Lee, S., Cho, T., Choi, J.W. 2012. Effect of Particle Size and Moisture Content of Woody Biomass on the Feature of Pyrolytic Products. *Journal of the Korean Wood Science and Technology*, **40**(6), 445-453.

Hwang, H., Sahin, O., Choi, J.W. 2017. Manufacturing a super-active carbon using fast pyrolysis char from biomass and correlation study on structural features and phenol adsorption. *RSC Advances*, **7**(67), 42192-42202.

IRENA. 2014. Global bioenergy : supply and demand projections. in: *A working paper for REmap 2030*, (Ed.) D.S. Shunichi Nakada, Dolf Gielen.

Jain, A., Balasubramanian, R., Srinivasan, M. 2016. Hydrothermal conversion

of biomass waste to activated carbon with high porosity: A review. *Chemical Engineering Journal*, **283**, 789-805.

Jiang, L., Yan, J., Hao, L., Xue, R., Sun, G., Yi, B. 2013. High rate performance activated carbons prepared from ginkgo shells for electrochemical supercapacitors. *Carbon*, **56**, 146-154.

Jin, Z., Katsumata, K.S., Lam, T.B.T., Iiyama, K. 2006. Covalent linkages between cellulose and lignin in cell walls of coniferous and nonconiferous woods. *Biopolymers*, **83**(2), 103-110.

Kai, D., Tan, M.J., Chee, P.L., Chua, Y.K., Yap, Y.L., Loh, X.J. 2016. Towards lignin-based functional materials in a sustainable world. *Green Chemistry*, **18**(5), 1175-1200.

Kambo, H.S., Dutta, A. 2015. A comparative review of biochar and hydrochar in terms of production, physico-chemical properties and applications. *Renewable and Sustainable Energy Reviews*, **45**, 359-378.

Kaparaju, P., Felby, C. 2010. Characterization of lignin during oxidative and hydrothermal pre-treatment processes of wheat straw and corn stover. *Bioresource Technology*, **101**(9), 3175-3181.

Karayıldırım, T., Sınağ, A., Kruse, A. 2008. Char and coke formation as unwanted side reaction of the hydrothermal biomass gasification. *Chemical engineering & technology*, **31**(11), 1561-1568.

Kastner, J.R., Miller, J., Geller, D.P., Locklin, J., Keith, L.H., Johnson, T. 2012. Catalytic esterification of fatty acids using solid acid catalysts generated from biochar and activated carbon. *Catalysis today*, **190**(1), 122-132.

Keiluweit, M., Nico, P.S., Johnson, M.G., Kleber, M. 2010. Dynamic molecular structure of plant biomass-derived black carbon (biochar). *Environmental science & technology*, **44**(4), 1247-1253.

Khezami, L., Chetouani, A., Taouk, B., Capart, R. 2005. Production and characterisation of activated carbon from wood components in powder:

cellulose, lignin, xylan. *Powder Technology*, **157**(1), 48-56.

Kim, J.-Y., Lee, J.H., Park, J., Kim, J.K., An, D., Song, I.K., Choi, J.W. 2015. Catalytic pyrolysis of lignin over HZSM-5 catalysts: Effect of various parameters on the production of aromatic hydrocarbon. *Journal of Analytical and Applied Pyrolysis*, **114**, 273-280.

Kim, K.H., Eom, I.Y., Lee, S.M., Choi, D., Yeo, H., Choi, I.-G., Choi, J.W. 2011. Investigation of physicochemical properties of biooils produced from yellow poplar wood (Liriodendron tulipifera) at various temperatures and residence times. *Journal of Analytical and Applied Pyrolysis*, **92**(1), 2-9.

Kim, K.H., Kim, J.-Y., Cho, T.-S., Choi, J.W. 2012. Influence of pyrolysis temperature on physicochemical properties of biochar obtained from the fast pyrolysis of pitch pine (Pinus rigida). *Bioresource technology*, **118**, 158-162.

Kleinert, M., Barth, T. 2008. Phenols from lignin. *Chemical engineering & technology*, **31**(5), 736-745.

Knop, A., Pilato, L.A. 2013. *Phenolic resins: chemistry, applications and performance*. Springer Science & Business Media.

Kruse, A., Dinjus, E. 2007. Hot compressed water as reaction medium and reactant: 2. Degradation reactions. *The Journal of Supercritical Fluids*, **41**(3), 361-379.

Kumar, S., Mohanty, A., Erickson, L., Misra, M. 2009. Lignin and its applications with polymers. *Journal of Biobased Materials and Bioenergy*, **3**(1), 1-24.

Lalhruaitluanga, H., Jayaram, K., Prasad, M., Kumar, K. 2010. Lead (II) adsorption from aqueous solutions by raw and activated charcoals of Melocanna baccifera Roxburgh (bamboo)—A comparative study. *Journal of Hazardous Materials*, **175**(1), 311-318.

Lee, J.H., Hwang, H., Moon, J., Choi, J.W. 2016. Characterization of

hydrothermal liquefaction products from coconut shell in the presence of selected transition metal chlorides. *Journal of Analytical and Applied Pyrolysis*, **122**, 415-421.

Lee, J.W., Kidder, M., Evans, B.R., Paik, S., Buchanan Iii, A., Garten, C.T., Brown, R.C. 2010. Characterization of biochars produced from cornstovers for soil amendment. *Environmental Science & Technology*, **44**(20), 7970-7974.

Li, H., Li, W., Zhang, Y., Wang, T., Wang, B., Xu, W., Jiang, L., Song, W., Shu, C., Wang, C. 2011a. Chrysanthemum-like α-FeOOH microspheres produced by a simple green method and their outstanding ability in heavy metal ion removal. *Journal of Materials Chemistry*, **21**(22), 7878-7881.

Li, W., Cao, C.-Y., Wu, L.-Y., Ge, M.-F., Song, W.-G. 2011b. Superb fluoride and arsenic removal performance of highly ordered mesoporous aluminas. *Journal of hazardous materials*, **198**, 143-150.

Li, W., Chen, D., Xia, F., Tan, J.Z., Huang, P.-P., Song, W.-G., Nursam, N.M., Caruso, R.A. 2016. Extremely high arsenic removal capacity for mesoporous aluminium magnesium oxide composites. *Environmental Science: Nano*, **3**(1), 94-106.

Li, W., Zhang, L.-S., Wang, Q., Yu, Y., Chen, Z., Cao, C.-Y., Song, W.-G. 2012. Low-cost synthesis of graphitic carbon nanofibers as excellent room temperature sensors for explosive gases. *Journal of Materials Chemistry*, **22**(30), 15342-15347.

Li, X., Han, C., Chen, X., Shi, C. 2010. Preparation and performance of straw based activated carbon for supercapacitor in non-aqueous electrolytes. *Microporous and Mesoporous Materials*, **131**(1), 303-309.

Li, X., Hayashi, J.-i., Li, C.-Z. 2006. FT-Raman spectroscopic study of the evolution of char structure during the pyrolysis of a Victorian brown coal. *Fuel*, **85**(12), 1700-1707.

Li, Y., Shao, J., Wang, X., Deng, Y., Yang, H., Chen, H. 2014. Characterization of modified biochars derived from bamboo pyrolysis and their utilization for target component (furfural) adsorption. *Energy & Fuels*, **28**(8), 5119-5127.

Libra, J.A., Ro, K.S., Kammann, C., Funke, A., Berge, N.D., Neubauer, Y., Titirici, M.-M., Fühner, C., Bens, O., Kern, J. 2011. Hydrothermal carbonization of biomass residuals: a comparative review of the chemistry, processes and applications of wet and dry pyrolysis. *Biofuels*, **2**(1), 71-106.

Lima, I.M., Boateng, A.A., Klasson, K.T. 2010. Physicochemical and adsorptive properties of fast-pyrolysis bio-chars and their steam activated counterparts. *Journal of chemical technology and biotechnology*, **85**(11), 1515-1521.

Lin-Vien, D., Colthup, N.B., Fateley, W.G., Grasselli, J.G. 1991. *The handbook of infrared and Raman characteristic frequencies of organic molecules*. Elsevier.

Lin, X., Wang, C., Ideta, K., Miyawaki, J., Nishiyama, Y., Wang, Y., Yoon, S., Mochida, I. 2014. Insights into the functional group transformation of a Chinese brown coal during slow pyrolysis by combining various experiments. *Fuel*, **118**, 257-264.

Lin, Z., Liu, Y., Yao, Y., Hildreth, O.J., Li, Z., Moon, K., Wong, C.-p. 2011. Superior capacitance of functionalized graphene. *The Journal of Physical Chemistry C*, **115**(14), 7120-7125.

Liu, M.-C., Kong, L.-B., Zhang, P., Luo, Y.-C., Kang, L. 2012. Porous wood carbon monolith for high-performance supercapacitors. *Electrochimica Acta*, **60**, 443-448.

Liu, W.-J., Jiang, H., Yu, H.-Q. 2015. Thermochemical conversion of lignin to functional materials: a review and future directions. *Green Chemistry*,

17(11), 4888-4907.

Liu, W.-J., Zeng, F.-X., Jiang, H., Zhang, X.-S. 2011. Preparation of high adsorption capacity bio-chars from waste biomass. *Bioresour Technol*, **102**(17), 8247-8252.

Liu, Z., Zhang, F.-S. 2009. Removal of lead from water using biochars prepared from hydrothermal liquefaction of biomass. *Journal of Hazardous Materials*, **167**(1), 933-939.

Liu, Z., Zhang, F.-S., Wu, J. 2010. Characterization and application of chars produced from pinewood pyrolysis and hydrothermal treatment. *Fuel*, **89**(2), 510-514.

Lora, J.H., Glasser, W.G. 2002. Recent industrial applications of lignin: a sustainable alternative to nonrenewable materials. *Journal of Polymers and the Environment*, **10**(1-2), 39-48.

Lozano-Castello, D., Calo, J., Cazorla-Amoros, D., Linares-Solano, A. 2007. Carbon activation with KOH as explored by temperature programmed techniques, and the effects of hydrogen. *Carbon*, **45**(13), 2529-2536.

Ludwig, C.H., Sarkanen, K. 1971. *Lignins: occurrence, formation, structure and reactions*. Wiley-Interscience.

Müller-Hagedorn, M., Bockhorn, H., Krebs, L., Müller, U. 2003. A comparative kinetic study on the pyrolysis of three different wood species. *Journal of analytical and Applied Pyrolysis*, **68**, 231-249.

Mani, S., Kastner, J.R., Juneja, A. 2013. Catalytic decomposition of toluene using a biomass derived catalyst. *Fuel processing technology*, **114**, 118-125.

MARSH, H. 2006. *Rodriguez-Reinoso F. Activated carbon*. Amsterdam: Elsevier.

McKee, D.W. 1982. Gasification of graphite in carbon dioxide and water vapor—the catalytic effects of alkali metal salts. *Carbon*, **20**(1), 59-66.

McKendry, P. 2002. Energy production from biomass (part 1): overview of

biomass. *Bioresource technology*, **83**(1), 37-46.

Mohan, D., Pittman, C.U., Bricka, M., Smith, F., Yancey, B., Mohammad, J., Steele, P.H., Alexandre-Franco, M.F., Gómez-Serrano, V., Gong, H. 2007. Sorption of arsenic, cadmium, and lead by chars produced from fast pyrolysis of wood and bark during bio-oil production. *Journal of colloid and interface science*, **310**(1), 57-73.

Mohan, D., Sarswat, A., Ok, Y.S., Pittman, C.U. 2014. Organic and inorganic contaminants removal from water with biochar, a renewable, low cost and sustainable adsorbent–a critical review. *Bioresource technology*, **160**, 191-202.

Montes-Moran, M., Suarez, D., Menéndez, J., Fuente, E. 2004. On the nature of basic sites on carbon surfaces: an overview. *Carbon*, **42**(7), 1219-1225.

Nair, K., Kumar, R., Thomas, S., Schit, S., Ramamurthy, K. 2000. Rheological behavior of short sisal fiber-reinforced polystyrene composites. *Composites Part A: Applied Science and Manufacturing*, **31**(11), 1231-1240.

Naseem, R., Tahir, S. 2001. Removal of Pb (II) from aqueous/acidic solutions by using bentonite as an adsorbent. *Water Research*, **35**(16), 3982-3986.

Nimlos, M.R., Blanksby, S.J., Ellison, G.B., Evans, R.J. 2003. Enhancement of 1, 2-dehydration of alcohols by alkali cations and protons: a model for dehydration of carbohydrates. *Journal of analytical and applied pyrolysis*, **66**(1), 3-27.

Nursam, N.M., Tan, J.Z., Wang, X., Li, W., Xia, F., Caruso, R.A. 2016. Mesoporous Nitrogen-Modified Titania with Enhanced Dye Adsorption Capacity and Visible Light Photocatalytic Activity. *ChemistrySelect*, **1**(15), 4868-4878.

Otowa, T., Tanibata, R., Itoh, M. 1993. Production and adsorption

characteristics of MAXSORB: high-surface-area active carbon. *Gas separation & purification*, **7**(4), 241-245.

Pandolfo, A., Hollenkamp, A. 2006. Carbon properties and their role in supercapacitors. *Journal of power sources*, **157**(1), 11-27.

Pavia, D.L., Lampman, G.M., Kriz, G.S., Vyvyan, J.A. 2008. *Introduction to spectroscopy*. Cengage Learning.

Popescu, M.-C., Popescu, C.-M., Lisa, G., Sakata, Y. 2011. Evaluation of morphological and chemical aspects of different wood species by spectroscopy and thermal methods. *Journal of Molecular Structure*, **988**(1), 65-72.

Qian, K., Kumar, A., Zhang, H., Bellmer, D., Huhnke, R. 2015. Recent advances in utilization of biochar. *Renewable and Sustainable Energy Reviews*, **42**, 1055-1064.

Raymundo-Pinero, E., Azais, P., Cacciaguerra, T., Cazorla-Amorós, D., Linares-Solano, A., Béguin, F. 2005. KOH and NaOH activation mechanisms of multiwalled carbon nanotubes with different structural organisation. *Carbon*, **43**(4), 786-795.

Research, G.V. 2016. *Activated Carbon Market Analysis By Product (Powdered Activated Carbon (PAC), Granular Activated Carbon (GAC)), By Application (Liquid Phase, Gas Phase), By End-Use (Water Treatment, Food & Beverages, Pharmaceutical & Medical, Automotive, Air Purification) And Segment Forecasts To 2024*.

Rincón-Silva, N.G., Moreno-Piraján, J.C., Giraldo, L. 2016. Equilibrium, kinetics and thermodynamics study of phenols adsorption onto activated carbon obtained from lignocellulosic material (Eucalyptus Globulus labill seed). *Adsorption*, **22**(1), 33-48.

Rodríguez Correa, C., Stollovsky, M., Hehr, T., Rauscher, Y., Rolli, B., Kruse, A. 2017. Influence of the Carbonization Process on Activated Carbon Properties from Lignin and Lignin-Rich Biomasses. *ACS Sustainable*

Chemistry & Engineering, **5**(9), 8222-8233.

Romanos, J., Beckner, M., Rash, T., Firlej, L., Kuchta, B., Yu, P., Suppes, G., Wexler, C., Pfeifer, P. 2011. Nanospace engineering of KOH activated carbon. *Nanotechnology*, **23**(1), 015401.

Saha, D., Li, Y., Bi, Z., Chen, J., Keum, J.K., Hensley, D.K., Grappe, H.A., Meyer III, H.M., Dai, S., Paranthaman, M.P. 2014. Studies on supercapacitor electrode material from activated lignin-derived mesoporous carbon. *Langmuir*, **30**(3), 900-910.

Samuel, R., Pu, Y., Raman, B., Ragauskas, A.J. 2010. Structural characterization and comparison of switchgrass ball-milled lignin before and after dilute acid pretreatment. Applied biochemistry and biotechnology, 162(1), 62-74.

Schröder, E., Thomauske, K., Weber, C., Hornung, A., Tumiatti, V. 2007. Experiments on the generation of activated carbon from biomass. *Journal of analytical and applied pyrolysis*, **79**(1), 106-111.

Sevilla, M., Fuertes, A.B. 2009. The production of carbon materials by hydrothermal carbonization of cellulose. *Carbon*, **47**(9), 2281-2289.

Sevilla, M., Mokaya, R. 2014. Energy storage applications of activated carbons: supercapacitors and hydrogen storage. *Energy & Environmental Science*, **7**(4), 1250-1280.

Sevilla, M., Yu, L., Ania, C.O., Titirici, M.M. 2014. Supercapacitive Behavior of Two Glucose-Derived Microporous Carbons: Direct Pyrolysis versus Hydrothermal Carbonization. *ChemElectroChem*, **1**(12), 2138-2145.

Shafizadeh, F. 1982. Introduction to pyrolysis of biomass. *Journal of Analytical and Applied Pyrolysis*, **3**(4), 283-305.

Shen, G., Tao, S., Wang, W., Yang, Y., Ding, J., Xue, M., Min, Y., Zhu, C., Shen, H., Li, W. 2011. Emission of oxygenated polycyclic aromatic hydrocarbons from indoor solid fuel combustion. *Environmental*

science & technology, **45**(8), 3459.

Shimada, K., Hosoya, S., Ikeda, T. 1997. Condensation reactions of softwood and hardwood lignin model compounds under organic acid cooking conditions. *Journal of wood chemistry and technology*, **17**(1-2), 57-72.

Shimodaira, N., Masui, A. 2002. Raman spectroscopic investigations of activated carbon materials. *Journal of Applied Physics*, **92**(2), 902-909.

Silverstein, R.A., Chen, Y., Sharma-Shivappa, R.R., Boyette, M.D., Osborne, J. 2007. A comparison of chemical pretreatment methods for improving saccharification of cotton stalks. *Bioresource Technology*, **98**(16), 3000-3011.

Tan, J.Z., Nursam, N.M., Xia, F., Sani, M.-A., Li, W., Wang, X., Caruso, R.A. 2017. High-Performance Coral Reef-like Carbon Nitrides: Synthesis and Application in Photocatalysis and Heavy Metal Ion Adsorption. *ACS Applied Materials & Interfaces*, **9**(5), 4540-4547.

Tao, X., Xiaoqin, L. 2008. Peanut shell activated carbon: characterization, surface modification and adsorption of Pb2+ from aqueous solution. *Chinese Journal of Chemical Engineering*, **16**(3), 401-406.

Ternero-Hidalgo, J.J., Rosas, J.M., Palomo, J., Valero-Romero, M.J., Rodríguez-Mirasol, J., Cordero, T. 2016. Functionalization of activated carbons by HNO_3 treatment: Influence of phosphorus surface groups. *Carbon*, **101**, 409-419.

Toor, S.S., Rosendahl, L., Rudolf, A. 2011. Hydrothermal liquefaction of biomass: a review of subcritical water technologies. *Energy*, **36**(5), 2328-2342.

Transparency Market Research. 2013. Activated Carbon Market (Powdered, Granular) for Liquid Phase and Gas Phase Applications in Water Treatment, Food & Beverage Processing, Pharmaceutical & Medical, Automotive and Air purification - Global Industry Analysis, Size, Share, Growth, Trends and Forecast, 2013 - 2019.

Tuinstra, F., Koenig, J.L. 1970. Raman spectrum of graphite. *The Journal of Chemical Physics*, **53**(3), 1126-1130.

Wada, M., Okano, T. 2001. Localization of Iα and Iβ phases in algal cellulose revealed by acid treatments. *Cellulose*, **8**(3), 183-188.

Wagner, C., Riggs, W., Davis, L., Moulder, J., Muilenberg, G. *Handbook of X-ray photoelectron spectroscopy (1978) Eden Prairie*. Minesota.

Wang, H., Zhou, A., Peng, F., Yu, H., Yang, J. 2007. Mechanism study on adsorption of acidified multiwalled carbon nanotubes to Pb (II). *Journal of Colloid and Interface Science*, **316**(2), 277-283.

Wang, J., Kaskel, S. 2012. KOH activation of carbon-based materials for energy storage. *Journal of Materials Chemistry*, **22**(45), 23710-23725.

Wang, X., Huang, S., Zhu, L., Tian, X., Li, S., Tang, H. 2014. Correlation between the adsorption ability and reduction degree of graphene oxide and tuning of adsorption of phenolic compounds. *Carbon*, **69**, 101-112.

Wang, Y., Alsmeyer, D.C., McCreery, R.L. 1990. Raman spectroscopy of carbon materials: structural basis of observed spectra. *Chemistry of Materials*, **2**(5), 557-563.

Wei, L., Sevilla, M., Fuertes, A.B., Mokaya, R., Yushin, G. 2011. Hydrothermal Carbonization of Abundant Renewable Natural Organic Chemicals for High-Performance Supercapacitor Electrodes. *Advanced Energy Materials*, **1**(3), 356-361.

Wen, J.-L., Sun, S.-L., Xue, B.-L., Sun, R.-C. 2013. Recent Advances in Characterization of Lignin Polymer by Solution-State Nuclear Magnetic Resonance (NMR) Methodology. *Materials*, **6**(1), 359.

Wise, L.E. 1946. Chlorite holocellulose, its fractionation and bearing on summative wood analysis and on studies on the hemicelluloses. *Paper Trade*, **122**, 35-43.

Xiang, J., Hu, S., Sun, L., Xu, M., Li, P., Sun, X. 2006. Evolution of carbon and

oxygen functional groups during coal combustion. *JOURNAL OF CHEMICAL INDUSTRY AND ENGINEERING-CHINA*-, **57**(9), 2180.

Xu, C., Arancon, R.A.D., Labidi, J., Luque, R. 2014. Lignin depolymerisation strategies: towards valuable chemicals and fuels. *Chemical Society Reviews*, **43**(22), 7485-7500.

Xue, Y., Gao, B., Yao, Y., Inyang, M., Zhang, M., Zimmerman, A.R., Ro, K.S. 2012. Hydrogen peroxide modification enhances the ability of biochar (hydrochar) produced from hydrothermal carbonization of peanut hull to remove aqueous heavy metals: batch and column tests. *Chemical Engineering Journal*, **200**, 673-680.

Yang, G., Chen, H., Qin, H., Feng, Y. 2014. Amination of activated carbon for enhancing phenol adsorption: effect of nitrogen-containing functional groups. *Applied Surface Science*, **293**, 299-305.

Zhang, L.-S., Li, W., Cui, Z.-M., Song, W.-G. 2009. Synthesis of porous and graphitic carbon for electrochemical detection. *The Journal of Physical Chemistry C*, **113**(48), 20594-20598.

Zhao, Y., Feng, D., Zhang, Y., Huang, Y., Sun, S. 2016. Effect of pyrolysis temperature on char structure and chemical speciation of alkali and alkaline earth metallic species in biochar. *Fuel Processing Technology*, **141**, 54-60.

Zhi, M., Xiang, C., Li, J., Li, M., Wu, N. 2013. Nanostructured carbon–metal oxide composite electrodes for supercapacitors: a review. *Nanoscale*, **5**(1), 72-88.

Zhu, X., Liu, Y., Zhou, C., Luo, G., Zhang, S., Chen, J. 2014. A novel porous carbon derived from hydrothermal carbon for efficient adsorption of tetracycline. *Carbon*, **77**, 627-636.

Zielke, U., Hüttinger, K., Hoffman, W. 1996. Surface-oxidized carbon fibers: I. Surface structure and chemistry. *Carbon*, **34**(8), 983-998.

초 록

바이오리파이너리 공정 부산물의 촉매 활성화 공정을 이용한 나노 세공 탄소 소재 개발 및 활용

황혜원
환경재료과학전공
산림과학부
서울대학교 대학원

본 연구에서는 고온 촉매 활성화 공정을 이용하여 바이오매스 연료화 공정 부산물로부터 나노 세공을 지닌 탄소 소재를 제조하였으며 공정 조건에 따른 산물의 표면과 화학 구조 특성을 비교분석하고 더 나아가 산업 분야로의 활용 가능성을 평가하고자 하였다.

첫 번째 장에서는 급속 열분해 탄을 이용하여 수산화칼륨 촉매의 농도를 달리하며 나노 세공 활성탄을 제조하였다. 제조된 활성탄의 친환경 흡착제로써 활용 가능성을 살펴보기 위해 용액 농도와 흡착 시간 조건에서 페놀 제거 실험을 수행하였다. 활성화 공정 이후 2711 m^2/g의 높은 비표면적과 1.58 cm^3/g의 총 기공부피를 지닌 활성탄이 제조되었고 이를 페놀 흡착 실험에 적용하였을 때 흡착 메커니즘이 Langmuir 등온식을 따르는 것으로 나타났다. 평형 흡착량은 625 mg/g으로 상용 활성탄의 흡착량(500 mg/g)보다 더 뛰어난 성능을 보였고 활성탄의 물성과 흡착량

사이의 상관관계를 분석하였을 때 mesopore 부피가 가장 큰 영향을 미치는 것으로 조사되었다.

두 번째 장에서는 급속 열분해 탄과 더불어 수열처리 탄을 이용하여 고온 촉매 활성화 공정을 실시하였고 이 때 반응 가스의 영향을 살펴보기 위하여 공정의 대기 조건을 비활성 기체인 질소뿐만 아니라 활성 기체인 제로에어 가스 상태로 조절하여 반응을 진행하였다. 또한, 질소 조건에서 생성된 활성탄을 대상으로 기존의 후 산화 처리 기법으로 표면을 개질한 후 제조된 각 탄소 소재의 특성을 비교하였다. 이 때 반응 중 방출되는 휘발성 유기화합물의 분포를 분석하였고 반응 전후의 각 전구체와 활성탄에 대한 방향족 탄소 구조의 변화를 관찰함으로써 촉매에 의한 탄의 열분해 거동을 조사하였다. 또한 바이오매스 연료화 공정 부산물의 비표면적은 약 23 m^2/g 이하로 매우 낮았지만 활성화 공정 이후 최대 1879 m^2/g로 크게 증가하였다. 더 나아가, 활성탄을 납 흡착 및 탄소 전극 용도로 활용하였을 때 각 성능은 비표면적, 관능기, 친수성 및 mesopore 분포에 영향을 받았다. 기존의 후 산화 처리 기법으로 개질된 활성탄과 비교하였을 때 제로에어 조건 활성탄은 높은 납 흡착률 (41.1 mg/g)과 비정전용량 (185.9 F/g)을 보이며 다방면에 높은 활용 가능성을 나타내었다.

마지막 장에서는 리그닌을 사용하여 반응 온도 (700-800℃), 시간 (0.5-2h), 촉매 투입 비율 (1:1-6:1; w:w=촉매:리그닌)과 같은 다양한 공정 요인에 따른 활성탄의 물성 변화를 살펴보았다. 촉매 반응은 상대적으로 낮은 온도, 짧은 반응 시간, 적은 촉매 비율일 경우 물질 표면에서부터 반응이 시작되며 각 요인의 수치가 증가할수록 점차 내부 구조로 이동하여 de-alkylated aromatics의

방출과 더불어 구조 변형 혹은 붕괴가 일어나게 됨을 확인하였다. 리그닌 유래 활성탄의 비표면적은 최대 2782 m^2/g 으로 일정 수준의 공정 조건 이상 (750℃, 촉매 비율 4)에서 제조된 활성탄은 서로 비슷한 비표면적 특성을 지니는 것으로 나타났다. 이후 활성탄의 중금속 2종 (납, 카드뮴)과 유기물질 3종 (phenol, bisphenol-A, 2,4-dichlorophenoxyacetic acid)에 대한 흡착 효율을 비교하였을 때 흡착제인 활성탄 구조와 흡착질 간 $\pi-\pi$ 결합의 증가로 인하여 유기물질에 대한 제거 효율이 중금속에 비해 더 뛰어났다. 또한, 리그닌 유래 활성탄을 이용하여 슈퍼커패시터용 탄소 전극을 제조하였고 전기적 특성을 분석한 결과 추후 상용 활성탄을 대체할 수 있는 잠재성을 보였다.

본 연구에서는 바이오리파이너리 공정에서 부산물로 발생하는 탄과 리그닌의 고부가가치 활용을 위해 다양한 공정 조건에서 촉매 활성화 공정을 수행하였고 표면 특성이 개질된 나노 세공 활성탄을 생산하였다. 제조된 활성탄의 화학·구조적 특성을 다양한 분석기법을 이용하여 분석하였으며 더 나아가 오염 수질에 존재하는 중금속과 유기물질을 제거하기 위한 친환경 흡착제 및 슈퍼커패시터용 탄소 전극으로써 성능을 조사하였다. 이를 바탕으로 고형 부산물의 열변환 특성을 이해할 수 있었고 제조 산물을 실제 산업 분야에 활용함으로써 잠재적 사용 가치를 확인하였다.

키워드 : 급속 열분해, 수열 액화 공정, 리그닌, 활성탄, 방향족 탄화수소, 표면 개질, 친환경 흡착제, 탄소 전극